2015

A Synthetic Exploration of F-Element Borates and Plumbites

Jared Tyler Stritzinger

FLORIDA STATE UNIVERSITY

COLLEGE OF ARTS AND SCIENCES

A SYNTHETIC EXPLORATION OF *f*-ELEMENT BORATES AND PLUMBITES

By

JARED STRITZINGER

A Dissertation submitted to the
Department of Chemistry and Biochemistry
in partial fulfillment of the
requirements for the degree of
Doctor of Philosophy

Degree Awarded:
Spring Semester, 2015

Jared Stritzinger defended this dissertation on April 9, 2015.
The members of the supervisory committee were:

Thomas Albrecht-Schmitt
Professor Directing Dissertation

Ingo Wiedenhöver
University Representative

Susan Latturner
Committee Member

Albert Stiegman
Committee Member

The Graduate School has verified and approved the above-named committee members, and certifies that the dissertation has been approved in accordance with university requirements.

This is work is dedicated to my parents, Frank and Pamela Stritzinger, and to my fiancée, Laurel Winter. This work would not have been possible without each of you and your tireless support and endless patience.

ACKNOWLEDGMENTS

I would like to thank my parents and sister for their never-ending love, encouragement, and support. They have instilled in me the drive to work hard at the tasks I undertake and strive to complete them to the best of my abilities. Without their mentorship, guidance, and belief in me, I would not be writing this dissertation.

I would like to thank my fiancée, Laurel Winter. I cannot begin to convey how much you have done for me. From your endless patience with my antics to the love and compassion you have always shown me, you motivate me to strive to be and do better everyday.

I would also like to thank my advisor, Dr. Thomas Albrecht-Schmitt. It has been a wild ride across half the country and through strange times. You were my first introduction to the world of actinide chemistry and have shaped the way I think about science, research, careers, and my life. Throughout everything you have always been there to listen and believed in me even when I didn't. I am honored to have worked under your guidance and earned your respect.

To my older lab mates, thank you for everything you have taught me. Dr. Shuao Wang and Dr. Juan (Jenny) Diwu thank for teaching that wide-eye undergraduate summer researcher that when there's a problem we solves it. Dr. Eric Villa, you have always given me your help, guidance, and thoughtful insight, and without knowing it served as a role model. Dr. Matt Polinski, Dr. Justin Cross, and Dr. Jian Lin, thank you for being there to bounce ideas off of, put me back on track, and always lift me up.

To my current lab mates, I'm proud to have introduced you to the lab and learned from each of you in the process. Gannon Parker, Samantha Cary, Mark Silver, and Ali Arico, y'all are great. I would like to thank the undergraduates that carried out some of this work: ER Noche, Alexandra Barth, Reynold Bartel, and Mackenzie Beatrice; thank you for allowing me to take part in your science education. Kristen Pace, you so often taught me by asking questions, causing me to reexamine my understanding of what I was explaining.

I would like to thank a number of other professors who have influenced and taught me so much, Dr. Colin McMillen, Dr. Joseph Kolis, Dr. Allen Oliver, and Dr. Evgeny Alekseev.

To my committee members Dr. Susan Latturner, Dr. Albert Steigman, Dr. James Brooks, and Dr. Ingo Wiedenhöver, thank you for donating your time and attention to my education. I

would also like to thank Florida State University and the Department of Chemistry and Biochemistry.

Finally, I would like to thank the Chemical Sciences, Geosciences, and Biosciences Division, Office of Basic Energy Sciences, Office of Science, Heavy Elements Chemistry Program, U.S. Department of Energy, under Grant DE-FG02-09ER16026 for funding my research.

TABLE OF CONTENTS

LIST OF TABLES

LIST OF FIGURES

ABSTRACT

Despite their discovery during the 1940's, there are still many unanswered questions surrounding the elements past uranium, or transuranic elements. In the recent years more evidence is emerging that suggest the bonding and structure of the actinides in more complex than previous thought. We look to expand on this by careful choice of ligands as a means of probing the bonding observed in actinide complexes.

Towards the exploration of the nature of bonding in the actinide, the development of trends for ligand interaction is a goal. Currently, there is very little to indicate which ligands will show more covalent interactions or which will show more ionic interactions. Examining ligand systems that demonstrate a variety of characteristics, various oxoanions have been chosen over the traditional carbon based ligands. It is reasonable to view *f*-element interactions with oxoanions as metal ligand interactions and an excellent system to study displaying a variety of characteristics.

Currently the overall softness and polarizability of ligands is the only characteristic that lends some insight to the potential for covalency. However the choice of oxoanions makes the application of polarizability a guide difficult. Through use of the quantified hyperpolarizability of oxoanions a guide to discriminate between anions with lower polarizability such as phosphite and those with higher polarizability such as molybdate. With the higher degree of polarizability indicated by the hyperpolarizability, more covalent bonds with actinide metals are expected leading to unusual properties and differences when compared with lanthanide.

Though traditional mild hydrothermal methods have proved suitable for the synthesis of crystalline products, there are limits to the method. To expand the synthetic versatility of the lab and access new hydrothermal phase space autoclaves for synthesis in supercritical media were developed. In particular supercritical water is a desirable synthetic media for crystal growth owing to characteristics as a solvent and the ability to access oxidations of metals otherwise inaccessible to mild hydrothermal methods.

This dissertation is focused on the development of synthetics methods for the isolation and characterization of new *f*-element materials. To this end, each chapter reports on the synthetic methods and the novel *f*-element materials that incorporate highly polarizable oxoanions.

CHAPTER ONE

INTRODUCTION

1.1 Overview

With the dawn of quantum theory and elucidation of the structure of the atom came numerous breakthroughs in science, but the one that would have the most resounding effect was nuclear fission. The astounding power released when an atom is split could power a city for years or obliterate it in seconds. Beyond the release of energy, these discoveries also lead to the production of new elements past uranium, that have fascinating chemistry. Even to this day, over 70 years later, these elements continue to reveal interesting chemistry and are slowly beginning to give up their secrets.

Understanding these transuranic element better is becoming increasingly import as the world turns its collective eye to fossil fuels alternatives. One of the major players in alternative energy is nuclear energy. In the United States alone, approximately 20% of domestic energy is produced from nuclear power plants.[1] While the carbon emissions of these plants are low, they require large amounts of water to cool and produce a copious amount of radioactive waste. In 2011, it was reported that United States spent nuclear fuel inventory consisted of 65,000 metric tons and growing at a rate of 2,000 and 2,500 tons per year.[1,2] For 2015, that places the current number at 75,000 tons, and it is expected to grow with the approval of new nuclear plants in South Carolina and Georgia.

As the spent nuclear fuel contains various fission and neutron capture products, the fuel must be sequestered for 300,000 years before it can be safely removed.[3] In the United States, the now defunct Yucca mountain was designated to be a geological repository for domestic spent fuel and the Waste Isolation Pilot Plant (WIPP) in Carlsbad, New Mexico, a deep salt mine, was designated for defense waste.[4–6] However, the need for time spent in a repository can be significantly reduced by the removal of the actinides as they compose the majority of the long-lived waste. In addition to reducing the storage time of waste, the isolation of some actinide isotopes could be fissioned to produce more energy and transmute the elements into easier to manage waste.

For the majority of history the separation of nuclear waste has focused on extracting the plutonium and uranium from the spent nuclear fuel. The process developed during the Manhattan Project known as Plutonium Uranium Extraction (PUREX) focused on separating plutonium and uranium by manipulating the redox chemistry of these elements.[7,8] While this process was mastered over seventy years ago, today's need to separate the other actinides for storage and recycling is growing, but faces challenges. A modified PUREX process can be used to separate Neptunium, however the minor actinides, Americium and Curium, present difficulties.[9] Due to their common oxidation state, ionic radius, and coordination environment, developing elementally selective extractions for actinides from other lanthanide fission products is difficult.[10,11] Separating the Americium, allows for it to be re-burned or transmuted providing more power while reducing waste. By drawing the curium off, the total time needed to store lanthanide fission products is greatly reduced. Beyond the minor actinides, berkelium and californium possesses a particularly high radioactivity and poorly understood chemistry. Their high radioactivity presents numerous logistical complications that must be overcome to properly study their chemistry, resulting in their under representation in the literature.

Despite the inherent challenges present in extracting and separating transplutonium elements, recent developments have shown that soft ligands, specifically N-donors show slightly higher binding affinity for the minor actinides over the lanthanides.[12] This is linked to the stronger bonds that form from the apparently covalent interactions. The underlying reasons for the higher affinity and selectivity is poorly understood and the development of ligands for extraction has been slow. However, a study suggests that the affinity for the actinides is directly correlated to the overall hardness of the ligand.[13] This may be linked to the overall polarizability of the soft donors. Exploring the link between polarizability and affinity in the actinides is imperative to gain a better understanding of the interactions between actinides.

1.2 Oxidation States of *f*-Elements

When examining the similarities and differences between the lanthanides and actinides, it is convenient to start at the available oxidations states, **Table 1.1**.[14] In the lanthanides the trivalent state dominates as it is thermodynamically stable.[15,16] Though it has been demonstrated that all lanthanides can access the divalent state, only europium and ytterbium can do so easily.[17] Cerium must also be mentioned as it can easily access the tetravalent state. The actinides redox

chemistry is significantly more complex, with a variety of oxidation states accessible and differing thermodynamic stabilities. This diversity in accessible oxidation states, especially in uranium, neptunium, and plutonium, is akin to that of transition metals.[15,18] Plutonium, however, deserves special attention as it's electrochemistry is particularly complex; in solution plutonium can exist as Pu(III), Pu(VI), Pu(V), or Pu(VI), however a mixture of these oxidation states in more common as the standard reduction potential separating each oxidation state is approximately 1.0 V.[14,19] The transplutonium elements see a reemergence of the trivalent state as the most stable oxidation state. However at californium the divalent state becomes accessible, and becomes the dominant oxidation state at nobelium.[14]

Table 1.1 *f*-Element oxidation states

La	Ce	Pr	Nd	Pm	Sm	Eu	Gd	Tb	Dy	Ho	Er	Tm	Yb	Lu
		(2+)	(2+)	(2+)	2+	2+	(2+)	(2+)	(2+)	(2+)	(2+)	2+	2+	(2+)
3+	**3+**	**3+**	**3+**	**3+**	**3+**	**3+**	**3+**	**3+**	**3+**	**3+**	**3+**	**3+**	**3+**	**3+**
	4+	4+	4+					4+	4+					

Ac	Th	Pa	U	Np	Pu	Am	Cm	Bk	Cf	Es	Fm	Md	No	Lr
	(2+)		(2+)			(2+)			(2+)	2+	2+	2+	**2+**	**2+**
+3	(3+)	(3+)	3+	3+	3+	**3+**	**3+**	**3+**	**3+**	**3+**	**3+**	**3+**	3+	3+
	4+	4+	**4+**	4+	**4+**	4+	4+	4+	4+	4?				
		5+	5+	**5+**	5+	5+	5?		5?					
			6+	6+	6+	6+	6?							
				7+	7+	7?								
					8?									

1.3 Bonding in *f*-Elements

The traditional view of bonding in *f*-elements is that almost all interactions are ionic as the *f*-orbitals are core-like and tend to have little involvement in bonding. However this general view does not reflect the complexity and uniqueness of the *f*-elements. Beyond misrepresenting the richness of bonding in the actinides, this has also lead to the use of lanthanides as surrogates for the actinides, resulting in a misrepresentation of actinide bonding.

In the lanthanides the 4*f* orbital is buried beneath the *6s*, 6*p,* and 5*d*, orbitals.[16] Additionally, when examining the radial extent of lanthanide ions, they tend not to extend beyond 1.4 Å.[20] These characteristics result in the lanthanides exhibiting non-interacting and non-bonding 4*f* orbitals, with only a few cases of 4*f* orbital interactions with ligands.[16] Evidence of this limited interaction is shown in lanthanide ultraviolet-visible-near infrared absorbance spectroscopy, where Laport forbidden *f-f* transitions are observed as sharp peaks as ligands do not interaction with the 4*f* orbitals and are unable to alter the energy of the transitions.

The trend of core *f*-orbitals does not hold for the actinides, were the 5*f* and 6*d* orbitals are close in energy and the primary orbitals involved in bonding. Additionally the semi-core like 6*s* and *6p* orbitals may become involved in bonding, depending on their energies and the lingand.[21,22] With the variety of orbitals involved, understanding how bonding and orbital interactions lead to more covalent behavior is difficult to elucidate.[14,23] This is primarily observed in the early actinides for thorium to plutonium as the transition metal behavior, best represented by the rich electrochemistry, reflects the involvement of the 6*d* orbital. However this transition metal like behavior has been thought to tapper off, starting at americium, for the heavier actinides as they develop lanthanide like characteristics, with the emergence of the trivalent state. However, the simple emergence of lanthanide-like stability in oxidation state is not always reflected by an emergence of lanthanide-like bonding.

The 5*f* orbital drops in energy at the actinide series is traversed.[24] At the beginning of the series the near degeneracy of the 5*f* and 6*d* orbitals are evident, allowing electrons to occupy either orbital.[15,18] However, at plutonium the 5*f* orbital has dropped far enough below the 6*d* orbital, that the ground state electrons only occupy the 5*f* orbital. With the loss of the 6*d* involvement, the transition metal-like behavior is thought to be lost, as the 5*f* orbital is more core-like, mirroring the 4*f* orbital. However, the decrease in energy of the 5*f* orbital places it at the same energy as the 2*p* orbitals of most ligands, especially those composed of oxygen, carbon,

and nitrogen.[24] This provides the 5*f* orbital with strong ligand orbital energy matching, allowing it to play a more direct role in bonding, which is evidenced in the growing body of work that shows soft-donor ligands prefer actinides over the lanthanide counter parts. [20,25,26,27–29]

1.4 Comparative Studies of *f*-Element Systems

A number of comparative studies have been completed for both the lanthanides and actinides producing interesting results. Examining the aquo-triflate complexes, $M(H_2O)_9(CF_3SO_3)_3$ ($M = Ln^{3+}$ or An^{3+}), the actinides and lanthanides are nearly identical in behavior.[30] Both spectroscopic and magnetic results show highly ionic interactions and theoretical calculations suggest no *f*-orbital involvement. However in the case of the tris-cyclopentadienyl compounds $M(C_5H_5)_3$ (M=Th-Cf), complex bonding is observed.[14,31] This is exhibited primarily in the absorption spectra the electronic states have been altered by ligand interactions. These complexes show more covalent bonding indicated by the broadened absorption peaks or significantly red shifted transitions.[32–38] This oddity has spurred a number of theoretical studies of the system to better understand orbital involvement. The results have shown the primary interactions are between the metal's 6*d* orbitals and the carbon's 2*p* orbitals, with additional, but minor 5*f* to 2*p* orbital interactions. As mentioned in Section 1.3, as the actinide series is traversed the 5*f* orbital decreases in energy, better matching the carbon 2*p* orbital is observed, while the 6*d* increases in energy, subsequently reducing its energy match and contributions. Additionally, the greater radial extension of the 5*f* orbital allows for greater over lap with the cyclopentadienyl ligands. However, in this case of increased orbital overlap and energy matching there is no apparent sharing of electrons, making the nature of the interaction difficult to classify.

1.5 Anion Hyperpolarizability and Polarizability

When comparing the cases of $M(C_5H_5)_3$ and $M(H_2O)_9(CF_3SO_3)_3$, it is clear that some characteristics of the ligands govern orbital accessibility, which plays a major role in the electronic effects. There is further evidence of this in the neutral N-donor *f*-element complexes that show both thermodynamic trends and absorption spectra that suggest covalent interactions.[39,40] This suggests that soft, polarizable ligands possess the capacity to exhibit bonding differences between the lanthanides and actinides.

Applying this concept to oxoanions, which are typically considered hard, suggests that bonding exhibiting covalent interaction should be inaccessible. However this direct application of hard-soft theory, does not prove valid, as the *f*-element borates show unique orbital interactions for the actinide series.[41–45] The borate oxoanion is interesting as it can adopt two coordination geometries, tetrahedral BO_4 and trigonal BO_3, and polymerize, resulting in the ability to form complex, polarizable networks.[46,47] The polarizability of borate and most oxoanions is extremely difficult to quantify, especially in cases of a complex network. Looking beyond the polarizability of oxoanions, there is the quantified hyperpolarizability, **Table 1.2**, which is the susceptibility of the metal oxygen bond to distort when impinged upon by an optical field.[48,49] This value may yield insight to the polarizability of the anion as a whole unit, as a high hyperpolarizability indicates large movements of electron density across the anion.

Table 1.2 Reported hyperpolarizabilities of various M-O bonds

M−O Bond	$B \cdot 10^{-40}(m^4/V)$	Compound
Ti^{4+}−O	495	$BaTiO_3$
W^{6+}−O	230	$BaTeW_2O_9$
Te^{4+}−O	130	Te_2SeO_7
Se^{4+}−O	160	$TeSeO_4$
Pb^{2+}−O	865	$PbTiO_3$
N^{3+}−O	12	$NaNO_2$
P^{5+}−O	17	KH_2PO_4
Cl^{5+}−O	11	$NaClO_3$
Br^{5+}−O	23	$NaBrO_3$
I^{5+}−O	140	$LiIO_3$, HIO_3
Nb^{5+}−O	240	$LiNbO_3$
Ta^{5+}−O	200	$LiTaO_3$
Mo^{6+}−O	305	$RbMoO_3(IO_3)$

Using hyperpolarizability has proved an effective guide for predicting covalent interactions with oxoanions. In the instance of P^{5+}-O, the low hyperpolarizability of 17 $\beta \cdot 10^{-40}(m^4/V)$ suggests that ionic bonding should be exhibited in the both the actinides and lanthanides. In fact this holds true as shown for both plutonium and americium phosphites when

compared to the lanthanide phosphites as the exhibit the same structure and expected spectroscopy.[50] In the instances of W^{6+}-O and Mo^{6+}-O the high hyperpolarizabilities, 230 and 305 $\beta \cdot 10^{-40}(m^4/V)$ respectively, indicate a greater possibility for covalent interactions to arise. This too was shown to be true in a series of actinide molybdates and tungstates.[51–53] In both the series, changes in structures arise when comparing lanthanide and actinides materials prepared in the same manner. Additionally the emergence of larger charge transfer bands in the actinide materials shows increased orbital interactions. To further examine this concept, lead *f*-element systems are ideal, as Pb^{2+}-O has the highest reported hyperpolarizability of 865 $\beta \cdot 10^{-40}(m^4/V)$ suggesting the potential for even more orbital involvement.[48]

CHAPTER TWO

SYNTHETIC METHODS AND CHARACTERIZATION TECHNIQUES

2.1 Synthetic Methods

Boric acid (H_3BO_3) is a weak acid, where the mechanism for its acidity is through the acceptance of a hydroxide group, rather than proton donation.[54,55] While a solid at room temperature it can easily be dissolved in water, and the dissociation equation, $B(OH)_3$ (*aq)* + H_2O (*l*) ⇔ $B(OH)_4^-$ (*aq*) + H^+ (*aq*), shows how boric generates a proton by accepting a hydroxide from the water.[56] When boric acid heated to 170.9 °C, boric acid melts and begins to undergo a series of dehydrations. As temperature increases metaboric acid, HBO_2 begins to form and with further heating above 230 °C, tetraboric acid, $H_2B_4O_7$, becomes the predominate form. If heated beyond 300 °C, boric acid is completely dehydrated and boron oxide B_2O_3 is formed.

This flexibility in phase, through a wide temperature regime, coupled with its high solubility, makes boric acid an ideal flux agent as it can simply be washed away after the reaction is complete. Its use as such, was first pioneered by Williams *et. al,* as a route to synthesizing $[H_2en]_4[Hen]_2[V_6B_{22}O_{53}H_8]\cdot 5H_2O$ (en = ethylenadiamine $C_2H_4(NH_2)_2$).[57] Since then the application of boric acid as a flux has been expanded to aluminoborates,[58–60] borophosphates,[61,62] and transition metal borates.[63–65]

The first application of the boric acid flux method to *f*-elements showed the formation of $Ln[B_5O_9(OH)_3]$ (Ln = Gd – Lu).[66,67] It was then shown that by controlling the ratio of metal to boric acid in reactions exhibit some control over the reaction as different structures were isolated with different rations.[68] The boric acid flux method was applied to the high oxidation state, light actinides with the synthesis of a number of thorium, uranium, and neptunium borates by Shuao Wang.[69–73] The trivalent transuranic elements were explored and compared to their trivalent lanthanide counterparts by Matt Polinski.[42–44]

Boric acid flux reactions were conducted by charging a 23 mL internal volume polytetrafluoroethylene (PTFE) liner with the reagents and loading the liner into a Parr 4749 stainless steel acid digestion vessel. (For transuranic reactions, PTFE liners with an internal volume of 10 mL were used and the reagents were scaled down to accommodate the 5 mg of the

starting actinide salt.) An excess of boric acid is used as it acts both as a solvent and ligand for the starting lanthanide or actinide source. A small amount of water or acid, about 0.2 mL, is added to aid in crystallization and introduce additional anions. The vessel is sealed and placed in a box furnace at 200 °C to 240 °C for 5-7 days. The reaction is cooled at a rate of 5 °C/hr until room temperature is reached. Products can be isolated from the aggregate at the bottom of the liner by dissolving the excess boric acid in boiling water.

The boric acid flux differs from the traditional hydrothermal methods as it employs negligible amounts of water when compared to the reactants. Depending on the conditions and size of the reaction vessel, anywhere between 1 mL to 20 mL of water can be used, a comparably large amount with respect to the other reactants. The excess of solvent defines the hydrothermal technique and has been employed to grow many solid-state materials.[74,75] Hydrothermal reactions also distinguish themselves from the boric acid flux method, with notably shorter reactions time, as short as two hours, making it more ideal for the "trapping" kinetic products.

One difficulty encountered when working in the hydrothermal regime is that the solubility of starting reagents and the products plays a major role in the reaction. If sufficient quantities of the reagents are not solubilized, they cannot react to form the desired products. This is often overcome through the use of acids, mineralizers, or elevated temperature. However when adding acids and mineralizers, the potential formation of high insoluble binary salts must be considered. This is particularly important with respect to the Pb(II) ion, which forms insoluble salts with all halides, sulfates, and hydroxides.

Typical hydrothermal reactions are conducted by charging a 23 mL internal volume polytetrafluoroethylene (PTFE) liner with the reagents and loading the liner into a Parr 4749 stainless steel acid digestion vessel. (For transuranic reactions, PTFE liners with an internal volume of 10 mL were used and the reagents were scaled down to accommodate the 5 mg of the starting actinide salt.) A large amount of water is added to the liner, 1 mL - 2.5 mL, to act as a solvent. Often acids or solutions of mineralizes are added in place of water to aid solubility or crystallization. In the case of Pb(II), weakly coordinating acids such as $HClO_4$ were utilized. The vessel is then sealed and placed in a box furnace at 150 °C to 230 °C for 1-5 days. The reaction is then cooled at a rate of 5 to 10 °C/hr until room temperature is reached. Rapid cooling, known as quenching, can be utilized when attempting to isolate kinetic phases. Products can be isolated from the liner by the removal of water.

When temperature regimes exceed 250 °C, the PTFE liners begin to flow and common acid digestion vessels are no longer sufficient to carry out hydrothermal reactions. Transitions to all metal autoclaves that utilize a metal-metal sealing mechanism must be made to contain the pressure generated from heating water. Additionally, at 374.2 °C and 22.4 MPa water transitions into the supercritical state, taking on the characteristic of both a liquid and a gas. Unfortunately in these temperature and pressure environments, corrosion of the autoclave becomes an issue as reactions begin to involve the iron, nickel, or other various metals of the autoclave walls.

The supercritical water regime is an attractive phase space to explore for crystal growth owing to its dissolving and diffusion properties, which are critical for crystal growth.[76] The growth from a supercritical solution offers access to starting materials and products that do not melt through conventional techniques. This allows for reagents that melt above 1000 °C to be used at much lower temperatures, around 600 °C and overcomes issues encounter with materials that melt incongruently. In addition to allowing access to different reagents, supercritical water's significantly reduced viscosity results in lower rate of solvent trapping in crystals as they grow.

As a result autoclaves were designed and manufactured with the help of the machine shop. Each autoclave was made out of RENE 41, a steel alloy with a high nickel content, which offers superb strength and thermal properties for the containment of high pressures and temperatures. The autoclave is a 2.0" diameter cylinder with a 0.5" bore diameter and measures 9" in height, with an internal volume of 27 mL. The sealing mechanism employed is a "cold Tuttle seal," where a coned plunger is driven into the circular opening of the autoclave by a capping nut. A pressure gauge and pressure release system consisting of a manual release and over pressure burst plate are connected to the plunger via a step down connector.

The fully assembled autoclave system can be heated by being placed in a vertical tube furnace. When setting the autoclave in the furnace, the cap-nut should be left outside the furnace, to ensure a proper seal. Alternatively, to establish more thermal control over the autoclave, band heaters can be attached directly to the autoclave system. The heaters are regulated by an Omega controller that monitors the temperature via a type K thermocouple placed between the band heater and outer surface of the autoclave. The band heater system is placed in a cinderblock pit filled with vermiculate insulation. Additional pictures and information is in Appendix C.

To overcome corrosive concerns floating liners were used inside of the autoclave. Silver metal has been shown to be inert towards basic mineralizers and only reactive in the presence of

oxidants or acidic mineralizers. This is an ideal reaction vessel offering relative inertness while being more cost effective than other inert metals such as gold or platinum. Typical silver floating liners were made from 0.25" outer diameter fine silver tubing cut into 2.5" lengths. One end of the tubing was crimped and welded shut. The liner is typically charged with 100-300 mg of total reagents and 0.4 mL of basic mineralizer. The open end of the liner is cleaned with a Kimwipe to remove any mineralizer and starting reagent to ensure a proper weld. The open end is crimped and welded shut. Under a microscope, each floating liner should be inspected for leaks at the weld sites. When reaction conditions required oxidants or acidic conditions, 0.5" diameter quartz tubes were used. In that case 12" lengths of quartz tubing was heated at the mid point and pulled into two 6" lengths to form floating liners. Each vessel was typical charged with 300 mg to 500 mg of reagents and 0.5 mL to 0.8 mL of an oxidizing or acid mineralizer. The quartz tube is then submerged in liquid nitrogen to freeze the mineralizers. This allows for the vessel to be connected to an schlink line via a Swagelok and evacuated under vacuum. The vessel is then sealed about an 1.5" from the Swagelok in the flame, which results in a vessel is about 4" long.

Sealed floating liners are loaded into the bore of the autoclave. Six silver liners can be loaded if two band heaters are being used; only four should be loaded when using one band heater. The use of small pliers may be used to slightly depress the middle of the silver liner, allowing them to be loaded easier. When loading quartz liners, only one liner can be run in the autoclave at a time. If two quartz liners are placed in the autoclave, the nesting of the sealed ends of the quartz linear is problematic as thermal expansion causes the liners to break. The void space in the autoclave is completely filled with deionized water as a counter pressure measure. After reactions are completed, and liners are removed, the silver liners are crushed and must be cut open with pliers and flushed to remove products. Quartz liners are scored, cracked open, and flushed to isolate products.

2.2 Characterization Techniques

Upon synthesis and isolation of crystals from either flux or hydrothermal reactions, a number of characterization techniques are employed to determine the structure, magnetic, and electronic properties of the product. In the case of radioactive materials, especially transuranic elements, additional procedures must be taken so free-flowing solids are not handled outside a negative pressure glove box, as they present a serious safety and contamination concerns.

2.2.1 Single Crystal X-ray Diffraction

The main characterization technique used to elucidate the structure of crystalline products is single crystal X-ray diffraction (SCXRD). The data gathered can be check against databases to determine if the structure has been previously identified. Well-formed, transparent crystals with defined edges were selected and mounted on cryoloops with immersion oil. Crystals were optically aligned on a Bruker D8 Quest X-ray diffractometer using a digital camera. Initial intensity measurements were performed using a IμS X-ray source (MoKα, λ = 0.71073 Å) with high-brilliance and high-performance focusing multilayered optics. Standard APEXII software was used for determination of the unit cells and data collection control. The intensities of reflections of a sphere were collected by a combination of four sets of exposures (frames). Each set had a different ϕ angle for the crystal, and each exposure covered a range of 0.5° in ω. A total of 1464 frames were collected with an exposure time per frame of 20-60 s, depending on the crystal. SAINT software was used for data integration including Lorentz and polarization corrections. Absorption corrections were applied using the program SCALE (SADABS). The structure was solved by direct methods and refined on F2 by full-matrix least squares techniques using the program suite SHELX.

2.2.2 Powder X-Ray Diffraction

Powder X-Ray Diffraction (PXRD) was used to determine the phase purity and overall crystallinity of samples. Approximately 10 – 30 mg of a sample was ground using a mortar and pestle and placed on a sample holder. When loading the sample holder care was taken to avoid preferred orientation while maintaining a flat surface. PXRD performed on a Rigaku DMAX 300 Ultima III powder X-ray diffractometer using Cu Kα radiation (λ = 1.54185 Å) and on an original X-ray diffraction setup using Guinier camera 670 with a Huber imaging plate and a Ge crystal monochromatic (Cu Kα, λ = 1.54060 Å).

2.2.3 UV-Vis-NIR Absorption and Photoluminescence Spectroscopy

UV-Vis-NIR absorption spectroscopy data of *f*-elements is unique to both the element and oxidation state as the main peaks observed are *f-f* transitions that arise from spin orbit coupling. As *f*-electrons are typically not involved in bonding the transitions do not shift in energy. These characteristics allows for determination and identification of *f*-elements and their oxidation state in compounds from absorption data. Photoluminescence spectroscopy can further

serve confirm the identity of the *f*-element present in the crystals, by providing another characteristic that differs by element, **Table 2.1.**[77,78] Additionally, significantly shifted or broadened *f-f* transitions in the absorption or photoluminescence spectra may indicate that the *f*-orbitals are being influenced and shifted, a potential indicator of covalency. When broadening occurs, vibronic progressions may become evident, suggesting coupling of the vibronic and electronic modes.

Table 2.1 *f*-Element fluorescence reference

Lanthanide	Color	Peak (nm)
Pr(III)	Orange	525-680
Nd(III)	NIR	1060
Sm(III)	Orange	590
Eu(III)	Red	620
Eu(II)	Blue	430
Gd(III)	UV	312
Tb(III)	Green	550
Dy(III)	Yellow-Orange	570
Ho(III)	Green	540
Er(III)	NIR	1530
Yb(III)	NIR	980

Actinide	Color	Peak (nm)
U(VI)	Green	500, 525
Am(III)	Red	685
Cm(III)	Orange-Red	600
Cf(III)	Green	525*

* centered at

UV-vis-NIR and photoluminescence data were acquired from single crystals using a Craic Technologies microspectrophotometer. Crystals were placed on quartz slides under Krytox oil and the data was collected from 200 to 1700 nm. The exposure time was auto-optimized by the Craic software. Photoluminescence data was acquired using the same microspectrophotometer with an excitation wavelengths of 260, 365, 420, and 563 nm and equipped with a Linksys cold stage operating from 25 °C to -193.4 °C.

2.2.4 Scanning Electron Microscopy and Energy-Dispersive X-Ray Spectrometry

Scanning electron microscopy was preformed on single crystals mounted on carbon discs with double-sided carbon tape. Crystals with flat, clean faces were selected and three to four different data points were collected to provide the least standard deviation. Images and data were collected using a JEOL 5900 with an XRF energy-dispersive X-ray spectrometer. The energy of

the electron beam was set at 29.02 kV and the spectrum acquisition time was 60 s. Analysis was used to verify elemental composition and aid in resolution of dissorder.

2.2.5 Magnetic Measurements

Magnetic measurements were taken using a Quantum Design Magnetic Properties Measurement System. Samples were prepared by grinding 20 to 30 mg of a pure crystalline product with a mortar and pestle and loaded into polycarbonate capsules placed in a straw. For transuranic samples, 2.0 to 3.0 mg of unground sample was loaded into a Quantum Design sample rod assembly, sealed RSO 4090-405 that utilized threading for containment. Zero-field cooling and field cooling sequences were performed at 1,000 Oe at temperatures ranging from 1.8 K to 300 K. Each sequence followed the intervals outlined in **Table 2.2**. Polycarbonate sample holder corrections were applied to the raw magnetic data. Hysteresis was performed at 5 K and 205 K at magnetic fields ranging from -5.5 T to 5.5 T.

CHAPTER THREE

FURTHER EVIDENCE FOR THE STABLIZATION OF U(V) WITHIN A TETRAOXO CORE

Adapted with permission from Stritzinger, J. T.; Alekseev, E. V.; Polinski, M. J.; Cross, J. N.; Eaton, T. M.; Albrecht-Schmitt, T. E. *Inorg. Chem.* **2014**, *53* (10), 5294–5299.

3.1 Introduction

Variable oxidation states are a prevalent feature of the early actinides and uranium is an excellent example of this, existing in all oxidation states between 2+ and 6+.[14,17] However, in the presence of air and water only the 4+ and 6+ oxidation states are common.[14] The preparation of U(V) compounds is often problematic in aqueous media because U(V) rapidly disproportionates into U(VI) and U(IV).[79,80] Despite this, U(V) compounds are becoming better represented in the literature owing to new and nontraditional synthetic methodologies that are able to circumvent disproportionation pathways.[81,82] Among the most promising of the new techniques employed for preparing uncommon valence states for uranium is the use of supercritical water as a reaction medium. Lii *et al.* have championed this method and provided numerous examples of mixed-valent uranium silicates and germanates, one of which simultaneously contains U(IV), U(V), and U(VI).[83]

Uranium's variable coordination chemistry leads to great structural diversity in this family of compounds. In low oxidation states, high coordination numbers of eight and nine are common, and the coordination is relatively isotropic. When the oxidation state is raised to 5+ or 6+, trans-terminal oxo groups are typically present, and this leads to highly anisotropic coordination environments that take the form of bipyramids with four to six donor atoms in the equatorial plane perpendicular to an AnO_2^{n+} core. While the most common U(VI) structural unit is the UO_7 pentagonal bipyramid, there are compounds that contain uranium in as many as three different coordination environments simultaneously.[84,85]

Our group has been interested in the preparation of novel actinide borates from thorium to californium in oxidation states from 3+ to 6+.[41,42,86] Neptunium borates show remarkably rich redox chemistry and mixed-valency is common.[87] However, all uranium borates to date only

contain U(VI). The use of supercritical water as a reaction medium can provide a route to lower oxidation states of uranium, to link uranium and neptunium borate chemistry. Herein we disclose the preparation, crystal structures, and optical properties of two new uranium borates obtained from supercritical water reactions. One of these compounds is the first example of a mixed-valent U(VI)/U(V) borate, thereby bridging uranium and neptunium borate chemistry.

3.2 Experimental

3.2.1 Synthesis

UO_3 (Bio-analytical Industries, 99.5%), $KBO_2{\cdot}nH_2O$ (Alfa Aesar, 99.5% min), B_2O_3 (Alfa Aesar, 99.5% min), and KOH (Alfa Aesar) were used as received. Both uranyl borates were synthesized from reactions carried out in silver ampoules (6.35 cm by 0.635 cm inner diameter). Reactants and mineralizer were loaded into the ampoules and welded shut. The ampoules were loaded into a 27 mL internal volume autoclave, utilizing a Tuttle ‘‘cold seal’’ plunger and counter-pressured with 20.0 mL of deionized water. The autoclave was heated to 600 °C and generated approximately 200 MPa for four days. The autoclave was removed and cooled under house air for 2 hours. The ampoules were removed and opened. Products were flushed out with deionized water. The yield for various phases could not be accurately calculated as residual products and amorphous material adhere to the walls of the ampoule and are compressed into inaccessible pockets due to the high pressure. *Caution: UO_3 used in this study contained depleted uranium; standard precautions for handling radioactive materials should be followed.*

For the synthesis of $K_{10}[(UO_2)_{16}(B_2O_5)_2(BO_3)_6O_8]{\cdot}7H_2O$ (**1-SCWUB**), a total of 178 mg of UO_3 (47.1 mg, 0.16 mmol) and $KBO_2{\cdot}nH_2O$ (131.1 mg, 1.60 mmol) (molar ratio 1:10) was loaded into a silver ampoule. 0.4 mL of 1 M KOH was added before the ampoule was sealed. Yellow rod shaped crystals were isolated for further study in an estimated 50% yield.

For the synthesis of $K_{13}[(UO_2)_{19}(UO_4)(B_2O_5)_2(BO_3)_6(OH)_2O_5]{\cdot}H_2O$ (**2-SCWUB**), a total of 220 mg of UO_3 (68.4 mg, 0.25 mmol) and B_2O_3 (177.0 mg, 2.5 mmol) (molar ratio 1:10) was loaded into an silver ampule. 0.4 mL of 1 M KOH was added before the ampoule was sealed. Dichroic black/amber tablet shaped crystals were isolated in an estimated 25% yield.

3.2.2 Crystallographic Studies

Crystals suitable for X-ray diffraction were isolated and mounted on CryoLoops with Krytox oil and optically aligned on a Bruker APEXII Quazar X-ray diffractometer using a digital camera. Initial intensity measurements were performed using an IμS X-ray source, a 30 W microfocused sealed tube (Mo Kα, λ = 0.71073 Å) with high-brilliance and high-performance focusing multilayer optics. Standard APEXII software was used for determination of the unit cells and data collection control. The intensities of reflections of a sphere were collected by a combination of four sets of exposures (frames). Each set had a different φ angle for the crystal, and each exposure covered a range of 0.5° in ω. A total of 1464 frames were collected with an exposure time per frame of 10 - 30 s, depending on the crystal. SAINT software was used for data integration including Lorentz and polarization corrections. Absorption corrections were applied using the program SCALE (SADABS). Relevant crystallographic information is listed in **Table 3.1**

3.2.3 UV-Vis-NIR Absorbance Measurements

UV-Vis-NIR spectra were acquired from single crystals using a Craic Technologies microspectrophotometer. Crystals were isolated in Krytox oil and placed on quartz slides. Spectra were collected from 200 to 1100 nm. The exposure times were auto-optimized by the Craic software.

3.2.4 Scanning Electron Microscopy and Energy-Dispersive X-Ray Spectrometry

SEM-EDS images and data were collected using a JEOL 5900 with an XRF energy-dispersive X-ray spectrometer. The energy of the electron beam was set at 29.02 kV, and the spectrum acquisition time was 60 s. Spectra and analysis can be found in Appendix A.

3.3 Results and Discussion

3.3.1 Synthesis

Water becomes a supercritical fluid at 374 °C and 22.4 MPa.[76] It is a unique medium for crystal growth because the decrease of the dielectric constant at supercritical temperatures causes reduced solubility of ions.[88] The supercritical nature of the fluid also leads to rapid mixing of the components. The conditions for hydrothermal reactions in metal vessels are known to favor reducing environments; however, this is poorly understood, and there has been considerable

speculation on the nature of the reducing agent.[89] One possibility is the permeation of H_2 across the metal ampoules from the outside environment.[74] Additionally, the vessel's metal wall may become involved in the reaction resulting in another pathway for the reduction and stabilization of lower-valent metals.[90] The pH of the system is kept basic to prevent oxidation of the silver ampoule, and provides OH^- anions which act as a mineralizer.[55] The combination of temperature, pressure, and pH, drastically shifts the Eh of the system potentially stabilizing unusual species in solution.[74] Furthermore, high temperatures favor BO_3 over BO_4 leading to simpler borate building units.

3.3.2 Structural and Topological Discussion

$K_{10}[(UO_2)_{16}(B_2O_5)_2(BO_3)_6O_8]\cdot 7H_2O$ (**1-SCWUB**) is a layered structure that crystallizes in the polar, orthorhombic space group *Pmc*2_1. The layers are composed of a complex sheet of uranium and boron that propagate parallel to the [*bc*] plane with the inner layer occupied by K^+ cations and water molecules (**Figure 3.1a**). There are eight crystallographically unique uranium sites that lead to the large [*bc*] plane dimensions of 11.9312(3) Å × 23.5320(6) Å. Seven of the uranium centers are surrounded by seven oxygen atoms creating UO_7 pentagonal bipyramidal environments that are fairly distorted in their geometries. The final uranium site is a six coordinate tetragonal bipyramid. The uranyl U≡O bond distances range from 1.79(1) Å to 1.807(8) Å for the seven coordinate pentagonal bipyramids and 1.793(8) Å in the tetragonal bipyramid. The equatorial interactions range from 2.16(1) to 2.60(1) Å and 2.22(1) to 2.34(1) Å in the pentagonal and tetragonal bipyramids, respectively.

The sheet topology in $K_{10}[(UO_2)_{16}(B_2O_5)_2(BO_3)_6O_8]\cdot 7H_2O$ is quite complex. An anion topology representation of the layers is shown in **Figure 3.1b**. It is possible to separate two slightly different fragments (A and B, as shown in **Figure 3.1b**). Each of these fragments is based on corrugated infinite chains (shown in dark grey on **Figure 3.1b**). These chains are composed of edge-sharing UO_7 pentagonal bipyramids and can be designated as P-chains (pentagonal). The structure of these chains are very similar, but in the B fragment these chains are rotated by 180º compared with the chain orientation in the A fragment. The chains from different fragments are linked through BO_3 triangles (showed in green) and additional UO_6 and UO_7 polyhedra (shown in violet). There are only UO_7 polyhedra within the A fragment and only UO_6 within the B fragments. These additional polyhedra are linked to other U-chains via edge-sharing within the fragments and via corner-sharing between the fragments. Topologically these

additional groups are within the claw-like fragments (shown in orange) and this is a result of U-chains bending. There is only a small difference between UO_6 and UO_7 (mono and bidentate coordination on BO_3 triangle) positions within claw-like fragments that results in the coordination change of uranium atoms. In the topological representation shown in **Figure 3.1b**, the space between A/B fragments is filled by triangular groups (showed in blue) and can be designated as the T-chain (triangular). Summing the chain groups, the topology of $K_{10}[(UO_2)_{16}(B_2O_5)_2(BO_3)_6O_8]\cdot 7H_2O$ sheets can be described as …PTPTPTP…

$K_{13}[(UO_2)_{19}(UO_4)(B_2O_5)_2(BO_3)_6(OH)_2O_5]\cdot H_2O$ (**2-SCWUB**) is a layered structure that crystallizes in the centrosymmetric, orthorhombic space group *Pbam*. The layers are composed of a complex sheet of uranium and boron that propagate parallel to the [*ab*] plane, with the inner layer occupied by potassium atoms and water molecules (**Figure 3.2**). The *b* axis is remarkably long at 49.867(3) Å because there are eleven crystallographically unique uranium sites. Seven of the uranium centers are surrounded by seven oxygen atoms creating UO_7 pentagonal bipyramidal environments that are fairly regular in their geometries. The remaining four uranium atoms are found within UO_6 tetragonal bipyramids, and here the coordination can be highly distorted. The sheet topology is similar to that of $K[(UO_2)_{19}(UO_4)(B_2O_5)_2(BO_3)_6(BO_2OH)_{10}]\cdot nH_2O$;[91] however, **2-SCWUB** lacks the borate groups that bridge between the layers to create the three-dimensional network observed in $K[(UO_2)_{19}(UO_4)(B_2O_5)_2(BO_3)_6(BO_2OH)_{10}]\cdot nH_2O$. The replacement of the BO_3^{3-} linker with OH^- is accompanied by a lowering of the oxidation state of the uranium site to U(V). The U(V) center deviates from the typical uranyl geometry because it has four short equatorial bonds measuring 1.999(13) Å and 2.134(13) Å and two longer axial bonds measuring 2.33(3) Å forming the tetraoxo core geometry (**Figure 3.3**). The assignment of the pentavalent oxidation state to this uranium site is suggested by bond-valence sum calculations as well as spectroscopic data (*vide infra*). The bond-valence sum of the uranium within the $[UO_4(OH)_2]$ unit is 5.2, consistent with U(V). Additionally, in $K[(UO_2)_{19}(UO_4)(B_2O_5)_2(BO_3)_6(BO_2OH)_{10}]\cdot nH_2O$ the U8 site, is present as a pentagonal bipyramid, however in **2-SCWUB** the coordination is better described as six plus one, with four short bonds ranging from 2.25(1) Å to 2.38(2) Å and a long interaction of 2.74(2) Å. The other ten uranium sites are found within classical uranyl cores, UO_2^{2+}, with two short axial bonds and much longer equatorial bonds. These uranyl distances range from 1.805(1) Å to 1.82(1) Å within the pentagonal bipyramids, and from 1.78(1) Å to 1.81(2) Å within the tetragonal bipyramids.

The equatorial interactions range from 2.23(1) Å to 2.73(2) Å, and from 2.17(1) Å to 2.38(2) Å in the pentagonal and tetragonal bipyramids, respectively. The bond-valence sums for these ten sites range from 5.79 to 6.18.

A number of the uranium silicates and germanates prepared in supercritical water are mixed-valent and fall into three different classes. The first of these have ordered sites of different oxidation states, and includes $Rb_3(U_2O_4)(Ge_2O_7)$.[92] In the second group, some of the uranium sites are formally intermediate-valent such as $Cs_2K(UO)_2Si_4O_{12}$.[93] A final group incorporates both ordered sites and intermediate sites such as $Cs_4(U^{V}O)(U^{IV/V}O)_2(Si_2O_7)_2$ and $Cs_x(U^{V}O)(U^{IV/V}O)_2(Ge_2O_7)_2$.[94] For the structures of the final group, it is probably better to describe these as disordered, as the most likely explanation is that each site represents an average of multiple oxidation states rather than true intermediate-valency. **2-SCWUB** falls into the first category and the mixed-valent site is ordered. It is not entirely clear which group the neptunyl borates, $K_4(NpO_2)_{6.73}B_{20}O_{36}(OH)_2$ and $Ba_2(NpO_2)_{6.59}B_{20}O_{36}(OH)_2{\cdot}H_2O$,[87] fall into, but they are most likely disordered, placing them into the second category.

In contrast to uranyl borates prepared from boric acid flux reactions at much lower temperatures, BO_4 tetrahedral building units are absent in **2-SCWUB**, and only BO_3 triangles are present. In addition, the borate does not form a polymeric network, and instead only BO_3 triangles and dimeric B_2O_5 units are found. The B−O bond distances range from 1.30(1) to 1.43(2) Å. It is well known that high temperatures favor BO_3 units over BO_4. This trend was shown for the uranyl borates prepared by Gasperin using reaction temperatures of ~1150 ºC where all structures contained only BO_3 trianges with only $Ni_7B_4UO_4$ possessing a BO_4 tetrahedra.[95] More recently, high temperature and high pressure studies of the Th-B-O and U-B-O systems have shown the presence of exclusively BO_4 at pressures above 5.5 GPa for thorium and 10.5 GPa for uranium.[96] The prevalence of BO_4 in these structures is a result of the extremely high pressures.

3.3.2 UV-Vis-NIR Absorbance Spectroscopy

The room temperature UV-vis-NIR absorbance spectra shown in **Figure 3.4** have two key regions. At short wavelengths, the classical absorption bands of uranyl exist, the first of these are the equatorial LMCT band centered near 350 nm. The second feature at 450 nm is the vibronically-coupled transitions of the UO_2^{2+} core that have been extensively studied for more than five decades.[14,97] In the spectrum of **2-SCWUB**, but not **1-SCWUB** , there is a third broad

peak centered at 550 nm that arises from the charge transfer of U(V). This transition has been observed in UCl_5 and is characteristic of U(V).[98] The typical *f-f* transitions of U(V) are not exhibited because the uranium resides on an inversion center, which strongly enforces the selection rules (*f-f* transitions are Laporte forbidden).

3.4 Conclusions

The formation of short oxo multiple bonds with metals occurs in order to stabilize high oxidation states. There are, in fact, variations in the number of oxo's required for a given oxidation state. For example, Mo(VI) most commonly has two oxo's to yield the *cis*-molybdenyl unit, MoO_2^{2+}, but molecules containing one oxo and three oxo's are known.[79] Uranyl is similar with two oxo's dominating U(VI) chemistry, yielding the *trans*, UO_2^{2+}, core, however it is possible to stablize U(VI) with a single oxo unit.[99–101] Oxidation states for metals beyond 6+ typically require four oxo atoms as occurs for Np(VII) in $[NpO_4(OH)_2]^{3-}$.[102] The nearly planar nature of this tetraoxo core is unique to the actinide series. Therefore, the question is why is U(V) found within a tetraoxo core like Np(VII)? At most it should only require two oxo's for stabilization; one is probably sufficient. The answer is rather straightforward: These units are not isolated within molecules, but rather are found within extended structures. The four short equatorial bonds are not to terminal oxo's as found in $[NpO_4(OH)_2]^{3-}$, but rather the oxo's bound to U(V) actually bridge between three uranium centers, i.e. they are μ_3-oxo's. Thus, they are in fact helping to stabilize one U(V) and two U(VI) centers.

Both mild and supercritical hydrothermal conditions provide access to U(V) compounds, it appears that there is a stability window for this oxidation state. $K[(UO_2)_{19}(UO_4)(B_2O_5)_2(BO_3)_6(BO_2OH)_{10}]\cdot nH_2O$, for example, was prepared using a reaction temperature that was only 50 ºC higher than that used to prepare $K_{13}[(UO_2)_{19}(UO_4)(B_2O_5)_2(BO_3)_6(OH)_2O_5]\cdot H_2O$ (2-SCWUB).[91] This former compound is similar to **2-SCWUB**, but lacks the U(V) center, and only contains U(VI). In addition to the stability window issue, the syntheses of these compounds are all the more difficult because the reductant is generated *in situ*. The first example of a U(V) compound in this class was intentionally generated by using zinc metal as a reductant.[94] In contrast, in the supercritical reactions, the reducing agent is currently being debated, and hence control is lacking.[74,89,90]

Table 3.1 Crystallographic data for $K_{10}[(UO_2)_{16}(B_2O_5)_2(BO_3)_6O_8]\cdot 7H_2O$ (**1-SCWUB**) and $K_{13}[(UO_2)_{19}(UO_4)(B_2O_5)_2(BO_3)_6(OH)_2O_5]\cdot H_2O$ (**2-SCWUB**).

Compound	1-SCWUB	2-SCWUB
Mass	5555.58	13409.8
Color and habit	Yellow, Tablet	Black, Tablet
Space group	$Pmc2_1$	Pbam
a (Å)	11.9312(3)	13.3979(8)
b (Å)	6.8866(2)	49.867(3)
c (Å)	23.5320(6)	6.9305(4)
V (Å^3)	1933.52(9)	4630.3(5)
Z	2	2
T (K)	100	100
λ (Å)	0.71073	0.71073
Maximum 2θ (°)	27.50	27.31
ρ_{calcd} (g cm^{-3})	4.771	4.809
μ (Mo $K\alpha$), cm^{-1}	340.26	355.22
$R(F)$ for $F_o^2 > 2\sigma(F_o^2)^a$	0.0238	0.0393
$R_w(F_o^2)^b$	0.0563	0.099

$^aR(F) = \Sigma \| F_0 | - | F_c \| / \Sigma | F_0 |$

$^bR(F_0^2) = [\Sigma w(F_0^2 - F_c^2)^2 / \Sigma w(F_0^4)]^{1/2}$

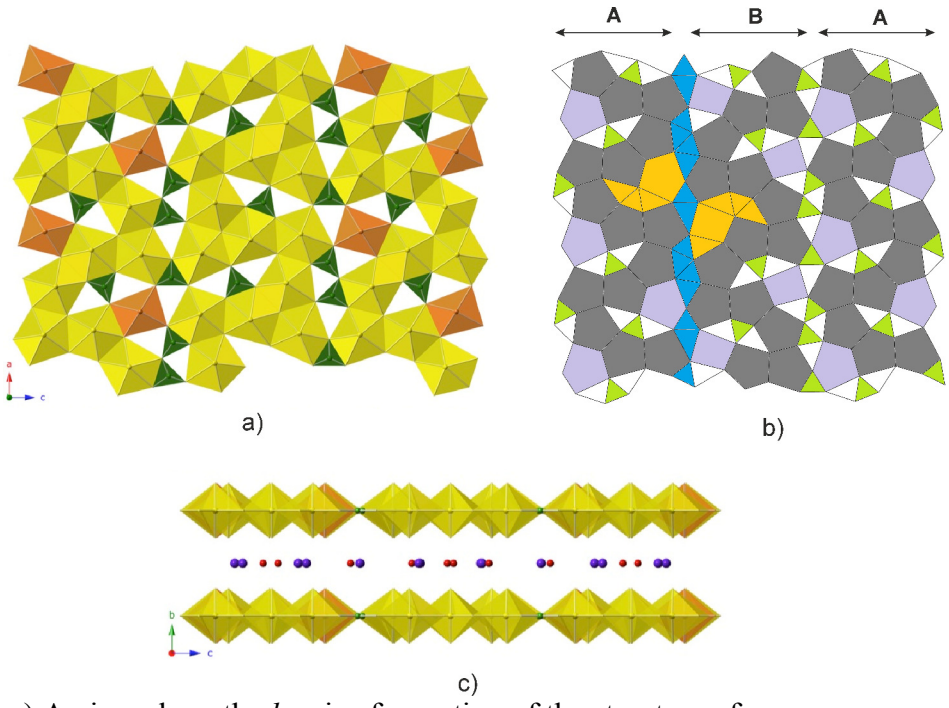

Figure 3.1 a) A view along the *b* axis of a portion of the structure of $K_{10}[(UO_2)_{16}(B_2O_5)_2(BO_3)_6O_8]\cdot 7H_2O$ (**1-SCWUB**) depicting all of the different coordination environments. b) An anionic topology representation of the layer. c) A view of the interlayer containing K^+ cations and water. Uranium is represented by yellow and orange polyhedra, borate as green triangles, oxygen as red spheres, and K^+ by blue spheres

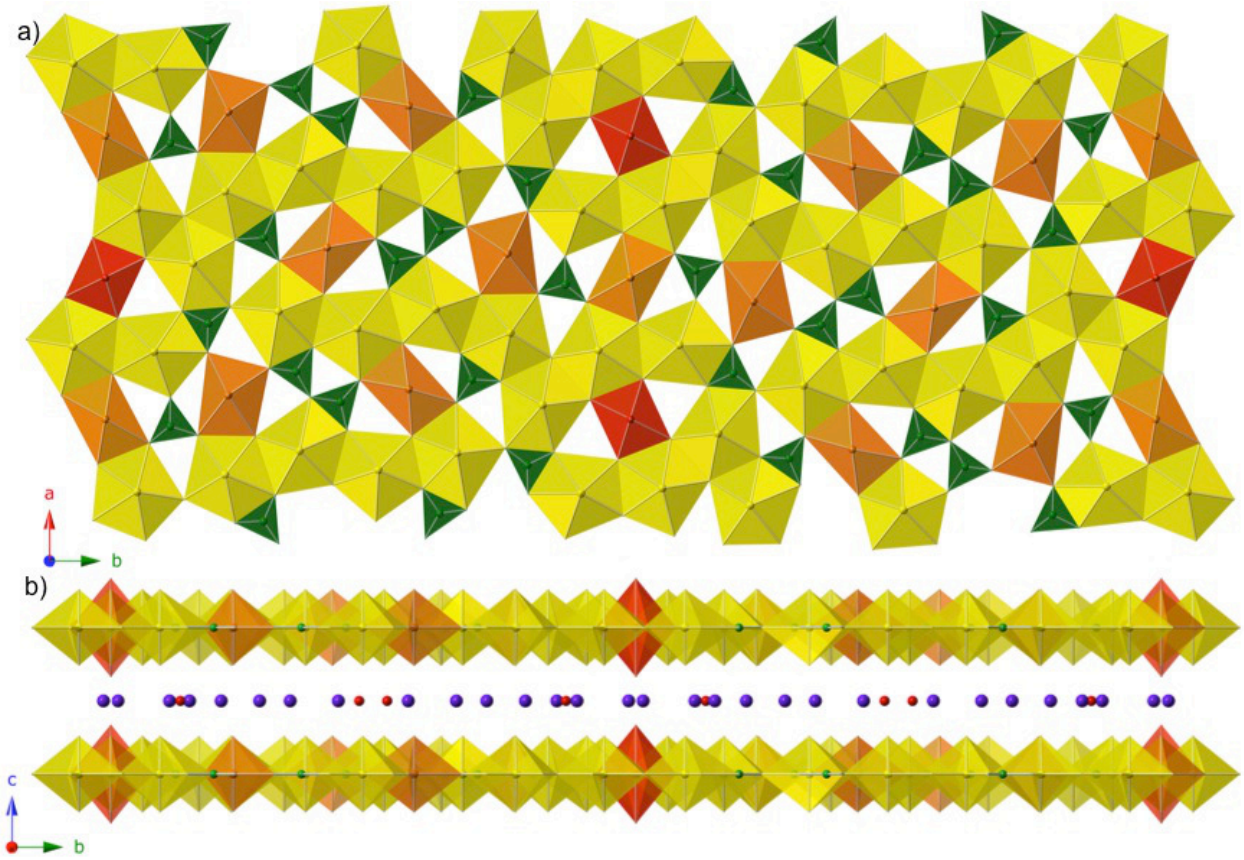

Figure 3.2 a) A view along the [*ab*] plane, showing all the coordination environments. b) A view of the interlayer containing potassium and water. Uranium(VI) is represented by yellow and orange polyhedral, uranium(V) is represented by red polyhedral, borate is represented by green triangles, oxygen is represented by red spheres, and potassium is represented by blue spheres.

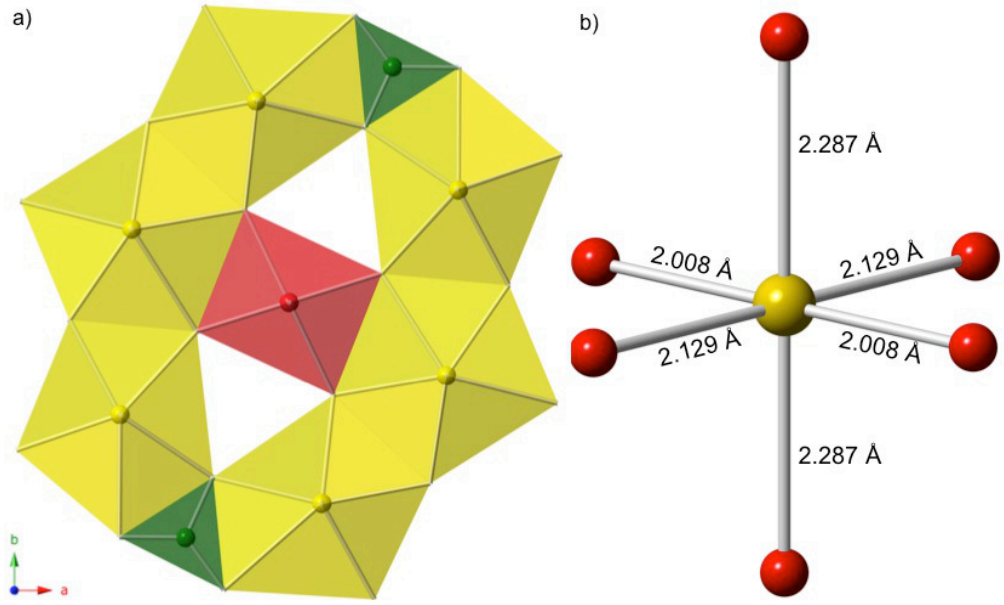

Figure 3.3 a). The coordination environment surrounding the tetraoxo core. b) Ball and stick model of the tetraoxo core showing the four short and two long bonds.

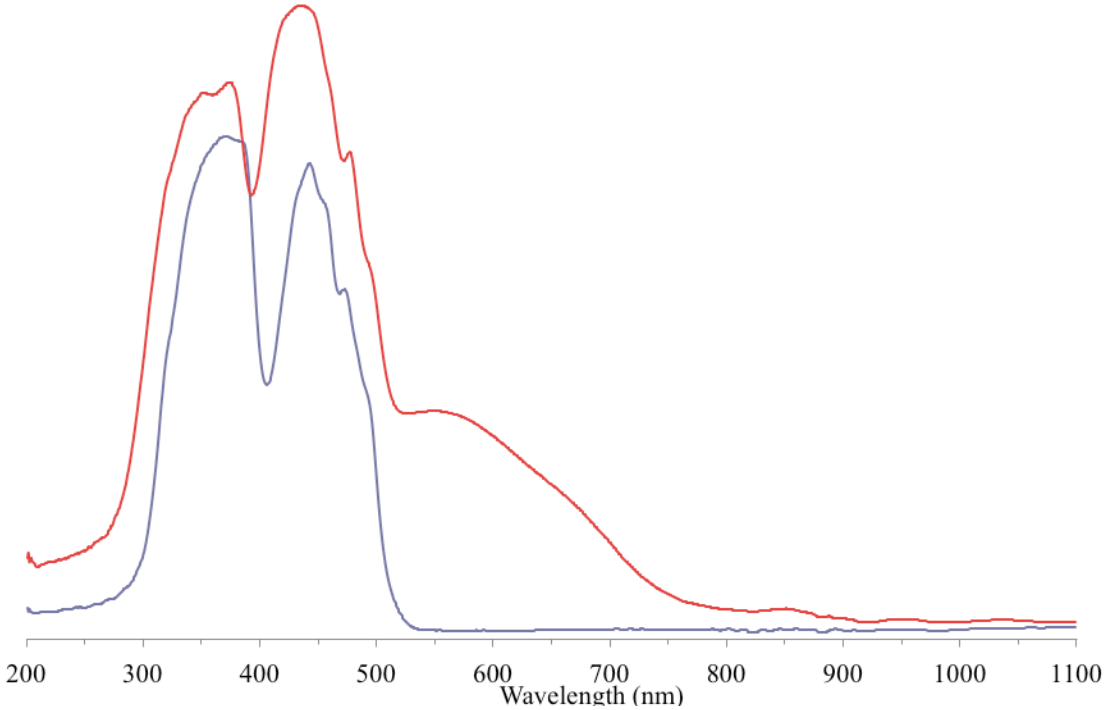

Figure 3.4 UV-vis-NIR absorption spectra for **1-SCWUB** (blue) and **2-SCWUB** (red). The broad feature centered at 550 nm is the charge-transfer band of U(V).

CHAPTER FOUR

HEXANUCLEAR AND PENTANUCLEAR LANTHANIDE PLUMBITE NANOCLUSTERS

4.1 Introduction

Our understanding of metal-ligand interactions in the *f*-block is currently undergoing a rapid transformation with respect to the involvement of the 4*f* and 5*f* orbitals in bonding.[14,20] This is particularly true in complexes and compounds containing divalent lanthanides, where structural and spectroscopic evidence, as well as quantum mechanical calculations of Nd(II) and Dy(II) systems, indicate that the $4f^{n+1}$ and $4f^n5d^1$ configurations are close in energy.[17,103] In an effort to distinguish between the bonding in 4*f* versus 5*f* compounds, we have proposed that bond hyperpolarizabilities can be used as a guide for predicting the extent of covalency in metal-ligand interactions. Transition metal and main-group element bond hyperpolarizabilities have been quantified by the developers of nonlinear optical materials.[48] Our supposition is that the charge of the metal cations creates a similar effect as that of the electric field of light on the polarization of the electrons within a bond. Careful choice of ligands containing bonds capable of large perturbations should give rise to covalent interactions in the 5*f* series either through donation into empty 6*d*, 7*s*, and/or 7*p* orbitals or by delocalization of 5*f* electrons. The largest reported bond hyperpolarizability is for the Pb^{II}–O bond, and we therefore chose this system to test our hypothesis.

Unfortunately, complex lead oxide systems are poorly represented in the literature, especially with *f*-block metals. The rare examples include Pb_6LaO_7X (X = Cl, Br), which contains an unusual cubic coordination environment around La(III), and the cluster $[LaPb_8O(OH)_{10}(H_2O)]^{7+}$, which was recently reported.[104,105] We expand on these previous efforts by reporting the preparation, structures, and properties of $[Ln_6Pb_{18}O_2(OH)_{38}][ClO_4]_{12}\cdot 8H_2O$ (Ln = Y, Sm – Er) and $[Ln_5Pb_{17}(OH)_{36}][ClO_4]_{13}\cdot nH_2O$ (Ln = Tm, Yb, Lu). These compounds represent related families of intricate, lanthanide lead oxyhydroxides that form nano-sized clusters.

4.2 Experimental

4.2.1 Synthesis

All reported lanthanide species were synthesized starting with the respective Ln_2O_3 (Ln = Y, Sm, Eu, Gd, Tb, Dy, Ho, Er, Tm, Yb, and Lu) and were used as received without further purification. A PTFE-lined Parr 4749 acid digestion vessel with a 23 mL internal volume was charged with 0.2 mmol of Ln_2O_3, 1 mmol (223.2 mg) of PbO, and 1 mL of 1M $HClO_4$. The autoclaves were sealed, heated at 180 °C for four days, and cooled at a rate of 10 °C per hour. Products were isolated and washed with ethanol. Estimated yields varied from an estimated 60-90% based on the lanthanide, with holmium having the largest yield.

4.2.2 Crystallographic Studies

Crystals suitable for X-ray diffraction were isolated and mounted on CryoLoops with Krytox oil and optically aligned on a Bruker D8 Quest X-ray diffractometer using a digital camera. Initial intensity measurements were performed using a IμS X-ray source (MoKα, λ = 0.71073 Å) with high-brilliance and high-performance focusing multilayered optics. Standard APEXII software was used for determination of the unit cells and data collection control. The intensities of reflections of a sphere were collected by a combination of four sets of exposures (frames). Each set had a different φ angle for the crystal, and each exposure covered a range of 0.5° in ω. A total of 1464 frames were collected with an exposure time per frame of 20-60 s, depending on the crystal. SAINT software was used for data integration including Lorentz and polarization corrections. Absorption corrections were applied using the program SCALE (SADABS). The structure was solved by direct methods and refined on F2 by full-matrix least squares techniques using the program suite SHELX.

4.2.3 UV-Vis-NIR and Photoluminescence Measurements

UV-vis-NIR and photoluminescence spectra were acquired from single crystals using a Craic Technologies microspectrophotometer. Crystals were placed on quartz slides under Krytox® oil and the data was collected from 200 to 1700 nm. The exposure time was auto-optimized by the Craic software for absorbance and manually set to five seconds for photoluminescence. Photoluminescence data was acquired using the same

microspectrophotometer with an excitation wavelength of 365 nm for terbium and 420 nm for europium and equipped with a Linksys cold stage operating from 25 °C to -193.4 °C.

4.2.4 Magnetic Studies

23.7 mg of powdered $[Ho_6Pb_{18}O_2(OH)_{38}][ClO_4]_{12} \cdot 8H_2O$ was encapsulated in a polycarbonate sample holder and placed in a polycarbonate straw. Magnetometric measurements were taken using a Quantum Design Magnetic Properties Measurement System SQUID. Zero-field cooling and field cooling sequences were performed at 1,000 Oe at temperatures ranging from 1.8 K to 300 K. Polycarbonate sample holder corrections were removed from raw magnetic data. Further treatment of the data was required to acquire χ_M, by removing the diamagnetic contributions from all atoms in the unit cell.[1] Hysteresis was performed for 5 K and 205 K with field sweeps from -5.5 T to 5.5 T.

4.3 Results and Discussions

Two distinct structures form when lanthanide and lead oxides are reacted with perchloric acid. The early lanthanides (Y, Sm –Er) form a hexanuclear cluster of lanthanide atoms encapsulated by a lead cage. The structure shifts to a pentanuclear cluster in the late lanthanides (Tm, Yb, and Lu), resulting in changes to the lead cage.

4.3.1 Structural Discussion

$[Ln_6Pb_{18}O_2(OH)_{38}][ClO_4]_{12} \cdot 8\ H_2O$ (Ln = Y, Sm – Er), **LnPb-1**, crystalizes in the centrosymmetric, monoclinic space group C_2m, **Table 4.1.** The structure is composed of clusters separated by void space occupied by disordered perchlorate and water molecules, **Figure 4.1.** The cluster $[Ln_6Pb_{18}O_2(OH)_{38}]^{12+}$ is overall spherical with a diameter of 12.32 Å. The cluster is composed of a hexanuclear lanthanide center, $[Ln_6(OH)_{32}]^{14-}$ and lead cage $[Pb_{18}O_2(OH)_{30}]^{2+}$, where twenty-four of the bridging hydroxide serve to join the lanthanide core to the lead cage, **Figure 4.2.**

Examining the lanthanide hexanuclear cluster reveals that it is composed of six lanthanide atoms at the vertices of an octahedron with an average Ln-Ln distance of 3.8 Å that centers on a void. Each lanthanide atom has a coordination environment of eight oxygen atoms at an average distance of 2.4 Å, forming a nearly perfect antiprism. Each lanthanide moiety is joined to four neighboring lanthanide moieties via edge sharing, forming a cubic void in the center**.**

The lead cage consists of eighteen lead moieties, each bound by three oxygen atoms at an average distance of 2.3 Å and expresses a stereoactive lone pair to produce a trigonal pyramidal coordination environment. The coordination environment of the lead atoms can be expanded to 3.1 Å, where interactions with the oxygen atoms of the perchlorate ions are observed. The cage is formed by each lead moiety connecting with two or three of its neighboring lead moieties via corner sharing through a bridging hydroxide.

Understanding how the lanthanide core and lead cage are joined is difficult, but the entire cluster can be broken down to a fundamental building block, **FBB-1**, consisting of one square antiprismatic lanthanide moiety and three lead trigonal pyramidal moieties, **Figure 4.3a**. In this building block, the lanthanide moiety shares three of its top edges with the lead moieties. When three **FBB-1** are combine via edge sharing of the lanthanide moieties and joined to the corners of the lead moieties via a μ_3 oxygen atom, half the cluster is formed, **Figure 4.3b**. By combining the two halves, the whole cluster is formed, **Figure 4.3c**. The cage possesses a "window" consisting of seven lead moieties that take the shape of an arrow pointing to the left, **Figure 4.4**.

$[Ln_5Pb_{17}(OH)_{36}][ClO_4]_{13}\cdot nH_2O$ (Ln = Tm, Yb, or Lu), **LnPb-2**, crystalizes in the centrosymmetric, triclinic space group *P*-1, **Table 4.2.** This structure is also composed of clusters separated by void space occupied by charge balancing perchlorate and water molecules; however, the disorder appears to be unique to each element resulting in three different unit cells, **Figure 4.5**. $[Ln_5Pb_{17}(OH)_{36}]^{13+}$ is very similar to $[Ln_6Pb_{18}O_2(OH)_{38}]^{12+}$, but with the loss of a lanthanide center, the overall spherical nature of the former cluster distorted to a domed shape. The diameter at the widest remains 12.33 Å, however the height is 8.41Å, **Figure 4.6a** Breaking the cluster into its components there is a pentanuclear lanthanide center that is capped with a lead atom $[Ln_5Pb(OH)_{28}]^{11-}$ and lead cage $[Pb_{16}(OH)_{28}]^{4+}$, where twenty-four of the bridging hydroxide serve to join the lanthanide core to the lead cage, **Figure 4.6**.

When comparing the pentanuclear cluster to the hexanuclear cluster, one lanthanide center in the octahedral arrangement was replaced by a lead atom, **Figure 4.6b.** While the Ln – Ln distances remain an average of 3.75 Å, the Ln to capping lead distance is 3.83 Å. Again, each lanthanide atom has a coordination environment of eight oxygen atoms at an average distance of 2.35 Å, forming a nearly perfect antiprism. The capping lead atom has a coordination environment of four oxygen atoms averaging 2.36 Å and expresses a stereoactive lone pair, forming a square pyramid.

The lead cage shifts to accommodate the exchange of a lanthanide for lead canter, however the fundamental nature remains the same, **Figure 4.6c.** Lead atoms adopt the trigonal pyramid environment with an average distance of 2.3 Å to three oxygen atoms and express a stereoactive lone pair. Each lead moiety is linked to two neighbors via corner sharing through a bridging hydroxide, this results in a similar arrow shaped "window" as observed in LnPb-1, **Figure 4.7a.** The major deviation from the lead cage in $[Ln_6Pb_{18}O_2(OH)_{38}]^{12+}$, is the expression of a ring, around the vacant lanthanide site, **Figure 4.7b**.

The lead cage shifts to accommodate the exchange of a lanthanide for lead center, however the fundamental nature remains the same, **Figure 4.6c.** Lead atoms adopt the trigonal pyramid environment with an average distance of 2.3 Å to three oxygen atoms and express a stereoactive lone pair. Each lead moiety is linked to two neighbors via corner sharing through a bridging hydroxide, this results in a similar arrow shaped "window" as observed in **LnPb-1**, **Figure 4.7a.** The major deviation from the lead cage in $[Ln_6Pb_{18}O_2(OH)_{38}]^{12+}$, is the expression of a ring around the vacant lanthanide site, **Figure 4.7b**.

While the whole cluster is altered from **LnPb-1**, it can still easily be broken down. The **FBB-1** from the previous structure is retained but a new fundamental building block, **FBB-2**, is observed, **Figure 8a**. FFB-2 is a variation on FFB-1 as it is composed of a lanthanide square antiprism that shares all its top edges with lead moieties. **FBB-2** occupies the top of the structure and is linked to four units of **FBB-1** that occupy the equatorial position of the cluster. These five building units join to form the cluster, leaving a void space at the bottom for the capping lead.

In both structures disordered water and perchlorate molecules occupy the void space between clusters. As with most structures that incorporate crystalized perchlorate anions, the disorder at these sites is endemic to the structure, requiring a number of crystallographic restraints. The disorder results in the Cl-O bond distance varying from 1.23Å to 1.6Å and the O-

CL-O angle ranging from 103.2° to 125.2°. While the primary role of perchlorate is as a counter ion, interactions with the lead atoms ranging from 2.68Å to 3.18Å, suggest a potential structural role as well.

4.3.2 UV-Vis-NIR Absorption and Photoluminescence Spectroscopy

The absorption spectra for each lanthanide cluster were obtained using a microspectrophotometer. Each spectra exhibits the characteristic Laporte forbidden *f-f* transitions throughout the UV-Vis-NIR region, as assigned by Binnemans *et al.*[106] The absorption spectra for $[Ho_6Pb_{18}O_2(OH)_{38}][ClO_4]_{12}\cdot 8\ H_2O$, is shown in **Figure 4.9**, and is representative of the sharp *f-f* transitions observed for all the clusters. All absorption spectra are located in Appendix B

The fluorescence of $[Eu_6Pb_{18}O_2(OH)_{38}][ClO_4]_{12}\cdot 8\ H_2O$ and $[Tb_6Pb_{18}O_2(OH)_{38}][ClO_4]_{12}\cdot 8\ H_2O$ were measured at room temperature and at -193.4 °C. For the spectra at room temperature the intensity of fluorescence is greatly reduced as the bridging hydroxides allow for vibrational relaxation; however upon cooling there is an increase in intensity as the bridging hydroxides become thermally constrained, resulting in better resolution of the peaks. For both europium, **Figure 4.10,** and terbium, **Figure 4.11**, the observed peaks are well characterized and assigned in the literature.[77,78,107]

4.3.3 Magnetic Characterization

The $[Ho_6Pb_{18}O_2(OH)_{38}][ClO_4]_{12}\cdot 8H_2O$ cluster was selected for magnetic studies as there are three unique holmium atoms within 4.0 Å of each other. In plots of both χ^{-1} vs. T (**Figure 4.12**) and χ * T vs T (**Figure 4.13**), paramagnetic behavior is observed. A Weiss constant of -10.3 K is obtained from the χ^{-1} vs. T plot for temperatures above 100 K. While a negative Weiss constant may indicate slight antiferromagnetism, in this system it is negligible and is not supported by the hysteretic study of the material, **Figure 4.14**. Little to no remnant magnetization and coercivity exists in this sample, and display typical paramagnetic behavior at both 205 K and 5 K.

4.3.4 Structural Comparisons

The hexanuclear lanthanide cluster observed in **LnPb-1** and **LnPb-2** is well documented and can be isolated from a neutralized solution of perchloric acid. While the bond Ln-O bond distances remain on the same order of magnitude, the reported cluster contains a capping μ_6 oxo

in the center of the cluster, make the lanthanides nine coordinate. Despite this lanthanide clusters incorporation into other structures, **LnPb-1** and **LnPb-2** mark the first instance of the full encapsulation of the hexanuclear cluster by a larger cage. Interestingly, the hexanuclear cluster is also observed for both tetravalent thorium and uranium as part overall structures, however isolation of those bare clusters has not been achieved.[108] The hexanuclear clusters observed for thorium and uranium often lack the μ_6 oxo, which is mirrored in **LnPb-1** and **LnPb-2**.[109,110]

Within the literature there are limited instances of structures that incorporate both lanthanide metals and lead and even fewer that incorporate halides. The best examples are Pb_6LaO_7X (X = Cl, Br), $[LaPb_8O(OH)_{10}(H_2O)](NO_3)_7$, and $[LaPb_8O(OH)_{10}(H_2O)](NO_3)_7 \cdot 2H_2O$.[104,105] In both instances, these structures were only reported with lanthanum as a metal, where the lanthanum structure is absent from the series for which **LnPb-1** and **LnPb-2** represent.

For the structure Pb_6LaO_7X (X = Cl, Br), the lanthanide atom occupies an eight coordinate cubic environment, differing from the observed square antiprism in **LnPb-1** and **LnPb-2**. Examining the structure, it composed of columns of lanthanum moieties encapsulated by lead moieties. These columns are joined by the halide atoms to form a two dimensional sheet. The lead atoms adopt a variety of coordination environments, ranging from three to five coordinate. Though the trigonal pyramidal coordination environment is present for lead atoms and the square faced lanthanum moiety is joined to it via edge sharing, there is no observation of **FBB-1** or **FBB-2**.

In the instances of $[LaPb_8O(OH)_{10}(H_2O)](NO_3)_7$ and $[LaPb_8O(OH)_{10}(H_2O)](NO_3)_7 \cdot 2H_2O$, the central unit $[LaPb_8O(OH)_{10}(H_2O)]^{7+}$ is fundamentally the same with only slight alterations in the lead network. For these structures the lanthanum center adopts a nine-coordinate environment that can best be described as a highly distorted tricapped trigonal prism. For the purpose of comparison, the tricapped trigonal prism can be viewed as a capped square antiprism, relating to the coordination observed in the lanthanide centers of **LnPb-1** and **LnPb-2**. The lead atoms adopt a variety of coordination environments including the trigonal pyramidal environment. However the presence of only trigonal faces on the lanthanum moiety prevents the formation of the **FBB-1** or **FBB-2** or any Ln-Pb unit observed in Pb_6LaO_7X, as both possess square faces. Despite the lack of common building units, the lead moieties cluster around the lanthanum atom, forming an isolated cluster. This cluster is charge balanced and linked to other clusters by the nitrate ion, in a similar manner as the perchlorate ions in **LnPb-1** and **LnPb-2**.

In all these examples the lead moieties are directly joined to the lanthanide atoms, forming a complex network or cluster. This network originates and depends on the lanthanide metal, as no lead atoms join one cluster or column to another. The overall structures depend on a halide, perchlorate, or nitrate to join the networks together. Furthermore the column in Pb_6LaO_7X requires that the lanthanum moieties form a edge sharing chain, which when compared to $[LaPb_8O(OH)_{10}(H_2O)](NO_3)_7$, $[LaPb_8O(OH)_{10}(H_2O)](NO_3)_7 \cdot 2\ H_2O$, **LnPb-1,** and **LnPb-2**, suggest that lead moieties would likely form clusters if the lanthanum atoms were isolated.

4.4 Conclusion

We reported the synthesis and characterization of two new lanthanide lead clusters, $[Ln_6Pb_{18}O_2(OH)_{38}][ClO_4]_{12} \cdot 8H_2O$ and $[Ln_5Pb_{17}(OH)_{36}][ClO_4]_{13} \cdot nH_2O$. The clusters exhibit absorption and photoluminescence spectra that are typical of Ln(III) in other structures and shows no signs magnetic interactions between lanthanide centers. Structurally, $[Ln_6Pb_{18}O_2(OH)_{38}][ClO_4]_{12} \cdot 8H_2O$ and $[Ln_5Pb_{17}(OH)_{36}][ClO_4]_{13} \cdot nH_2O$ contribute to evidence that lead oxoanions tend to cluster around metal centers rather than forming three dimensional networks. Owing to this apparent clustering nature and the high polarizability of the lead oxoanions, the analogue reactions with trivalent actinide metals should prove extremely interesting for comparative studies.

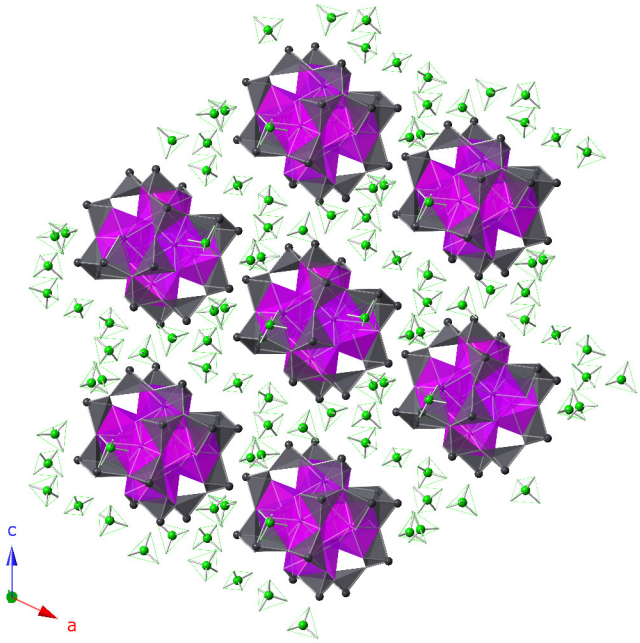

Figure 4.1 A view along the b-axis that shows the cationic cluster $[Ln_6Pb_{18}O_2(OH)_{38}]^{12+}$ and the charge balancing ClO_4 groups. Lanthanide centers are represented by purple polyhedra, lead centers by grey polyhedra, and perchlorate molecules by green spheres.

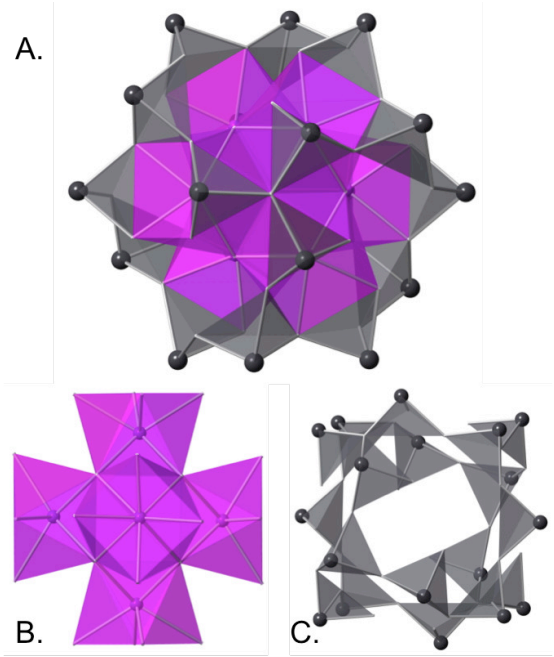

Figure 4.2 a) The cationic cluster $[Ln_6Pb_{18}O_2(OH)_{38}]^{12+}$ centered on the u_3 oxygen. b) The hexanuclear lanthanide core that shows an octahedral arrangement of square antiprisms. c) The eighteen-lead center cage, showing stereoactive lone pairs. Lanthanide centers are represented by purple polyhedral and lead centers by grey polyhedra.

Table 4.1 Crystallographic data for $[Ln_6Pb_{18}O_2(OH)_{38}][ClO_4]_{12}\cdot 8\ H_2O$

Compound	**Y**	**Sm**	**Eu**	**Gd**	**Tb**	**Dy**	**Ho**	**Er**
Mass	12524.47	13261.76	13281.08	13344.56	13364.60	13407.56	13436.72	13464.67
Color and habit	Colorless, block	Colorless, block	Colorless, block	Colorless, block	Colorless, block	Colorless, block	Pink, block	Pink, block
Space group	*C*2/*c*	*C*2/*c*	*C*2/*c*	*C*2/*c*	*C*2/*c*	*C*2/*c*	*C*2/*c*	*C*2/*c*
a (Å)	25.1660(15	25.077(3)	25.0937(13	25.1103(10	25.0295(11	25.091(2)	25.1506(10	25.1114(13
b (Å)	14.5642(9)	14.5993(16	14.6701(8)	14.6723(6)	14.6276(7)	14.6773(14	14.5783(6)	14.5484(8)
c (Å)	28.054(2)	27.891(4)	28.0089(15	28.0401(11	27.9264(17	28.006(4)	28.0413(11	27.980(2)
β (º)	115.3970(1	115.8534(1	114.9697(1	114.9970(1	115.0580(1	114.932(2)	115.3130(1	115.2710(1
V (Å^3)	9288.7(11)	9189(2)	9347.1(9)	9363.0(7)	9262.1(8)	9352.5(17)	9294.3(6)	9243.6(10)
Z	2	2	2	2	2	2	2	2
T (K)	100	296	296	100	296	296	100	296
λ (Å)	0.71073	0.71073	0.71073	0.71073	0.71073	0.71073	0.71073	0.71073
Maximum 2*θ*	30.603	27.520	27.330	30.656	30.582	31.888	30.639	27.679
ρ_{calcd} (g cm^{-3})	4.478	4.793	4.719	4.733	4.792	4.761	4.801	4.838
μ (Mo *K*α)	36.658	37.083	36.712	36.881	37.567	37.461	37.980	38.499
R(*F*) for $F_o^2 > 2\sigma(F_o^2)^a$	0.0512	0.0650	0.0354	0.0456	0.0447	0.0415	0.0544	0.0662
$R_w(F_o^2)^b$	0.0629	0.0871	0.0434	0.0854	0.0765	0.0620	0.1070	0.1224

[a] $R(F) = \Sigma || F_0 | - | F_c || / \Sigma | F_0 |$

[b] $R(F_0^2) = [\Sigma w(F_0^2 - F_c^2)^2 / \Sigma w(F_0^4)]^{1/2}$

Table 4.2 Crystallographic data for $[Ln_5Pb_{17}(OH)_{36}][ClO_4]_{13}\cdot nH_2O$

Compound	Tm	Yb	Lu
Mass	6488.21	6490.74	6744.09
Color and habit	Colorless, sheets	Colorless, sheets	Colorless, sheets
Space group	*P*-1	P-1	P-1
a (Å)	14.195(6)	14.2291(14)	14.2500(10)
b (Å)	15.488(6)	15.5992(15)	14.3033(10)
c (Å)	24.061(9)	24.288(2)	23.8561(17)
α (º)	84.007(8)	83.884(2)	94.008(2)
β (º)	84.320(8)	85.171(2)	94.359(2)
γ (º)	64.416(7)	64.894(2)	116.8910(10)
V (Å^3)	4737(3)	4849.5(8)	4294.2(5)
Z	2	2	2
T (K)	100	100	100
λ (Å)	0.71073	0.71073	0.71073
Maximum 2*θ* (º)	27.638	27.284	31.543
ρ_{calcd} (g cm^{-3})	4.549	4.445	5.216
μ (Mo *K*α)	35.211	34.637	42.497
$R(F)$ for $F_o^2 > 2\sigma(F_o^2)^a$	0.0643	0.0413	0.0503
$R_w(F_o^2)^b$	0.1096	0.0633	0.0776

$$^{a}R(F) = \Sigma \,||F_0| - |F_c|| / \Sigma |F_0|$$

$$^{b}R(F_0^2) = [\Sigma w(F_0^2 - F_c^2)^2 / \Sigma w(F_0^4)]^{1/2}$$

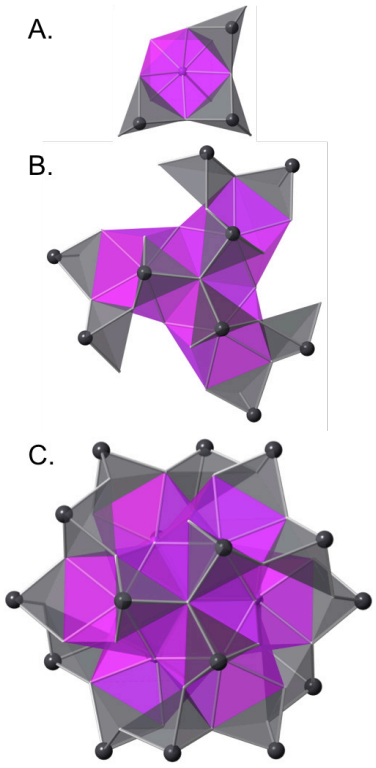

Figure 4.3 Assembly of the cationic cluster $[Ln_6Pb_{18}O_2(OH)_{38}]^{12+}$ a) The fundamental building block (FBB). b) Joining of three FBB's via an μ_3 oxygen to form half a cluster. c) The full cluster, derived from the joining of two half clusters shown in b. Lanthanide centers are represented by purple polyhedral and lead centers by grey polyhedra.

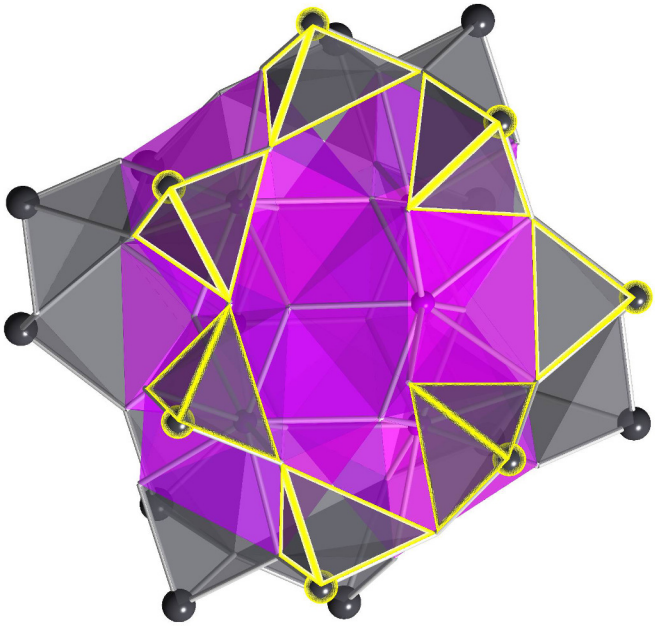

Figure 4.4 A view of the cluster showing the arrow shaped window located in the lead cage, highlighted in yellow. Lanthanide centers are represented by purple polyhedral and lead centers by grey polyhedra.

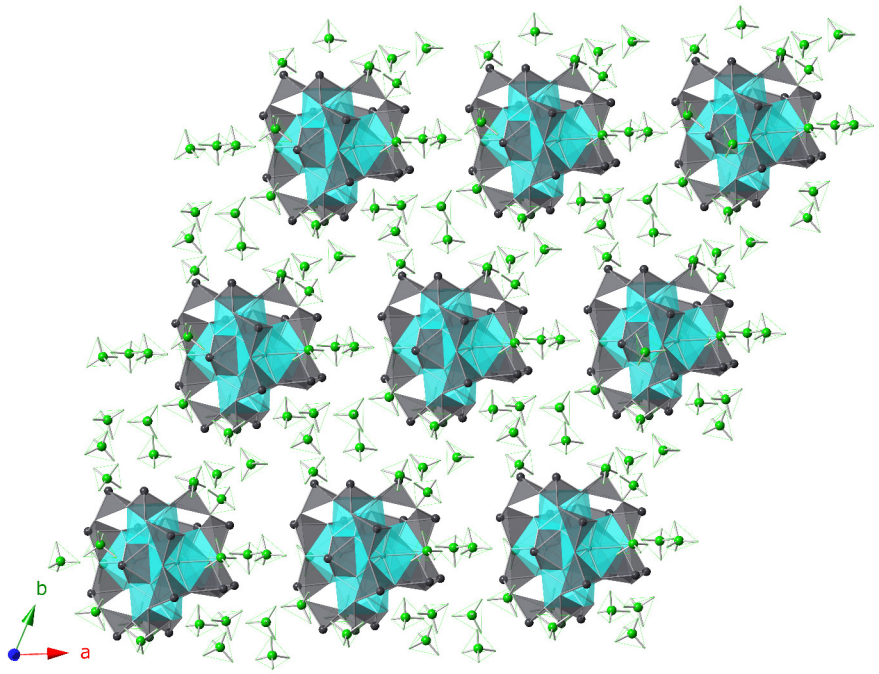

Figure 4.5 A view along the b-axis that shows the cationic cluster $[Ln_5Pb_{17}(OH)_{36}]^{13+}$ and the charge balancing ClO_4 molecules. Lanthanide centers are represented by turquoise polyhedra, lead centers by grey polyhedra, and perchlorate groups by green spheres.

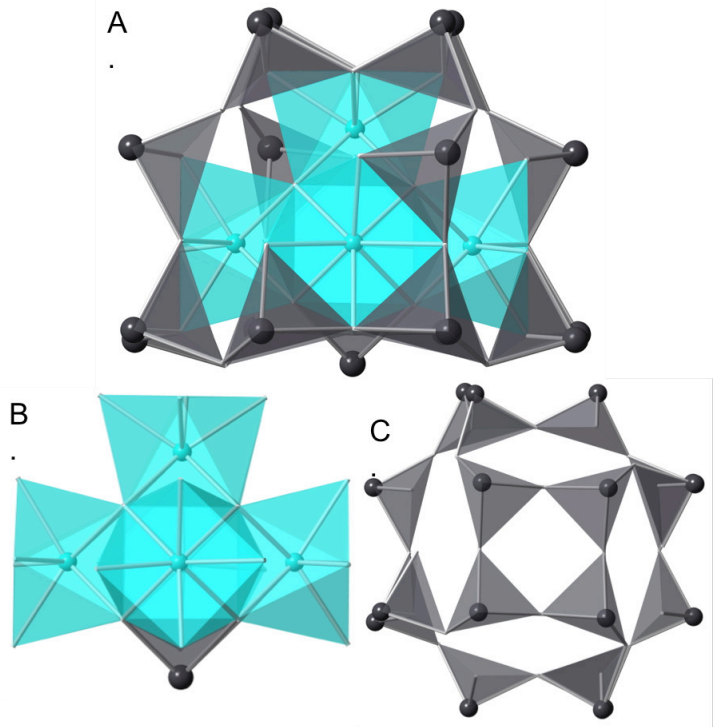

Figure 4.6 a) The cationic cluster $[Ln_5Pb_{17}(OH)_{36}]^{13+}$ viewed from the side. b) The pentanuclear lanthanide core capped with a lead atom to retain octahedral symmetry. c) The seventeen lead center cage, showing the open ring of the underside. Lanthanide centers are represented by turquoise polyhedra and lead centers by grey polyhedra.

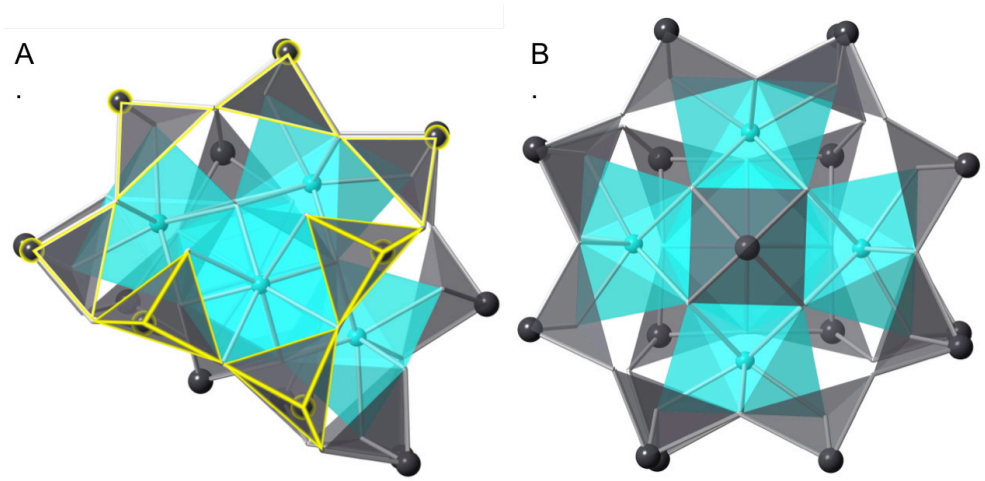

Figure 4.7 a) A view of the cationic cluster $[Ln_5Pb_{17}(OH)_{36}]^{13+}$ showing the arrow shaped window located on all equatorial sides of lead cage, highlighted in yellow. b) The underside of the cationic cluster $[Ln_5Pb_{17}(OH)_{36}]^{13+}$ showing the capping lead center encompassed by the open ring of the lead cage. Lanthanide centers are represented by turquoise polyhedra and lead centers by grey polyhedra.

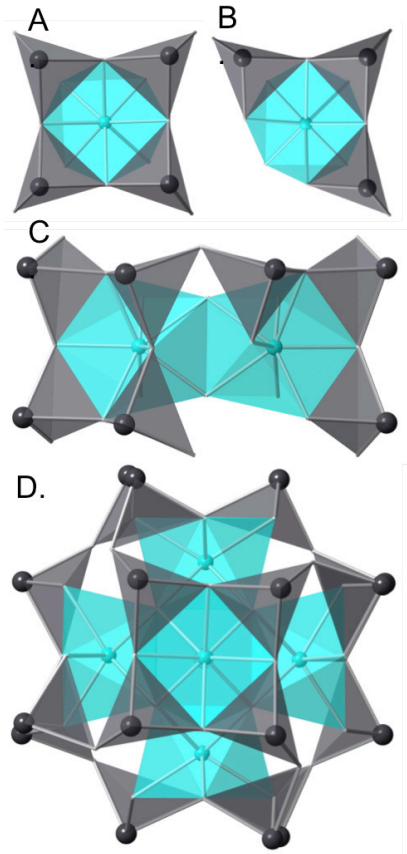

Figure 4.8 Assembly of the cationic cluster $[Ln_5Pb_{17}(OH)_{36}]^{13+}$ a) A new fundamental building block (**FBB-2**). b) The fundamental building block (**FBB-1**). c) Joining of **FBB-1** and **FBB-2** to form the basis of the cluster. d) The addition of 3 more units of **FBB-1** to structure C completes the cluster. Lanthanide centers are represented by turquoise polyhedra and lead centers by grey polyhedra.

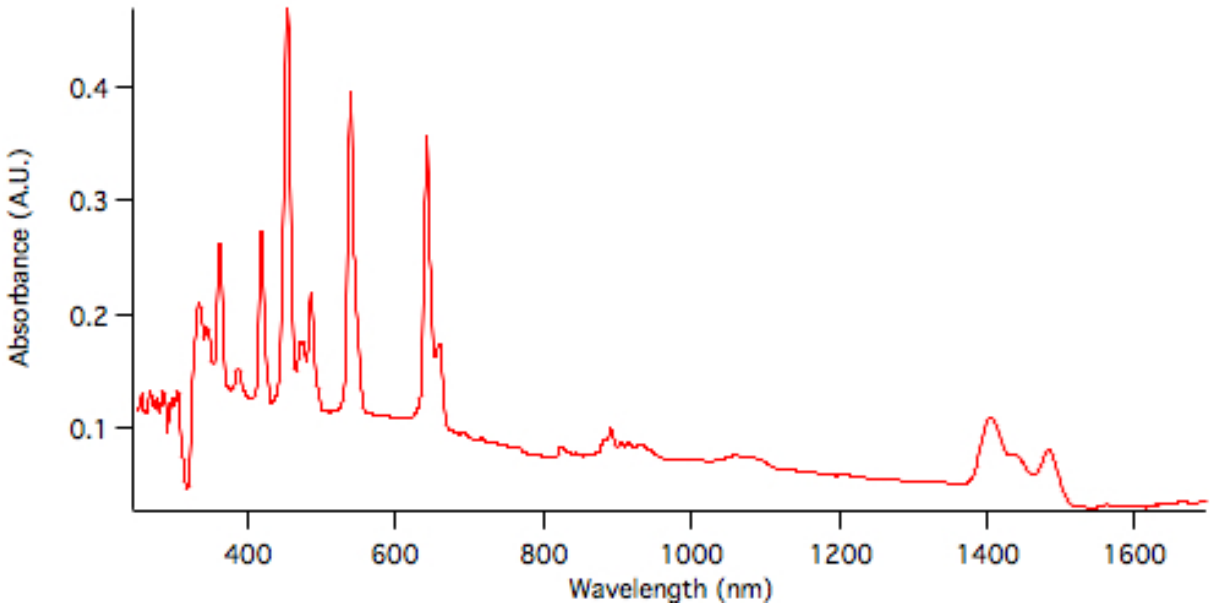

Figure 4.9 UV-Vis-NIR absorbance spectrum of $[Ho_6Pb_{18}O_2(OH)_{38}][ClO_4]_{12}\cdot 8\ H_2O$ displaying characteristic sharp *f-f* transitions.

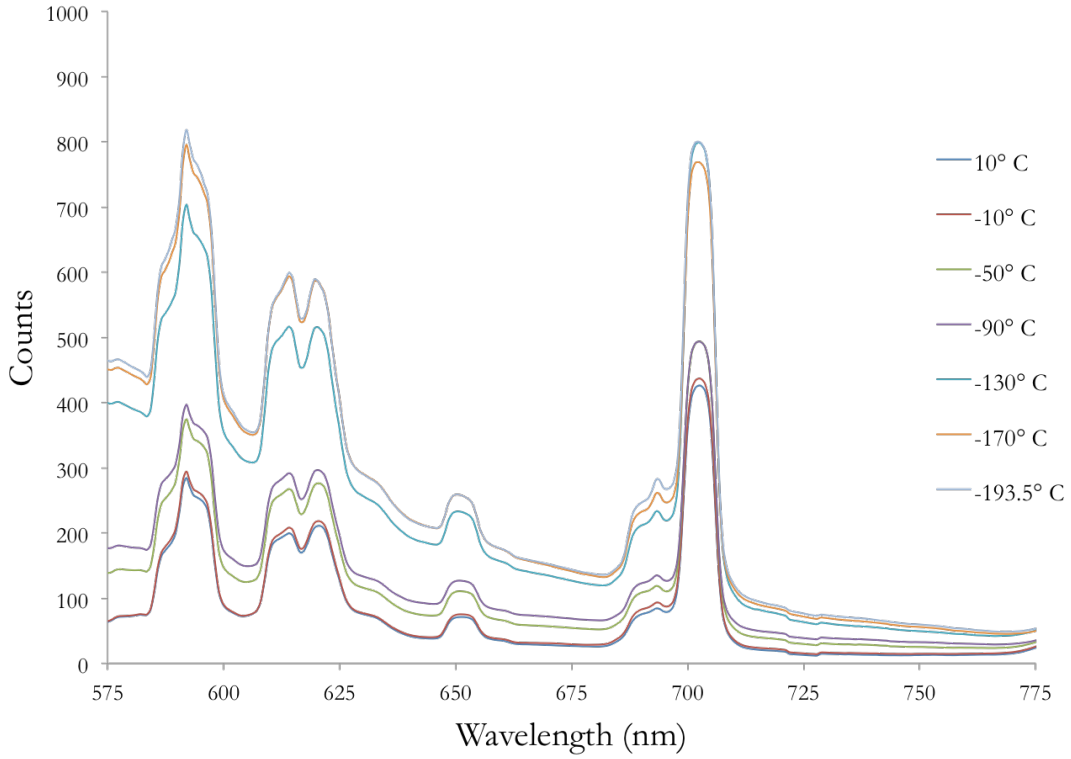

Figure 4.10 $[Eu_6Pb_{18}O_2(OH)_{38}][ClO_4]\cdot 8H_2O$ fluorescence when excited at 420 nm from 10 °C to -193.5 °C.

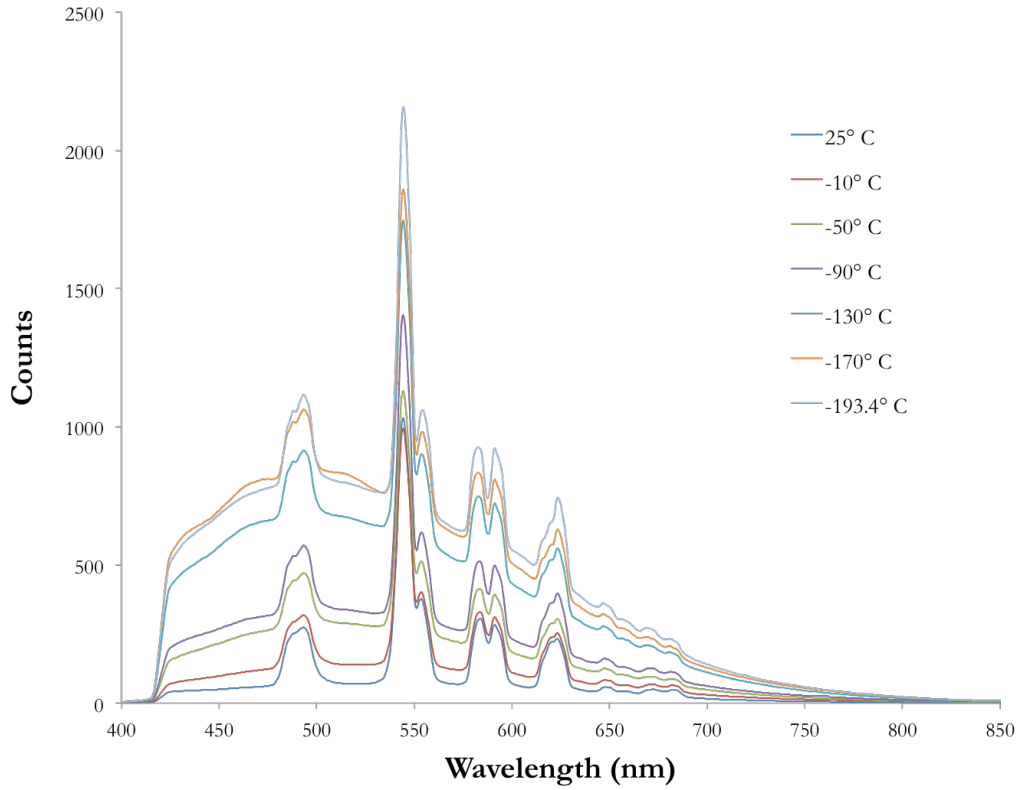

Figure 4.11 [$Tb_6Pb_{18}O_2(OH)_{38}$][ClO_4]·$8H_2O$ fluorescence when excited at 365 nm from 25 °C to -193.4 °C.

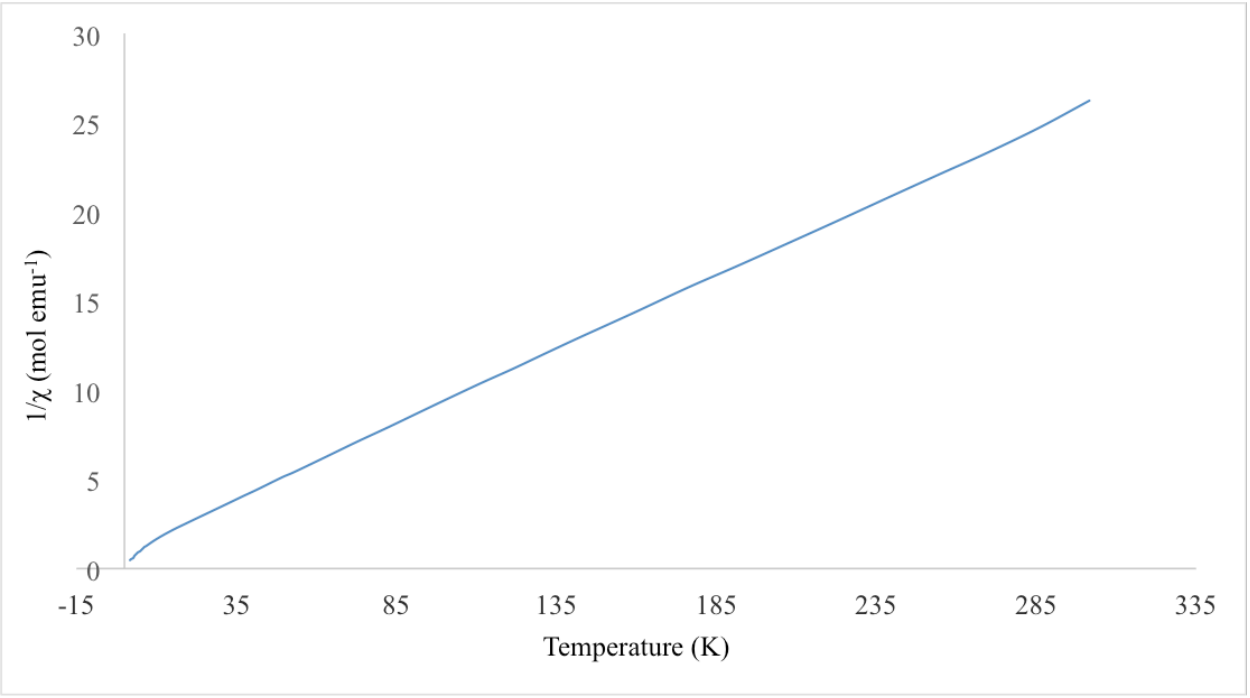

Figure 4.12 A plot of $1/\chi$ versus temperature for [$Ho_6Pb_{18}O_2(OH)_{38}$][ClO_4]$_{12}$·$8H_2O$, when fitted for Curie-Weiss behavior above 100 K Weiss constant of -10.3 is obtained.

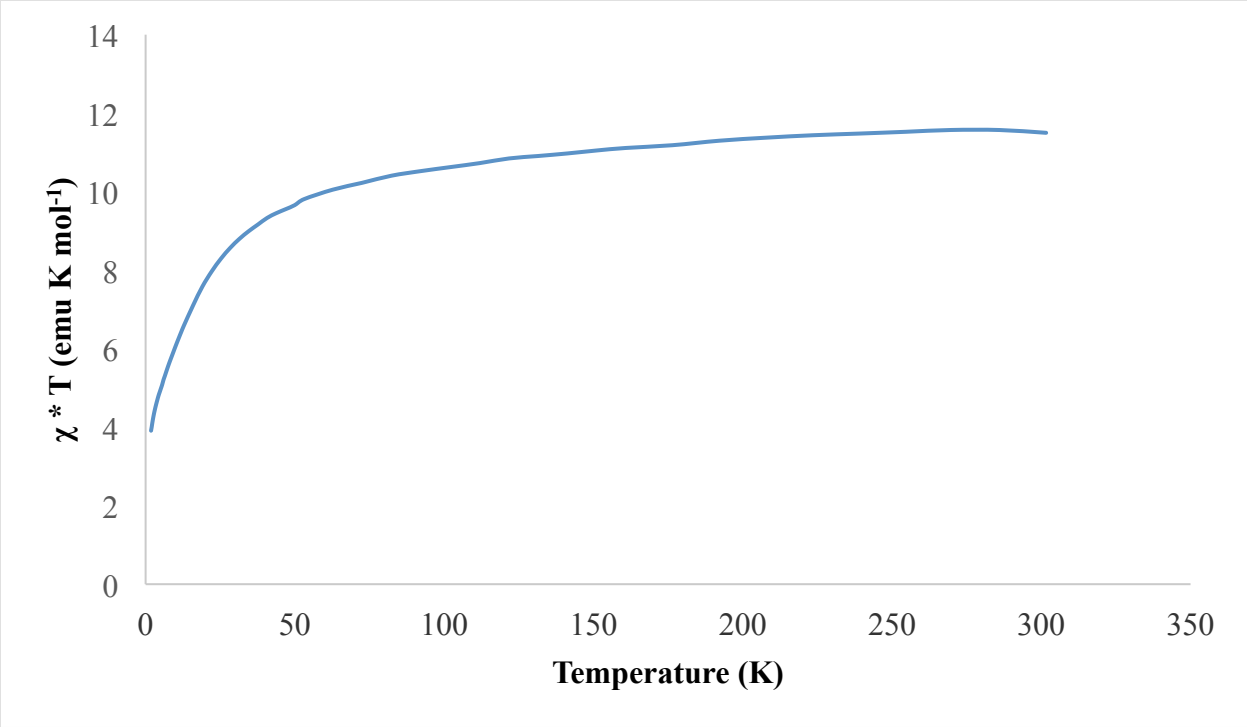

Figure 4.13 A plot of $\chi \cdot T$ versus temperature for $[Ho_6Pb_{18}O_2(OH)_{38}][ClO_4]_{12} \cdot 8H_2O$ displaying paramagnetic behavior.

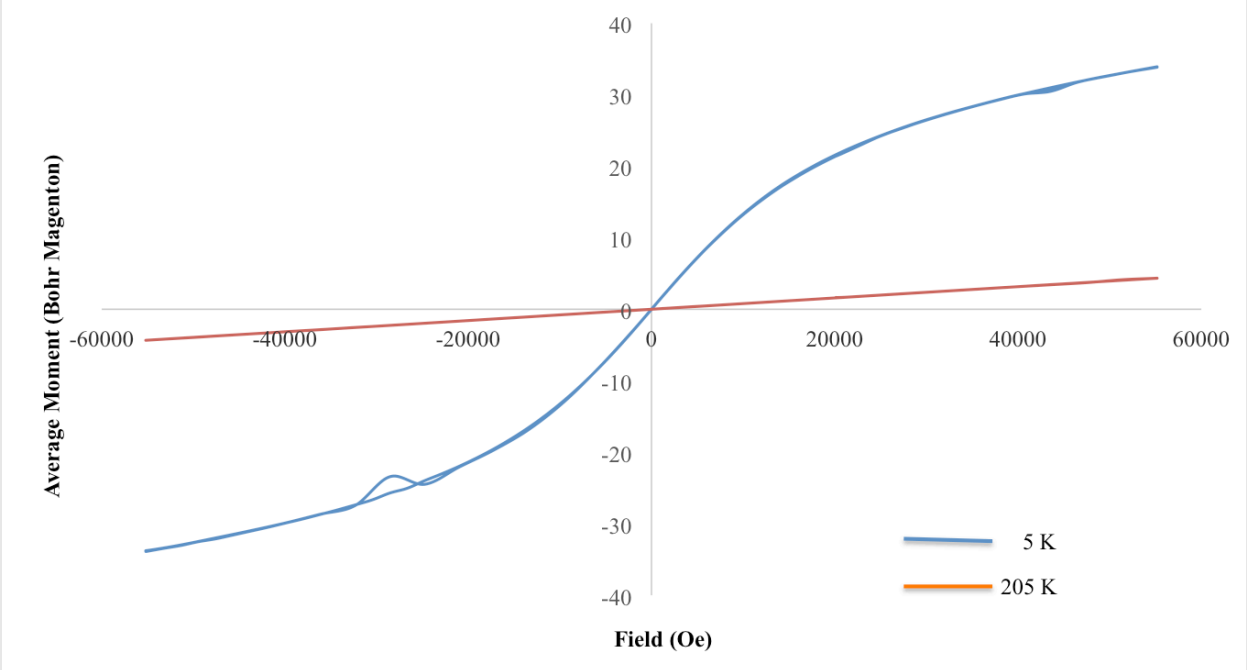

Figure 4.14 Hysteresis for $[Ho_6Pb_{18}O_2(OH)_{38}][ClO_4]_{12} \cdot 8H_2O$ at 205 K and 5 K showing no remnant magnetization.

CHAPTER FIVE

UNUSUAL STRUCTURE, BONDING, AND PROPERTIES IN A CALIFORNIUM BORATE

Adapted with permission from Polinski, M. J.; Iii, E. B. G.; Maurice, R.; Planas, N.; Stritzinger, J. T.; Parker, T. G.; Cross, J. N.; Green, T. D.; Alekseev, E. V.; Cleve, S. M. V.; Depmeier, W.; Gagliardi, L.; Shatruk, M.; Knappenberger, K. L.; Liu, G.; Skanthakumar, S.; Soderholm, L.; Dixon, D. A.; Albrecht-Schmitt, T. E. *Nat Chem* **2014**, *6* (5), 387–392.

5.1 Introduction

Californium is currently the heaviest element that exists on Earth, and is the last member of the actinide series with an isotope long-lived enough for work to be carried out in a standard radiological facility. Typically, synthetic studies on californium chemistry have been restricted to microgram scales, and detailed measurements that correlate structure and physicochemical properties are lacking. The limited number of examples of californium compounds can be ascribed to a variety of factors, which include the low isotopic availability of this element, the short half-life of the longest-lived available isotope (^{249}Cf = 351 years), and its extreme α and γ emissions (6.194 MeV and 0.388 MeV, respectively).

Only five single-crystal structures have been determined: $Cf(IO_3)_3$,[111] the orthorhombic and hexagonal forms of $CfCl_3$,[112] $Cf(Cp)_3$ (Cp = cyclopentadienyl),[34] and $[Cf(H_2O)_9][CF_3SO_3]_3$.[113] These compounds have isotypic lanthanide analogues. In the case of $[M(H_2O)_9][CF_3SO_3]_3$ ($M = Ln^{3+}$ or An^{3+}), the bonding is purely ionic, which means that the valence 5*f* orbitals of the actinide cations are non-bonding, much like the 4*f* orbitals of lanthanides.[30,114,115] However, numerous examples, based on structural and spectroscopic evidence, and electronic structure calculations, indicate the involvement of the 6*p*, 6*d* and/or 5*f* orbitals in bonding with actinides to yield metal-ligand bonds that are partially covalent.[20,31,42] An additional impediment in finding covalent bonding with trivalent actinides is that the degree of covalency decreases with the lowering of the oxidation state. Therefore, the effects of covalency with trivalent actinides are expected to be quite small.[20,31] Actinides beyond

plutonium are typically trivalent and their structural chemistry much like that of isoelectronic lanthanides, is thought to be determined solely by their ionic radii.

We have recently demonstrated that highly polarizable ligands, in this case polyborates, are able to form covalent bonds with the trivalent actinides Pu(III), Am(III) and Cm(III), and that this covalency is associated with the formation of structures that are not paralleled by lanthanides. Moreover, these neighboring actinides do not form an isotypic series with each other; each actinide displays unique chemistry.[42] To understand how the bonding changes across the actinide series, we investigated the synthetic, structural, spectroscopic, and quantum chemical properties of a Cf(III) borate and found many unanticipated results.

5.2 Experimental

5.2.1 Synthesis

$Cf[B_6O_8(OH)_5]$ was synthesized using $^{249}CfCl_3$ that was used as received from Oak Ridge National Laboratory. All work was conducted within a negative pressure glovebox and whenever possible the samples were shielded with lead. The sample used produces 1.7 R/hr at 40 mm and therefore represents a serious external hazard that required the experiments to be carefully choreographed to minimize exposure times. $^{249}CfCl_3$ (5 mg of ^{249}Cf) was dissolved in Millipore water (30 μL) and then transferred to a PTFE-lined Parr 4749 autoclave with a 10 mL internal volume. Boric acid (63 mg) was added to the droplet containing the dissolved Cf(III). The mixture was then sealed and heated at 240 ºC for seven days followed by slow cooling to room temperature over a three day period (3 ºC/hr). The furnace for heating the autoclave was also inside the glovebox and surrounded by thick lead sheets. The resulting product consisted of pale green microcrystalline clusters, which was washed using warm water to remove the excess boric acid flux, **Figure 5.1**.

Caution! ^{249}Cf ($t_{1/2}$ = 351 y; specific activity = 4.1 Ci/g), represent a serious health risk owing to its α (6.194 MeV) and more importantly its γ (0.388 MeV) emission, and the emission of its daughters. ^{249}Cf decays to ^{245}Cm ($t_{1/2} = 1.35 \times 10^7$ y) which is a potent α emitter and undergoes spontaneous fission releasing large fluxes of neutrons. All studies with californium were conducted in a laboratory dedicated to studies of transuranic elements. This laboratory is equipped with HEPA filtered hoods and negative pressure glove boxes that are ported directly into the hoods. A series of counters continually monitor radiation levels in the laboratory. The

laboratory is licensed by the Nuclear Regulatory Commission and the State of Florida. All experiments were carried out with approved safety operating procedures. All free-flowing solids are worked with in glove boxes, and products are only examined when coated with either water or Krytox oil and water.

5.2.2 Crystallographic Studies

Single crystals of $Cf[B_6O_8(OH)_5]$ were mounted on cryoloops with epoxy and optically aligned on a Bruker D8 Quest X-ray diffractometer using a digital camera. Initial intensity measurements were performed using a IμS X-ray source (MoKα, λ =0.71073 Å) with high-brilliance and high-performance focusing multilayer optics. Standard software was used for determination of the unit cells and data collection control. The intensities of reflections of a sphere were collected by a combination of multiple sets of exposures (frames). Each set had a different φ angle for the crystal and each exposure covered a range of 0.5° in ω. A total of 2716 frames were collected with an exposure time of 120 s. The SAINT software was used for data integration including Lorentz and polarization corrections. The structure was solved by direct methods and refined on F^2 by full-matrix least squares techniques using the program suite SHELX. Parameters for Californium are not present in the SHELX software and have to be inputted manually. Solutions were checked for missed symmetry using PLATON. Selected crystallographic information can be found in **Table 5.1**.

5.2.3 UV-Vis-NIR and Photoluminescence Measurements

UV-Vis-NIR and photoluminescence data were acquired from a cluster of microcrystals using a Craic Technologies microspectrophotometer. Crystals were placed on quartz slides under Krytox oil, and the data were collected from 400 to 800 nm. The exposure time was auto optimized by the Craic software. Photoluminescence data were acquired using the same microspectrophotometer with an excitation wavelength of 280, 365, 420, and 546 nm, an exposure of 5s, and an aperture size of 103 x 103 μm. Temperature control was achieved by using a Linkam temperature control stage.

5.2.4 Life-Time Measurements

Time-correlated single-photon counting (TCSPC) photoluminescence measurements were carried out using a femtosecond laser system. A Spectra-Physics Tsunami titanium sapphire

oscillator produced pulses that were amplified by a 1 kHz Spitfire regenerative amplifier, producing 800 nm pulses with a temporal duration of 100 femtoseconds. This fundamental output was frequency doubled, producing 400 nm light that was attenuated to submicrojoule pulse energies for TCSPC measurements. Visible photoluminescence was isolated from laser light using several dichroic beam splitters. The isolated photoluminescence was directed to an avalanche photodiode (id -100-20—ULN, ID Quantique), and TCSPC data was acquired using a 16-channel photon correlator (Becker Hickl). The high- and low-energy regions of photoluminescence were separated using band-pass filters. The temporal dynamic range of the time-domain measurements extended from subpicosecond to millisecond time scales. Photoluminescence lifetimes were fitted using in-house software.

5.2.5 Magnetic Measurements

Magnetic measurements were performed on a polycrystalline sample containing 750 μg of ^{249}Cf that was placed in a tightly closed PTFE sample holder, with a Quantum Design SQUID magnetometer MPMS-XL. Constant-field magnetic susceptibility measurements were carried out in an applied field of 0.100 T in the 1.8–380 K temperature range. Field-dependent magnetization was recorded at 1.8 K in the magnetic field varying from 0 to 7 T. The data were corrected for the diamagnetic contribution from the sample holder and constituent elements.

5.3 Results and Discussion

The reaction of $^{249}CfCl_3$ with molten boric acid yields pale-green microcrystals of $Cf[B_6O_8(OH)_5]$ as the only isolated product. This contrasts sharply with Pu(III), Am(III) and Cm(III), which yield $Pu[B_4O_6(OH)_2Cl]$, $Pu_2[B_{13}O_{19}(OH)_5Cl_2(H_2O)_3]$, $Am[B_9O_{13}(OH)_4]\cdot H_2O$ and $Cm_2[B_{14}O_{20}(OH)_7(H_2O)_2Cl]$, respectively.[42] These four lighter actinide borates share a similar structural design of polyborate layers where the actinide centers reside and are bridged by borate anions forming a three-dimensional framework structure. The Pu(III), Am(III) and Cm(III) metal ions are either nine- or ten-coordinate and adopt the highly anisotropic coordination environments with either hula-hoop or capped triangular cupola geometries.[116,117]

5.3.1 Structural Description

The structure of $Cf[B_6O_8(OH)_5]$ bears no similarities with the previously reported trivalent actinide borates. First, the polyborate scaffolding forms one-dimensional chains

fashioned from a new fundamental building unit for *f*-elements, as shown in **Figure 5.2**. This unit consists of four corner-shared BO_4 tetrahedra and two BO_3 triangles. Three chains wrap around each Cf(III) center, which resides on a two-fold site exhibiting C_2 symmetry, to create an eight-coordinate square antiprismatic coordination environment, as shown in **Figure 5.2b** and **Figure 5.3**. Although the eight Cf–O distances are quite similar, ranging from 2.411(5) Å to 2.463(5) Å, the geometry is far from a perfect square antiprism. The Cf(III) centers bridge the borate chains creating sheets, resulting in a layered structure, **Figure 5.2c**. This sharply contrasts with all earlier members of the actinides series, which contain polyborate layers that are linked together into 3D frameworks.

These structural deviations show the smaller-sized Cf(III) cation yielding both a lower coordination number and a more isotropic coordination environment than any observed for lighter actinide borates. Furthermore, although the lanthanide borates containing smaller Ln(III) cations (Ln = Gd to Lu) also form hexaborates, the polyborate forms sheets instead of chains, and the Ln(III) cations are nine-coordinate tricapped trigonal prisms.[67] The complete inability to predict the structure of $Cf[B_6O_8(OH)_5]$ from lanthanide or actinide borates, only serves to demonstrate the complexity of californium and the actinides.

5.3.2 Magnetic Characterization

Magnetic susceptibility measurements were performed on a polycrystalline sample of $Cf[B_6O_8(OH)_5]$ under an applied field of 0.1 T. No evidence of long-range ordering was observed in the temperature range 1.8–380 K, **Figure 5.4**. The data were fitted over the temperature range with a modified Curie-Weiss law, $\chi = C/(T - \theta) + \chi_0$, where C is the Curie constant from which the effective moment (μ_{eff}) is obtained, θ is the Weiss constant, and χ_0 represents the temperature-independent paramagnetism. The best fit, shown as a solid line through the data in **Figure 5.4c** yields values of $\mu_{eff} = 6.7(4)\ m_B$, $\theta = 0.5(2)$ K and $\chi_0 = 4.44(4) \times 10^{22}$ emu·K·mol^{-1}. The small Weiss constant, confirms that there are no significant interactions between californium magnetic moments, a result consistent with expectations based on the structural information. The shortest Cf-Cf distance of 4.625 Å which is too long for direct metal-metal interactions. Additionally, a magnetic superexchange pathway would involve an interaction through a bridging borate anion and is not expected to result in a significant effective coupling.

Within the single-ion regime, $Cf[B_6O_8(OH)_5]$ revealed a 380 K χT value of 25.6 emu·K·mol^{-1} (μ_{eff} = 14.3 μ_B), which is substantially larger than the expected value of 14.2 emu·K·mol^{-1} (μ_{eff} = 10.6 μ_B) calculated for the $^6H_{15/2}$ ground state of the Cf(III) (f^9) ion. Moreover, the χT product is strongly temperature dependent, **Figure 5.4c**, indicating the presence of a large temperature-independent paramagnetic (TIP) term of ~0.0643(5) emu/mol, estimated as a slope of the χT vs T dependence above 250 K. The dominant TIP value is also evident from the temperature dependence of inverse susceptibility that reaches a constant value at higher temperatures, **Figure 5.3b**. Other studies that deal with U(III) suggest that a significant degree of covalency can reduce the observed magnetic moment.[118] Lacking magnetic studies on Cf(III), a comparison with published studies on Dy(III), the $4f^9$ congener of Cf(III), reveals effective moments generally consistent with the full free-ion values; However a few instances of a slightly decreased moments were reported.[119,120] The decreased moments were partially attributed to crystal-field effects as they play a minor role in the moment reduction.[119,120] In $Cf[B_6O_8(OH)_5]$, the relatively low observed magnetic moment is likely attributed to significant covalency between the Cf(III) ion and the borate network.

5.3.3 Optical Spectroscopy

The electronic spectroscopy of $Cf[B_6O_8(OH)_5]$ is rich and the assigned solid-state absorption spectrum taken from a cluster of crystals is shown in **Figure 5.5**.[121] The *f–f* transitions shown are broader than typically observed in *f*-element structures, even at 79 K, and have features attributed to vibronic progression. When a sample of $Cf[B_6O_8(OH)_5]$ is irradiated with 365 or 420 nm light, emission occurs in the green region centered at 525 nm **Figure 5.6**. Significantly weaker luminescence is found in the near infrared at 1,020 nm when 546 nm light is used.

The emission at 525 nm is very broad and has the signature of strong vibronic progressions. The electronic spectra of several lanthanide compounds display vibronic progressions; however, the vibronic progressions in lanthanide compounds are very small and the original electronic transition are broadened by only a few nanometers.[122,123] In the lanthanides vibronic progressions are typically large and usually the electron-phonon coupling strength is only two or three times larger than that found in lanthanides.[122] Therefore the observation of vibronic progression is not necessarily indicative of the coupling between ligand

vibrations and metal orbitals found with transition metals, but is extremely unusual for an *f*-element complex.

At 79 K the J = 5/2 excited state transition to the J = 15/2 ground state is expected to be at most a few nanometers wide, but is approximately 140 nm wide. The broadening observed is more similar to that observed in d-block elements, where considerable covalent interactions are present. Crystalline defects and distortions slightly contribute to inhomogeneous line broadening and prevent the resolution of individual peaks (zero phonon lines and vibronic lines). The crystal-field levels of the ground multiplet (J = 15/2) induce an expected broadening on the order of several hundred wavenumbers, but do not explain the range of the observed transitions that are attributed to vibronic coupling.

Photoluminescence-lifetime measurements were measured in two regions of the emission centered at 525 nm and showed decay time constants of 1.2 ± 0.3 μs and 20 ± 2 μs, **Figure 5.6 Inset**. The shorter time constant originated primarily from high-energy emission (500 nm); the longer time constant was attributed to the low-energy peak (600 nm). These assignments were designated based on data obtained using optical band-pass filters, which allowed emission from the two bands to be separated. Due to the spread of vibronic bands, the decay measured at 600 nm is expected to have contributions from the band that originates at 500nm. However, the decay measured at 500 nm should not be affected by the band originated at 600 nm. These decays are associated with both the luminescence of Cf(III) and energy transfer to the daughter of ^{249}Cf α-decay, ^{245}Cm, which is also excited by 365 or 420 nm light and decays with the longer lifetime. Cooling the sample to 79 K resulted in clear resolution of the two features with the Cf(III) emission centered at 525 nm and the Cm(III) emission centered at 600 nm.

The energy level of Cf(III) J = 5/2 (mainly $^4P_{5/2}$) level lies ~ 20,000 cm^{-1}above the ground state, which corresponds to ~ 500 nm. The next-lower state is about 2,000 cm^{-1} below this. Thus, J = 5/2 is an emitting state even at room temperature. Cf(III) does not have any states with energy levels near 600 nm. The long lifetime of the 600 nm emission band matches with the first excited state of Cm(III), and is also consistent with a large energy gap because there are no low-lying excited states to quench the J = 7/2 emission. For this emission band, non-radiative relaxation is negligible. Furthermore, the intensity of the variation in the two bands as a function of temperature also confirms this assignment. The Cm(III) band does not depend significantly on temperature, whereas the Cf(III) band at 525 nm is highly temperature sensitive because the

energy gap below this emitting level is small. At higher temperature, radiative relaxation is quenched by thermal (phonon) relaxation. Much of the increase in the Cm(III) emission intensity results from energy transfer from Cf(III). Temperature has little influence on the multiphonon progressions of vibronic transitions, which appear in both emission and absorption spectra. Low temperature only eliminates the hot bands that arise from the occupied states above the ground state or the emitting states. Perhaps the most important feature of this is that when Cm(III) is placed in a coordination environment created by Cf(III), strong vibronic coupling is observed. The electronic spectroscopy of $Cm_2[B_{14}O_{20}(OH)_7(H_2O)_2Cl]$, where Cm(III) is in a very different coordination environment than when it is doped into $Cf[B_6O_8(OH)_5]$, lacks these attributes.[42]

5.4 Conclusions

Pu(III), Am(III) and Cm(III), also have been shown form covalent bonds with borate, but do not exhibit substantial changes in their electronic properties with respect to the corresponding free ions. For example, none of these trivalent actinide borates show a large crystal-field splitting of the ground free-ion term. The altered electronic properties discussed in this chapter are currently considered specific to this Cf(III) compound. In a previously reported Pu(III) structure, the delocalization of the electron density between the trivalent actinide and the borate network was quite weak. Additionally the orbital overlap with Pu(III) did not significantly change the electronic properties of Pu(III), as the *f*–*f* transitions were not broadened and vibronic progressions were absent. Similarly for Am(III), the significant overlap between the 6*d* orbitals and oxygen 2*p* orbitals from borate did not alter the 5*f* electron behavior. However, Cm(III) shows the signatures of vibronic progression in the emission spectrum when placed in the same coordination environment as Cf(III), which demonstrates that the coordination environment can play an important role in the properties of trivalent actinide ions. Quantum mechanical calculations, Appendix D, support significant donation of ligand electron density from the oxygen 2*p* to valence orbitals of Cf(III), notably the 6*d* followed by the 5*f* and 7*p*, which suggests the presence of some covalent character in the Cf–O bonds. Owing to the number of ligands in the first coordination shell, about 0.15 e^- is donated to the californium from each ligand. In conclusion, with careful choice of ligands capable of partial covalent bonding with late actinides, we have obtained a unique Cf(III) material that is unprecedented in the *f*-block.

Figure 5.1 Cluster of microcrystals of $Cf[B_6O_8(OH)_5]$.

Table 5.1 Crystallographic data for $Cf[B_6O_8(OH)_5]$

Compound	$Cf[B_6O_8(OH)_5]$
Formula Mass	526.90
Color and habit	Pale green, plate
Space group	*C*2/*c*
a (Å)	6.8495(14)
b (Å)	18.809(4)
c (Å)	7.2113(15)
a (°)	90
β (°)	101.364(7)
γ(°)	90
V (Å^3)	910.9(3)
Z	4
T (K)	130(2)
λ (Å)	0.71073
Maximum 2θ (deg.)	28.48
ρ_{calc}(g/cm^3)	3.842
μ(Mo *K*a) (cm^{-1})	93.82
R(*F*) for $F_o^2 > 2s(F_o^2)^a$	0.0277
$R_w(F_o^2)^b$	0.0547

$^a R(F) = \Sigma \| F_0 \| - \| F_c \| / \Sigma | F_0 |$

$^b R(F_0^2) = [\Sigma w(F_0^2 - F_c^2)^2 / \Sigma w(F_0^4)]^{1/2}$

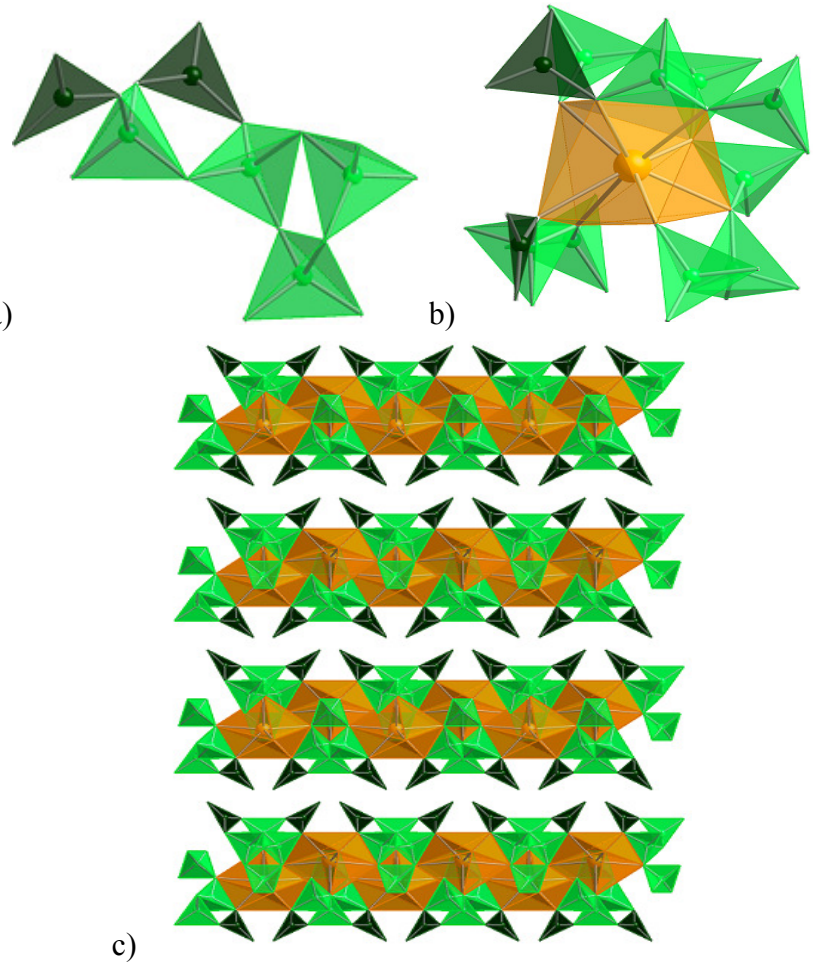

Figure 5.2 Graphical representations of the fundamental building block of borate units a), coordination environment of the Cf(III) b), and overall two-dimensional sheet structure viewed in the *ab* plane c) of $Cf[B_6O_8(OH)_5]$. The BO_3 triangles are depicted by the dark green polyhedra, BO_4 tetrahedra are depicted by light green polyhedra, and the californium square antiprismatic coordination geometry is depicted by orange polyhedra.

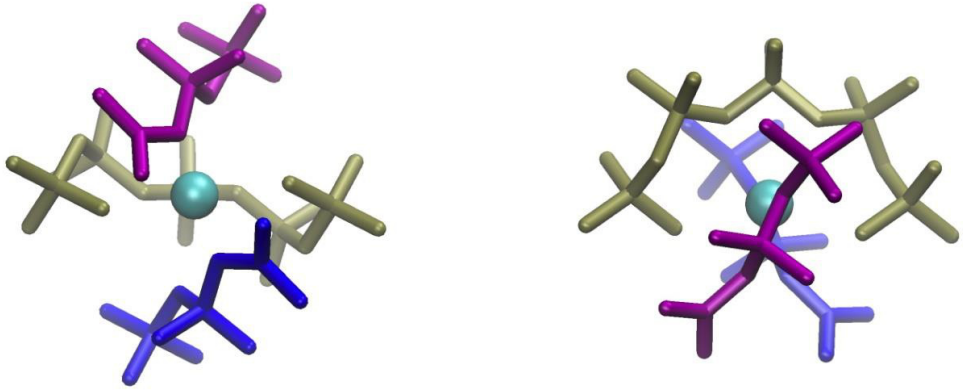

Figure 5.3 Fragment representation of the cluster structure. Left: front view perpendicular to the C_2 axis. Right: top view parallel to the C_2 axis. Ligand fragment with 4 coordinating O (tan), ligand fragments with 2 coordinating O (blue and purple) and Cf (cyan), H atoms have been omitted for clarity.

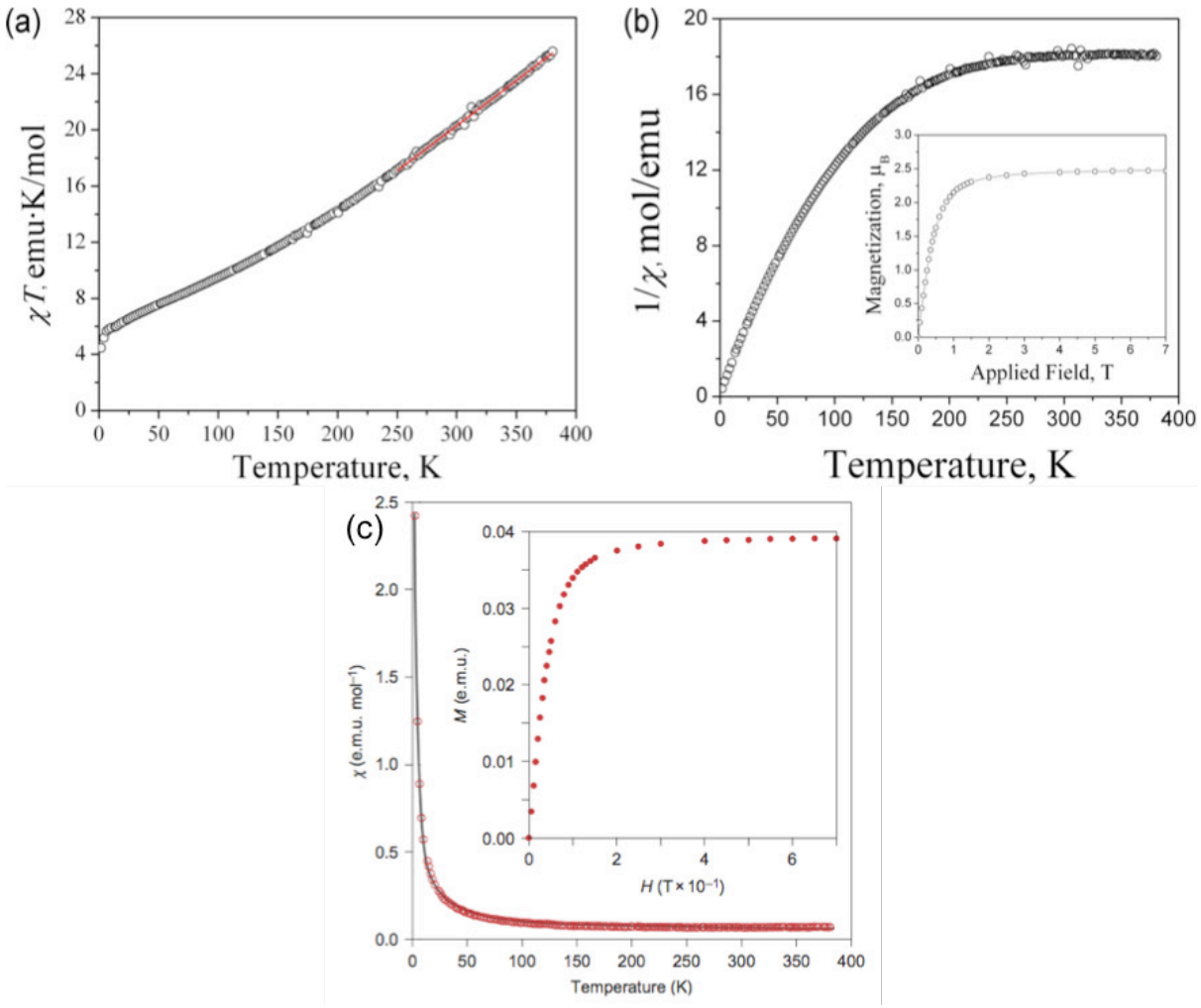

Figure 5.4 Temperature dependence of χT (a) and $1/\chi$ (b) of $Cf[B_6O_8(OH)_5]$. The inset shows the field-dependent magnetization at 1.8 K.

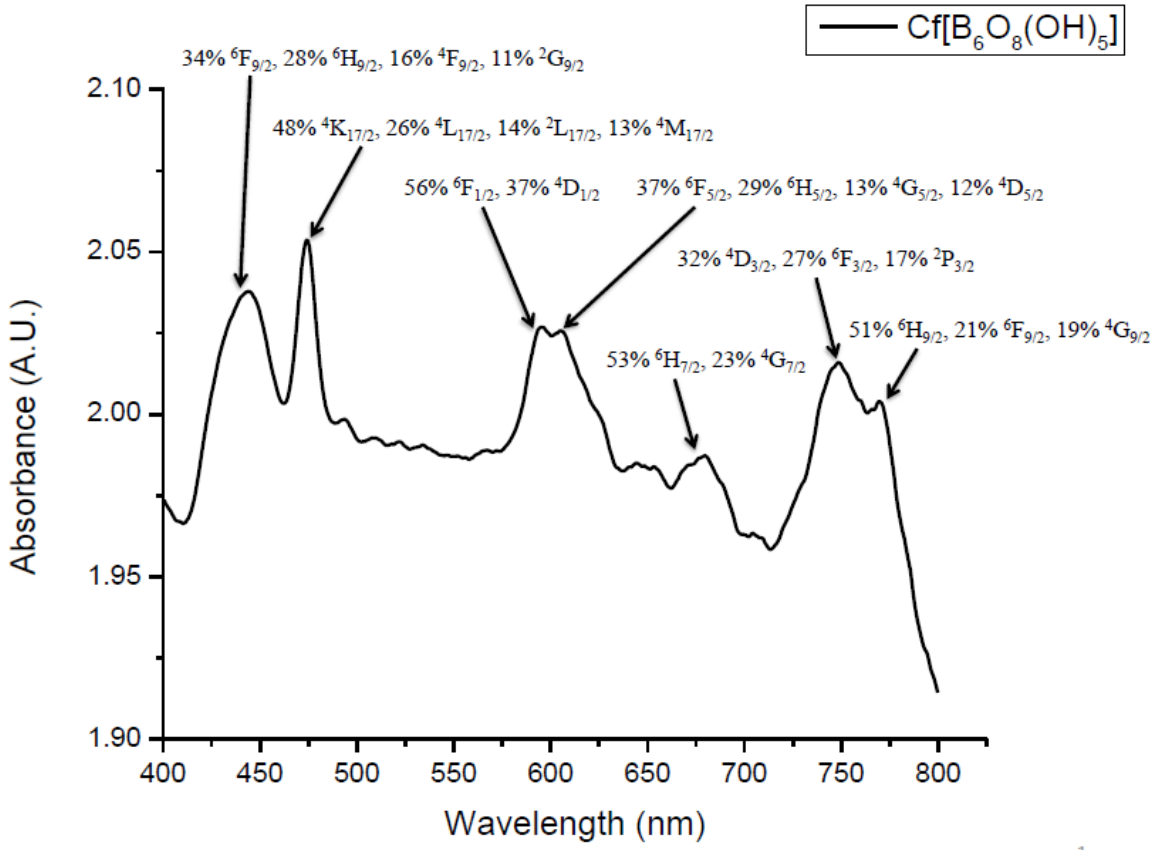

Figure 5.5 Room temperature absorption spectrum of $Cf[B_6O_8(OH)_5]$ showing *f-f* transitions that are characteristic for Cf(III).

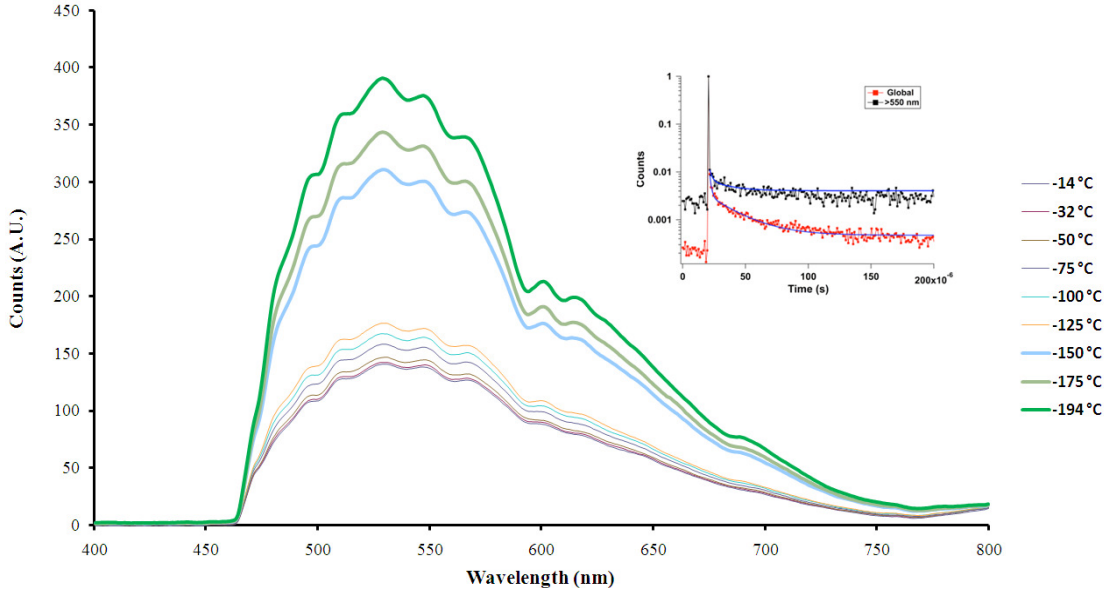

Figure 5.6 Photoluminescence spectra of $Cf[B_6O_8(OH)_5]$ upon excitation with 420 nm light as a function of temperature. The emission from Cf(III) is centered at 525 nm, while the emission from the Cm(III) daughter occurs at 600 nm. Both features show substantial vibronic progressions. The inset shows the decay lifetimes of 1.2 ± 0.3 μs for Cf(III) and 20 ± 2 μs for the Cm(III) daughter.

CHAPTER SIX

CHIRALITY AND POLARITY IN THE *f*-BLOCK BORATES $M_4[B_{16}O_{26}(OH)_4(H_2O)_3Cl_4]$ (M=Sm, Eu, Gd, Pu, Am, Cm, AND Cf)

Adapted with permission from Polinski, M. J.; Pace, K. A.; Stritzinger, J. T.; Lin, J.; Cross, J. N.; Cary, S. K.; Cleve, S. M. V.; Alekseev, E. V.; Albrecht-Schmitt, T. E. *Chem. Eur. J.* **2014**, *20* (32), 9892–9896.

6.1 Introduction

The past decade has seen intense activity directed toward gaining an understanding of the nature of chemical bonds in actinide metals,[14,124] complexes,[8,20,25,31,38] and materials.[24,26,125] Today, a large body of evidence has been gathered that supports 5*f* and 6*d* orbitals being involved in covalent bonding to a degree that is similar to that of *d*-orbitals in transition metal complexes.[8,14,20,24,31,124] In fact, there has been evidence since at least the 1960's and less definitive suggestions since the 1950's, that 5*f* orbitals of the actinides play a role in bonding in some compounds.[14] A fundamental understanding of these phenomena in actinides will have significant impacts on a wide range of areas over time. An immediate application of the differences in bonding between the 4*f* and 5*f* series allows the separation of trivalent lanthanides and actinides from one another; a critical feature of closing advanced nuclear energy cycles.

There are very few systems that extend beyond plutonium in which detailed structural and spectroscopic data have been deeply investigated. In fact, it is only in the halides,[112,126–130] iodate,[111,131,132] triflate,[30,114,115] and borate[41–44,133] series that single-crystal X-ray diffraction data and complementary spectroscopy and theory span from thorium to californium. When the discussion is restricted to actinides in the 3+ oxidation state, the halides, iodates, and triflates are isomorphous with lanthanide analogues, and any changes in structure ostensibly correlates with changes in ionic radii.[30,40,111–115,126–132,134] Additionally, what is lacking are isolable compounds in both series (Pu–Cf) that have different structures even when the radii are the same. Thus far, *f*-elements borates are the only family that achieves this goal. When synthesized by using boric acid fluxes, the lanthanides give three different products depending on the identity and ionic radii of the lanthanide metal under investigation. The early lanthanides (La–Nd) yielded

$Ln[B_4O_6(OH)_2Cl]$, the middle lanthanides (Sm and Eu) yielded $Ln_4[B_{18}O_{25}(OH)_{13}Cl_3]$, and the later lanthanides (Eu–Lu, Y) yielded $Ln[B_6O_9(OH)_3]$.[42] Under the same conditions, the middle-to-late trivalent actinides (Pu-Cm, Cf) yielded $Pu[B_4O_6(OH)_2Cl]$ and $Pu_2[B_{13}O_{19}(OH)_5Cl_2(H_2O)_3]$, $Am[B_9O_{13}(OH)_4]\cdot H_2O$, $Cm_2[B_{14}O_{20}(OH)_7\text{-}(H_2O)_2Cl]$, or $Cf[B_6O_8(OH)_5]$. [41–44,133]

Within a borate network, the lanthanide and actinide series do not entirely parallel one another. More importantly, the later trivalent actinides, Pu(III), Am(III), Cm(III), and Cf(III) display different chemistry from one another as well. Computational investigations of the aforementioned compounds have revealed that the bonding in the lanthanide materials is purely ionic, showing that the 4*f* orbitals are not involved in bonding.[42] The trivalent actinide greatly contrast this as Pu(III) uses its 6*p* orbital to bond with borate, Am(III) and Cm(III) use the 6*d*, and Cf(III) uses the 6*d*, 5*f*, and 7*p*.[41,42]

In an effort to further probe the bonding in actinide borates, a new series of compounds has been synthesized from boric acid flux reactions. This system is saturated with chloride ions in an attempt to force interactions between chlorine and the *f*-element centers. Under these reaction conditions, two different compounds are formed depending on the identity of the *f*-element. When the lanthanides La–Nd are used $Ln[B_4O_6(OH)_2Cl]$ (Ln = La–Nd) is formed which has previously been reported.[42] However, when Sm–Gd, Pu–Cm, and Cf are used, the highly complex, cubic borate $M_4[B_{16}O_{26}(OH)_4(H_2O)_3Cl_4]$ (M = Sm, Eu, Gd, Pu, Am, Cm, Cf) forms. Complex rare-earth oxoanion materials with cubic structures are uncommon, and are very poorly represented with trivalent actinides. This series represents only the third example that extends to californium for which single-crystal structures are known; the others being the aqua complexes and the chlorides. [30,112–115,126–130]

The nine-coordination ionic radii for Nd(III), Sm(III), Eu(III), and Gd(III) are 1.163 Å, 1.132 Å, 1.120 Å, and 1.107 Å, respectively.[10] Additionally, the nine-coordinate ionic radii for Pu(III) and Am(III) are 1.165 Å and 1.162 Å, respectively.[50] Unfortunately, the nine-coordinate ionic radii for Cm(III) and Cf(III) have never been determined and as a result no comparisons to curium and californium can be made. Surprisingly, Sm(III), Eu(III), and Gd(III), which are smaller than Pu(III) and Am(III), form the same compound, whereas lanthanides with similar radii to the actinides mentioned (i.e., Nd) form a different compound, $Ln[B_4O_6(OH)_2Cl]$, under these reaction conditions.

6.2 Experimental

6.2.1 Synthesis

The $M_4[B_{16}O_{26}(OH)_4(H_2O)_3Cl_4]$ compounds were synthesized by using $LnCl_3 \cdot 6H_2O$ (Ln = Sm, Eu, Gd), $^{239}PuCl_3$ (94% ^{239}Pu and 6% ^{240}Pu {along with trace amounts of other plutonium isotopes and ^{241}Am}), $^{243}AmCl_3 \cdot nH_2O$, $^{248}CmCl_3 \cdot nH_2O$ (3% ^{246}Cm), $^{249}CfCl_3 \cdot nH_2O$ as starting materials. $LnCl_3 \cdot {}_6H_2O$ (200 mg) was placed into a PTFE-lined Parr 4749 autoclave with a 23 mL internal volume and dissolved by using 300 mL (3.48 mmol) of concentrated HCl (11.6 M). Approximately 500 mg (8.09 mmol) of H_3BO_3 was then added to the sample. The samples were placed into a box furnace and heated at 240 °C for seven days followed by a slow cooling over a two-day period. The resulting products were then washed extensively with boiling deionized water to dissolve and remove any excess boric acid. After the washing step, large octahedral-shaped crystals of $M_4[B_{16}O_{26}(OH)_4(H_2O)_3Cl_4]$ were left in the bottom of the PTFE liner. The same procedure was also repeated using Ln_2O_3 as the starting lanthanide source, which gave identical results. The yields vary from 30-40% depending on the lanthanide. PXRD data are given in **Figure 6.1**.

In the experiments in which plutonium, americium, curium, and californium were used, a procedure that closely mirrored the reaction for the lanthanide materials was employed. Appropriate actinide starting material (5 mg) was placed into a PTFE-lined Parr 4749 autoclave with a 10 mL internal volume and dissolved by using enough 5 M HCl to completely dissolve the solid. The solid was then reduced to a moist residue by heating at 130 °C ending with a hydrated solid mass of $AnCl_3 \cdot nH_2O$. The $AnCl_3 \cdot nH_2O$ was then dissolved using 30 mL (0.348 mmol) of concentrated HCl (11.6 m). Approximately 70 mg (1.13 mmol) of H_3BO_3 was then added to the sample. The same heating scheme and washing steps preformed for lanthanide reactions were retained for the actinide reactions. The box furnace used for the actinide reactions was in a glovebox for additional containment of the radioactive materials. The resulting product was washed using cold water and consisted of large octahedral crystals for plutonium (blue), americium (pink), curium (pale yellow), and Cf (pale green). Yields cannot be safely determined for transuranium compounds.

Caution! ^{239}Pu ($t_{1/2}$ = 2.411 x 10^4 y), ^{243}Am ($t_{1/2}$ =7.38 x 10^3 y), ^{248}Cm ($t_{1/2}$ =3.48 x 10^5 y), and ^{249}Cf ($t_{1/2}$ = 351 y; specific activity = 4.1 Ci/g) all represent a serious health risk owing to

their α and γ emission and the emission of their daughters. Weapons grade ^{239}Pu decays to ^{235}U ($t_{1/2}$ = 7.04 x 10^8 y) and contains ^{240}Pu ($t_{1/2}$ = 6.56 x 10^3 y) which is a potent α emitter; ^{243}Am decays to ^{239}Np ($t_{1/2}$ = 2.35 d) which is a β- and γ-emitter; ^{248}Cm decays to ^{244}Pu ($t_{1/2}$ = 8.08 x 10^7 y) as well as undergoing spontaneous fission (which accounts for approximately 8% of its decay) releasing a large flux of neutrons that can have a specific activity, up to 100 mRem/hr for the sample size used. ^{249}Cf represents a significant health risk owing to its α (6.194 MeV) and more importantly its γ (0.388 MeV) emission, and the emission of its daughters. ^{249}Cf decays to ^{245}Cm ($t_{1/2}$ = 1.35 x 10^7 y) which is a potent α emitter and undergoes spontaneous fission releasing large fluxes of neutrons. All studies with plutonium, americium, and curium were conducted in a laboratory dedicated to studies on transuranium elements. This laboratory is located in a nuclear science facility and is equipped with HEPA filtered hoods and negative pressure gloveboxes that are ported directly into the hoods. A series of counters continually monitor radiation levels in the laboratory. The laboratory is licensed by the Nuclear Regulatory Commission. All experiments were carried out with approved safety operating procedures. All free-flowing solids are worked with in gloveboxes, and products are only examined when coated with either water or Krytox oil and water. There are significant limitations in accurately determining yield with plutonium, americium, and curium compounds because this requires drying, isolating, and weighing a solid, which poses certain risks, as well as manipulation difficulties given the small quantities employed in the reactions.

6.2.2 Crystallographic Studies

Crystals of all compounds were mounted on Mitegen CryoLoops with Krytox oil and optically aligned on a Bruker APEXII Quazar X-ray diffractometer using a digital camera. Crystals of the transuranium compounds are glued to the CryoLoops. Initial intensity measurements were performed using a IμS X-ray source, a 30 W microfocused sealed tube (Mo Kα, λ = 0.71073 Å) with high-brilliance and high-performance focusing Quazar multilayer optics. Standard APEXII software was used for determination of the unit cells and data collection control. The intensities of reflections of a sphere were collected by a combination of four sets of exposures (frames). Each set had a different φ angle for the crystal and each exposure covered a range of 0.5° in ω. A total of 1464 frames were collected with an exposure time per frame of 30 to 60 s, depending on the crystal. SAINT software was used for data integration including Lorentz and polarization corrections. Semiempirical absorption corrections

were applied using the program SCALE (SADABS). Residual solvent molecules were removed by the Squeeze function in PLATON. Selected crystallographic information is listed in **Table 6.1**.

6.2.3 UV-Vis-NIR and Photoluminescence Measurements

UV-vis-NIR data were acquired from individual crystals using a Craic Technologies microspectrophotometer. Crystals were placed on quartz slides under Krytox oil, and the data were collected from 200 to 1400 nm depending on the compound. The exposure time was auto optimized by the Craic software. Fluorescence data were acquired using the same microspectrophotometer with an excitation wavelength of 420 nm and an exposure time of 1 to 5 seconds.

6.3 Results and Discussion

6.3.1 Structural Discussion

Compound $M_4[B_{16}O_{26}(OH)_4(H_2O)_3Cl_4]$ crystallizes in the polar and chiral, cubic space group, $P2_13$, and contains two crystallographically unique, nine-coordinate *f*-element centers with tricapped trigonal prismatic geometries, **Figure 6.2a**.$M_4[B_{16}O_{26}(OH)_4(H_2O)_3Cl_4]$ is a dense, three-dimensional framework structure, **Figure 6.3a**, composed of corner-sharing BO_3 triangles and BO_4 tetrahedra that bind the *f*-element ion centers. The first metal center (site 1, yellow) has five BO_3 triangles and two BO_4 tetrahedra that corner share to create the bottom and capping units of the trigonal prism. The top of the trigonal prism is created by two crystallographically unique chlorine atoms. The second metal center (site 2, blue) has six BO_3 triangles and three BO_4 tetrahedra that corner-share to create the bottom and capping units of the trigonal prism. The top of the prism is created by three water molecules. The three-fold rotational axis that this second site resides on causes all oxygen atoms from the water molecules, BO_3, and BO_4 moieties to be symmetry related.

The metal centers of site 1 are also joined by chlorine atoms that bridge between two or three metal centers (**Figure 6.2b**) creating a butterfly structure. The μ_3 chloride (Cl1) resides on a threefold rotational axis and, along with one of the Cl2 atoms, allows each of the metal centers to edge share with another symmetrically equivalent metal center. Furthermore, the chloride anions are responsible for part of the trigonal prism.

In $P2_13$, there are four polar threefold axes, as is indicated by the tetrahedral symmetry. Running parallel to each polar axis are three parallel sets of 2_1 screws. **Figure 6.3** shows some of the helices created by the 2_1 screws and threefold axis. In **Figure 6.3a**, these can be best observed by following the yellow polyhedra upwards, and in **Figure 6.3b** by viewing the blue polyhedra. It is important to note that in **Figure 6.3b** the blue metal centers are not in the same plane, but rather there is depth to their arrangement. The metal–oxygen bond lengths observed in this compound are consistent with other bond lengths for *f*-element borates that have been reported **Tables 6.2 and 6.3.** [41–45,133,135–137]

A curious change in coloration was observed for crystals of these compounds when compared with other Pu(III) and Am(III) borates. Compounds $Pu[B_4O_6(OH)_2Cl]$ (*C*c) and $Pu_4[B_{16}O_{26}(OH)_4(H_2O)_3Cl_4]$ ($P2_13$) are both dark blue, whereas $Pu_2[B_{13}O_{19}(OH)_5Cl_2(H_2O)_3]$ ($P2_1/n$) has a very pale blue coloration. In a similar fashion, crystals of $Am_4[B_{16}O_{26}(OH)_4(H_2O)_3Cl_4]$ ($P2_13$) are dark pink, whereas $Am[B_9O_{13}(OH)_4]\cdot H_2O$ ($P2_1/n$) has a pale pink coloration. Although the local coordination environments of the M^{III} centers in these compounds are somewhat different, all are located on general positions in unit cells and the types of ligands are similar. What connects the first set (polar) and last set (nonpolar) of compounds are that the former crystallize in noncentrosymmetric space groups with permanent electric fields (i.e., polar axes or polar planes), and the latter crystallize in centrosymmetric space groups.

6.3.2 UV-Vis-NIR and Photoluminescence Spectroscopy

The ground states of Pu(III), Am(III), and Cf(III) are $^6H_{5/2}$, $^7F_0$, and $^6H_{15/2}$, respectively. The ground state for Cm(III) is more complicated because it is only 87% $^8S_{7/2}$ as spin-orbit coupling mixes in substantial contributions from $^6P_{7/2}$, $^6D_{7/2}$, and higher terms, resulting in crystal-field splittings of about 5–100 cm^{-1}.[14,138] The room temperature absorption spectra of each display a vast series of Laporte forbidden *f-f* transitions throughout the UV-vis- near IR (UV-vis-NIR) region.

The most important transition that occurs for Pu(III) is the $^6H_{5/2} \rightarrow {}^6H_{13/2}$ transition near 900 nm. Fortunately, this region is bare for Pu(IV). The $^4L_{13/2}$ and $^4M_{15/2}$ transitions are also routinely used to identify Pu(III). The most important transitions that occur for Am(III) are the $^7F_0 \rightarrow {}^5L_6$ the $^7F_0 \rightarrow {}^7F_6$ transitions near 500 and 800 nm, respectively. While the chemistry of curium and californium is overwhelmingly dominated by the trivalent state, there are still a

number of diagnostic transitions. For Cm(III), the $^8S_{7/2} \rightarrow 0.88\ ^6I + 0.26\ ^4K_2$ and $^8S_{7/2} \rightarrow 0.64\ ^6I + 0.32\ ^4H_2$, which are between 350 and 425 nm, can be used as diagnostic transitions as these are not present in the spectrum of Cm(IV) while for Cf(III) the $^6H_{15/2} \rightarrow 0.48\ ^4K_{17/2} + 0.26\ ^4L_{17/2} + 0.14\ ^2L_{17/2} + 0.13\ ^4M_{17/2}$, $^6H_{15/2} \rightarrow 0.56\ ^6F_{1/2} + 0.37\ ^4D_{1/2}$ and $^6H_{15/2} \rightarrow 0.32\ ^4D_{3/2} + 0.27\ ^6F_{3/2} + 0.17\ ^2P_{3/2}$ transitions at approximately 475, 600, and 750 nm can be used.[139–141]

The room temperature absorption spectra for $Pu_4[B_{16}O_{26}(OH)_4(H_2O)_3Cl_4]$ and $Am_4[B_{16}O_{26}(OH)_4(H_2O)_3Cl_4]$ can be seen in **Figure 6.4 and 6.5**, respectively. The room temperature absorption spectra for $Cm_4[B_{16}O_{26}(OH)_4(H_2O)_3Cl_4]$ and $Cf_4[B_{16}O_{26}(OH)_4(H_2O)_3Cl_4]$ can be seen in **Figure 6.6 and 6.7**, respectively. It is important to note that for the actinides, the absorption spectrum can be a powerful tool in determination of the oxidation state even when substantially different coordination geometries are observed.

The fluorescence spectrum for $Cm_4[B_{16}O_{26}(OH)_4(H_2O)_3Cl_4]$ and $Cf_4[B_{16}O_{26}(OH)_4(H_2O)_3Cl_4]$ can be seen in **Figure 6.8 and 6.9**, respectively. Cm(III) is one of the most luminescent ions and is known to be strongly fluorescing in the range of 595-613 nm when irradiated with a laser or a mercury-discharge lamp.[14] Cf(III) is known to be luminescent in the green region of the visible spectrum. In the case of $Cm_4[B_{16}O_{26}(OH)_4(H_2O)_3Cl_4]$ the sample was irradiated with 420 nm light normal to the triangular face which produced an approximately 50 nm wide fluorescence peak near 595 nm giving off a yellow-orange color. The fluorescence emission band is attributed to the relaxation of the $^6D_{7/2}$ excited state to the $^8S_{7/2}$ ground state.[14,142,143] The energy of the emission band is known to be dependent on the ligands attached to the Cm(III) ion. [14,142,143] For $Cf_4[B_{16}O_{26}(OH)_4(H_2O)_3Cl_4]$, a bulk sample was irradiated with 420 nm light which produced an approximately 300 nm wide fluorescence peak centered near 525 nm giving off a green color. The two resolved peaks near 500 and 525 nm are most likely due to the two different Cf(III) sites present in this compound.

The fluorescence spectrum of $Eu_4[B_{16}O_{26}(OH)_4(H_2O)_3Cl_4]$ can be seen in **Figure 6.10**. The Eu(III) ion has a $^7F_0$ ground state and is known to give red emission upon excitation. The emission spectrum is composed of the first excited state, $^5D_0$, and the ground septet, ^7F_J (J = 0-4). The $^5D_0 \rightarrow {}^7F_1$ transition is actually split into three peaks (unresolved in Figure SI.3) at 589, 592, and 596 nm. The main transition, $^5D_0 \rightarrow {}^7F_1$, around 614 nm is responsible for the red emission and is also a hypersensitive transition that can be influence by the ligand set.[77,144–146] This

hypersensitivity explains the broadened and unresolved $^5D_0 \rightarrow {}^7F_1$ transition as there are two different Eu(III) centers with different ligands bound to them in $Eu_4[B_{16}O_{26}(OH)_4(H_2O)_3Cl_4]$.

Upon comparing the UV-Vis-NIR absorption spectra recorded at room temperature of the polar and nonpolar compounds (**Figure 6.11**), an enhancement of Laporte forbidden *f–f* transitions was observed in the polar compounds. The *f*-orbitals of the metals are considered to be chemically inaccessible for the lanthanides and the middle-to-late actinides.[14,20,24,106,138,145,147–152] As such, the crystal-field effects of these ions are minimal and often regarded as perturbations of the free ion.[20,24,106,138,145,147–153] The spin–orbit coupling is most pronounced in these ions, and thus these effects lead to what are called "field-free" levels because they represent the spectrum of the given ion.[138,145,147–151] This allows the use the UV–Vis absorption spectrum as not only a means of chemical analysis, but also as a means of oxidation state confirmation as each *f*-element ion exhibits a characteristic absorption pattern that is largely independent of the ligand environment and bonding.

The characteristic Laport forbidden *f–f* transitions are weak with typical molar absorptivity values about 5 M^{-1} cm^{-1}.[138,145,147–151] The enhancement of a large number of these *f–f* transitions in the polar compounds could be a result of several factors. Since these compounds crystallize in a noncentrosymmetric space group, the selection rules are relaxed and the *f–f* transitions should be more intense. Additionally, in a polar space group, a permanent electric field will enhance the electric dipole transitions while magnetic dipole transitions may remain unaffected. This would result in enhancement of only certain transitions, but not all.

Finally, if the *f*-orbitals are mixing with ligand orbitals, the selection rules would be further relaxed. This would likely result in broadened transitions because of vibronic coupling. By comparing the polar and nonpolar spectra above, the enhanced transitions do exhibit both a broadening and redshifting of the peaks. Thus, we propose that these cubic actinide borate compounds may have covalent interactions between the *f*-orbitals and the borate and/or chlorine ligands. To complicate matters further, the number of actinide centers in the asymmetric units are larger in these cubic phases than in some of the other centrosymmetric compounds, and this would certainly affect the relative intensities of the *f–f* transitions.

To fully understand whether or not orbital mixing or the electric field in the crystals are responsible for the *f–f* enhancement observed, band-structure calculations would need to be performed. However, the basis sets for the heavy atoms (i.e., Pu–Cf) are not yet available. It is

our hope over the next few years that the theory and basis sets required to perform these calculations will be available, so that this system can be fully explored and understood.

6.4 Conclusions

Complex compounds containing *f*-elements that crystallize with cubic symmetry are quite rare. A number of interesting features emerge from this set. First, there is an enhancement of the *f*–*f* transitions in the polar compounds in comparison to their nonpolar analogues. We hypothesize that this may be a result of covalent interactions between the 5*f* orbitals of the actinides with either the borate or chloride ligands. Finally, even without quantum mechanical calculations, this work is another demonstration that heavy actinides do not behave simply like their equivalent-sized lanthanide counterparts. This is most easily demonstrated by considering the nine-coordinate ionic radii of Nd(III), Pu(III), and Am(III), which are 1.163 Å, 1.165 Å, and 1.162 Å, respectively. The ionic radii of Nd(III) is between that of Pu(III) and Am(III), yet Nd(III) forms a different compound. This is yet another example of why care must be taken when making assumptions about the chemistry of the mid-to-late trivalent actinides based on the chemistry of the lanthanides.

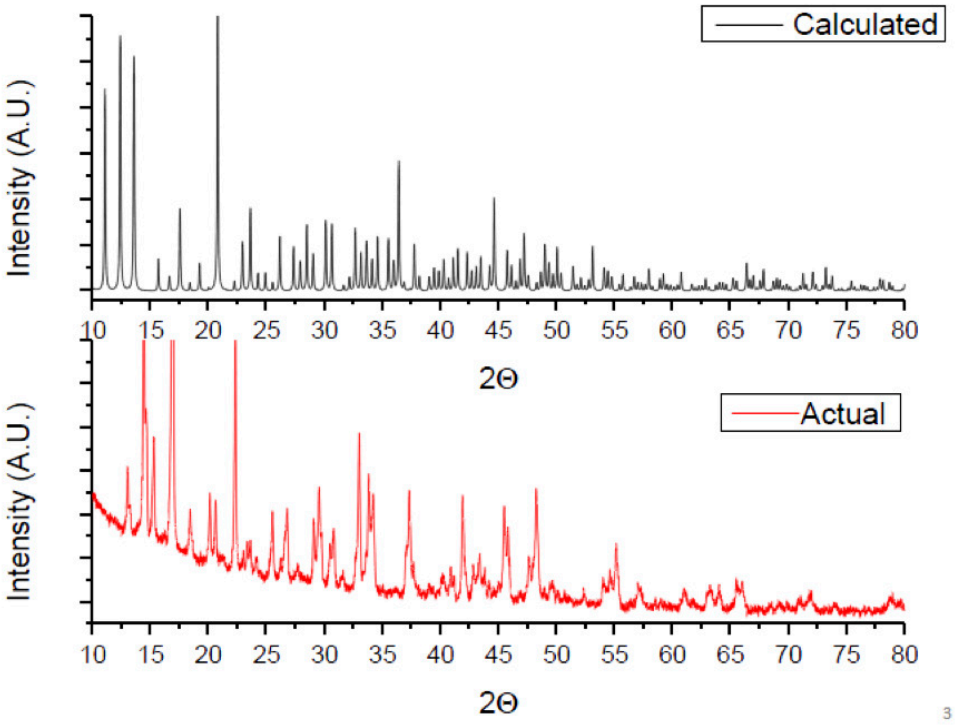

Figure 6.1 Calculated and measured powder X-ray diffraction patterns for $Eu_4[B_{16}O_{26}(OH)_4(H_2O)_3Cl_4]$.

Table 6.1 Crystallographic data for $Sm_4[B_{16}O_{26}(OH)_4(H_2O)_3Cl_4]$ (**SmBOCl**), $Eu_4[B_{16}O_{26}(OH)_4(H_2O)_3Cl_4]$ (**EuBOCl**), $Gd_4[B_{16}O_{26}(OH)_4(H_2O)_3Cl_4]$ (**GdBOCl**), $Pu_4[B_{16}O_{26}(OH)_4(H_2O)_3Cl_4]$ (**PuBOCl**), $Am_4[B_{16}O_{26}(OH)_4(H_2O)_3Cl_4]$ (**AmBOCl**), $Cm_4[B_{16}O_{26}(OH)_4(H_2O)_3Cl_4]$ (**CmBOCl**), and $Cf_4[B_{16}O_{26}(OH)_4(H_2O)_3Cl_4]$ (**CfBOCl**)

Compound	**SmBOCl**	**EuBOCl**	**GdBOCl**	**PuBOCl**	**AmBOCl**	**CmBOCl**	**CfBOCl**
Mass	1456.26	1462.7	1471.76	1822.86	1826.86	1846.86	1848.85
Color and habit	Colorless, Octahedra	Colorless, Octahedra	Colorless, Octahedra	Dark Blue, Octahedra	Pink, Octahedra	Yellow, Octahedra	Light green, Octahedra
Space group	$P2_13$	$P2_13$	$P2_13$	$P2_13$	$P2_13$	$P2_13$	$P2_13$
a (Å)	16.0467(14)	15.9822(4)	15.9934(14)	16.0148(7)	16.0543(8)	15.9799(3)	15.8751(19)
α(deg)	90	90	90	90	90	90	90
V (Å^3)	4132.0(6)	4082.34(18)	4090.9(6)	4107.4(3)	4137.8(4)	4080.58(13)	4000.8(14)
Z	4	4	4	4	4	4	4
T (K)	100(2)	100(2)	100(2)	100(2)	100(2)	100(2)	100(2)
λ(Å)	0.71073	0.71073	0.71073	0.71073	0.71073	0.71073	0.71073
Maximum 2θ(deg.)	27.44	28.35	28.39	27.5	27.46	28.28	27.483
ρcalcd (g cm^{-3})	2.341	2.38	2.39	2.948	2.933	3.006	3.053
μ(Mo $K\alpha$)	59.53	64.17	67.55	66.9	76.85	82.63	87.47
$R(F)$for $F_o^2 > 2\sigma(F_o^2)^a$	0.0398	0.0317	0.0274	0.0388	0.0244	0.0291	0.0614
$Rw(F_o^2)^b$	0.0794	0.0645	0.064	0.0933	0.0715	0.0679	0.1339

$^a R(F) = \Sigma || F_0 | - | F_c || / \Sigma | F_0 |$

$^b R(F_0^2) = [\Sigma w(F_0^2 - F_c^2)^2 / \Sigma w(F_0^4)]^{1/2}$

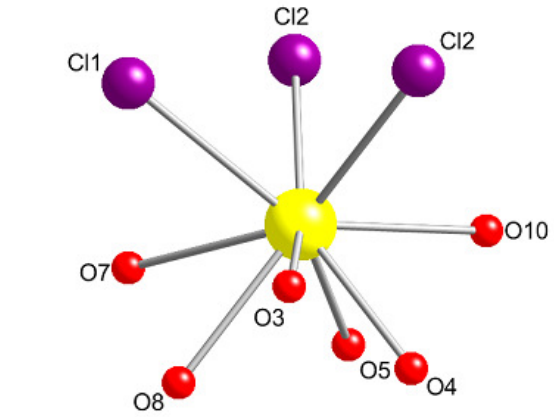

a)

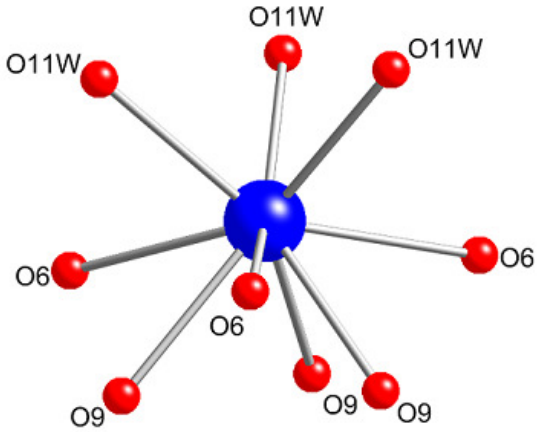

b)

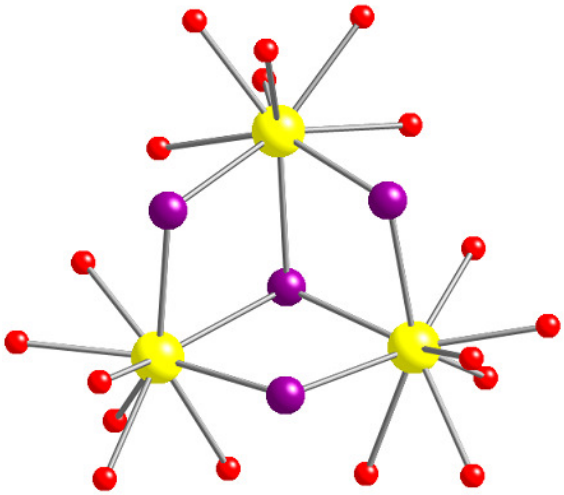

c)

Figure 6.2 Ball and stick models depicting the coordination geometry (tricapped trigonal prism) and connectivity by the bridging chlorine atoms in $M_4[B_{16}O_{26}(OH)_4(H_2O)_3Cl_4]$. The metal centers are represented by the yellow or blue spheres, oxygen atoms by red spheres, and chlorines by purple spheres.

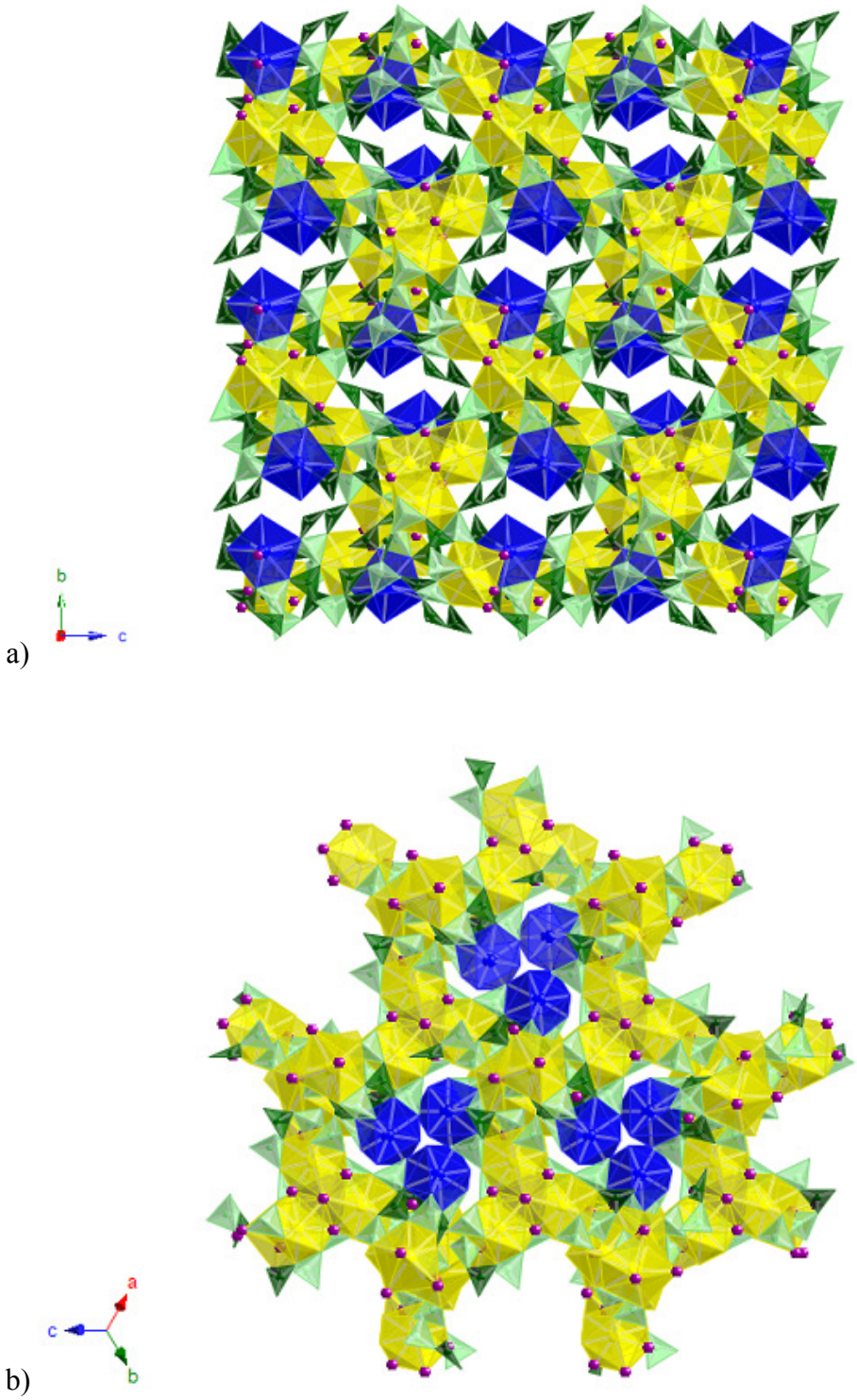

Figure 6.3 Depiction of the a) three-dimensional framework and b) the projection down the [111] axis of $M_4[B_{16}O_{26}(OH)_4(H_2O)_3Cl_4]$. The metal centers are depicted by yellow and blue spheres, chlorine is depicted by purple spheres, BO_4 tetrahedra as light green unit, and BO_3 triangles as dark green units.

Table 6.2 Selected bond distances (Å) for $Sm_4[B_{16}O_{26}(OH)_4(H_2O)_3Cl_4]$ (**SmBOCl**), $Eu_4[B_{16}O_{26}(OH)_4(H_2O)_3Cl_4]$ (**EuBOCl**), and $Gd_4[B_{16}O_{26}(OH)_4(H_2O)_3Cl_4]$ (**GdBOCl**)

Metal Site 1	**Distance (Å)**	**Metal Site 2**	**Distance (Å)**
Sm(1)-Cl(1)	2.870(2)	Sm(2)-O(6)	2.617(7)
Sm(1)-Cl(2)	2.794(2)	Sm(2)-O(9)	2.456(7)
Sm(1)-O(3)	2.555(7)	Sm(2)-O(11w)	2.492(10)
Sm(1)-O(4)	2.428(7)		
Sm(1)-O(5)	2.389(7)		
Sm(1)-O(7)	2.560(7)		
Sm(1)-O(8)	2.452(6)		
Sm(1)-O(10)	2.512(7)		
Gd(1)-Cl(1)	2.8601(12)	Gd(2)-O(6)	2.620(4)
Gd(1)-Cl(2)	2.7692(15)	Gd(2)-O(9)	2.455(4)
Gd(1)-O(3)	2.553(4)	Gd(2)-O(11w)	2.469(6)
Gd(1)-O(4)	2.435(4)		
Gd(1)-O(5)	2.382(4)		
Gd(1)-O(7)	2.499(4)		
Gd(1)-O(8)	2.440(4)		
Gd(1)-O(10)	2.547(4)		
Eu(1)-Cl(1)	2.8572(14)	Eu(2)-O(6)	2.617(7)
Eu(1)-Cl(2)	2.7815(17)	Eu(2)-O(9)	2.456(7)
Eu(1)-O(3)	2.543(5)	Eu(2)-O(11)	2.492(10)
Eu(1)-O(4)	2.428(5)		
Eu(1)-O(5)	2.388(5)		
Eu(1)-O(7)	2.502(5)		
Eu(1)-O(8)	2.438(5)		
Eu(1)-O(10)	2.542(5)		

Table 6.3 Selected bond distances (Å) for $Pu_4[B_{16}O_{26}(OH)_4(H_2O)_3Cl_4]$ (**PuBOCl**), $Am_4[B_{16}O_{26}(OH)_4(H_2O)_3Cl_4]$ (**AmBOCl**), $Cm_4[B_{16}O_{26}(OH)_4(H_2O)_3Cl_4]$ (**CmBOCl**), and $Cf_4[B_{16}O_{26}(OH)_4(H_2O)_3Cl_4]$ (**CfBOCl**)

Metal Site 1	Distance (Å)	Metal Site 2	Distance (Å)
Pu(1)-Cl(1)	2.8622(4)	Pu(2)-O(6)	2.6569(13)
Pu(1)-Cl(2)	2.7801(4)	Pu(2)-O(9)	2.6014(12)
Pu(1)-O(3)	2.5558(13)	Pu(2)-O(11w)	2.588(3)
Pu(1)-O(4)	2.5151(11)		
Pu(1)-O(5)	2.4420(10)		
Pu(1)-O(7)	2.5881(11)		
Pu(1)-O(8)	2.5217(10)		
Pu(1)-O(10)	2.5747(12)		
Cm(1)-Cl(1)	2.8558(6)	Cm(2)-O(6)	2.6627(14)
Cm(1)-Cl(2)	2.7373(6)	Cm(2)-O(9)	2.5673(14)
Cm(1)-O(3)	2.5762(4)	Cm(2)-O(11w)	2.61273(14)
Cm(1)-O(4)	2.4887(4)		
Cm(1)-O(5)	2.4349(5)		
Cm(1)-O(7)	2.5614(4)		
Cm(1)-O(8)	2.4758(7)		
Cm(1)-O(10)	2.5469(5)		
Am(1)-Cl(1)	2.86425(15)	Am(2)-O(6)	2.67357(15)
Am(1)-Cl(2)	2.76286(13)	Am(2)-O(9)	2.58134(14)
Am(1)-O(3)	2.56955(12)	Am(2)-O(11w)	2.60015(13)
Am(1)-O(4)	2.48804(13)		
Am(1)-O(5)	2.42445(13)		
Am(1)-O(7)	2.57630(13)		
Am(1)-O(8)	2.49269(13)		
Am(1)-O(10)	2.53742(13)		
Cf(1)-Cl(1)	2.827(7)	Cf(2)-O(6)	2.63(2)
Cf(1)-Cl(2)	2.697(8)	Cf(2)-O(9)	2.53(2)
Cf(1)-O(3)	2.62(2)	Cf(2)-O(11w)	2.54(4)
Cf(1)-O(4)	2.459(19)		
Cf(1)-O(5)	2.44(2)		
Cf(1)-O(7)	2.57(2)		
Cf(1)-O(8)	2.47(2)		
Cf(1)-O(10)	2.56(3)		

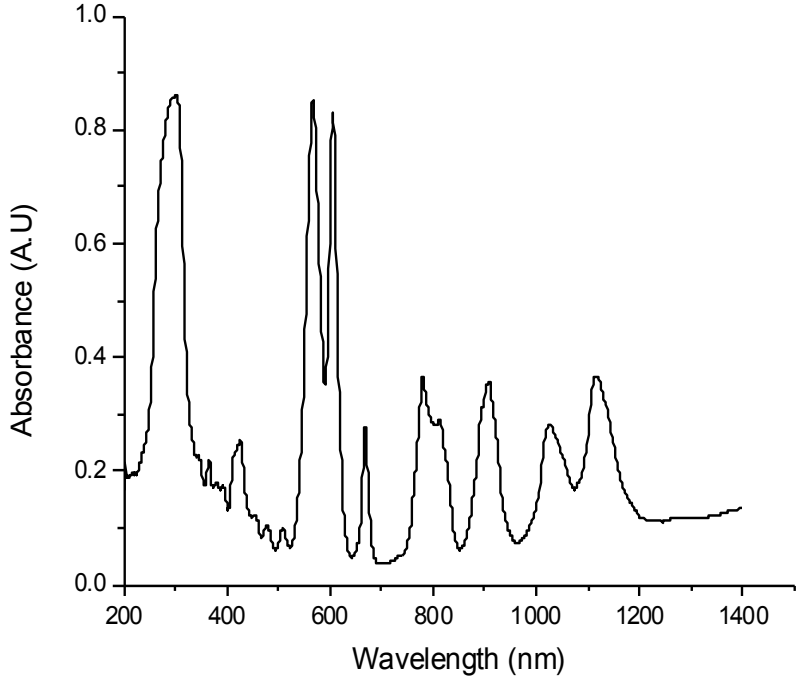

Figure 6.4 Absorption spectrum of $Pu_4[B_{16}O_{26}(OH)_4(H_2O)_3Cl_4]$ showing *f-f* transitions that are characteristic for Pu(III).

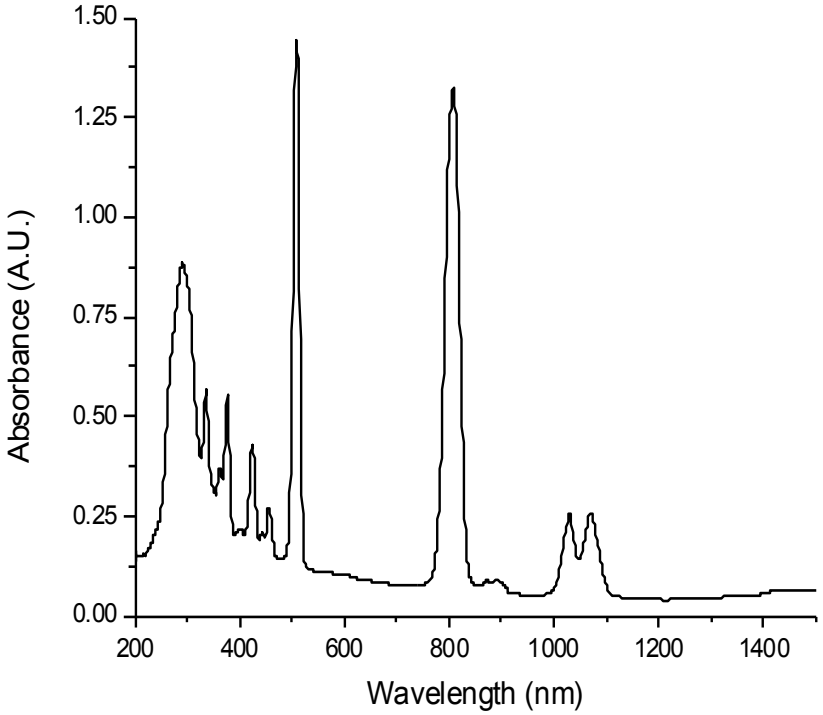

Figure 6.5 Absorption spectrum of $Am_4[B_{16}O_{26}(OH)_4(H_2O)_3Cl_4]$ showing *f-f* transitions that are characteristic for Am(III).

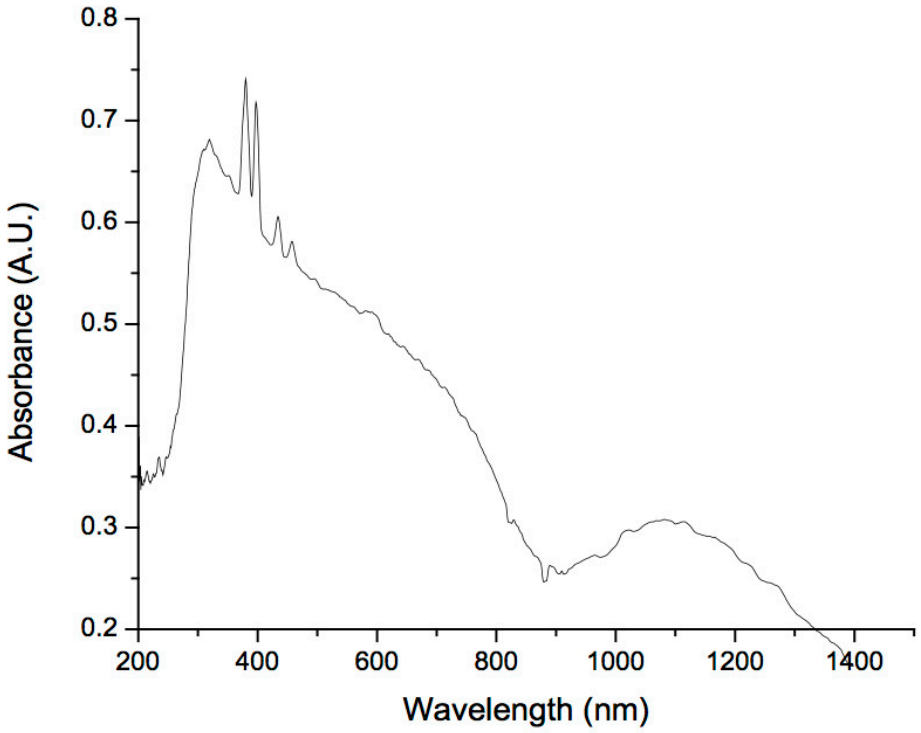

Figure 6.6: Absorption spectrum of $Cm_4[B_{16}O_{26}(OH)_4(H_2O)_3Cl_4]$ showing *f-f* transitions that are characteristic for Cm(III).

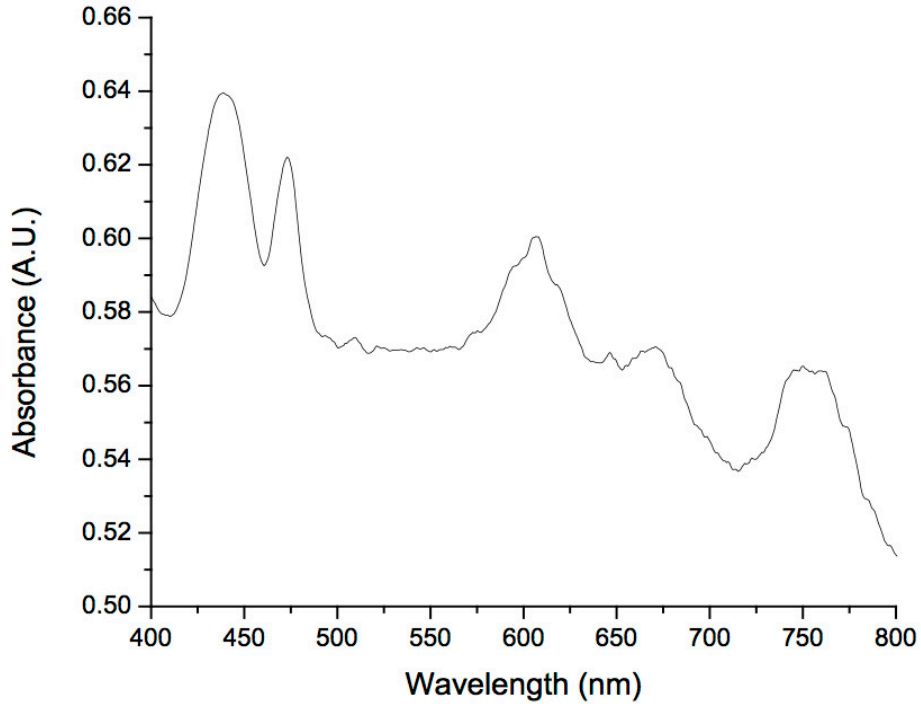

Figure 6.7 Absorption spectrum of $Cf_4[B_{16}O_{26}(OH)_4(H_2O)_3Cl_4]$ showing *f-f* transitions that are characteristic for Cf(III).

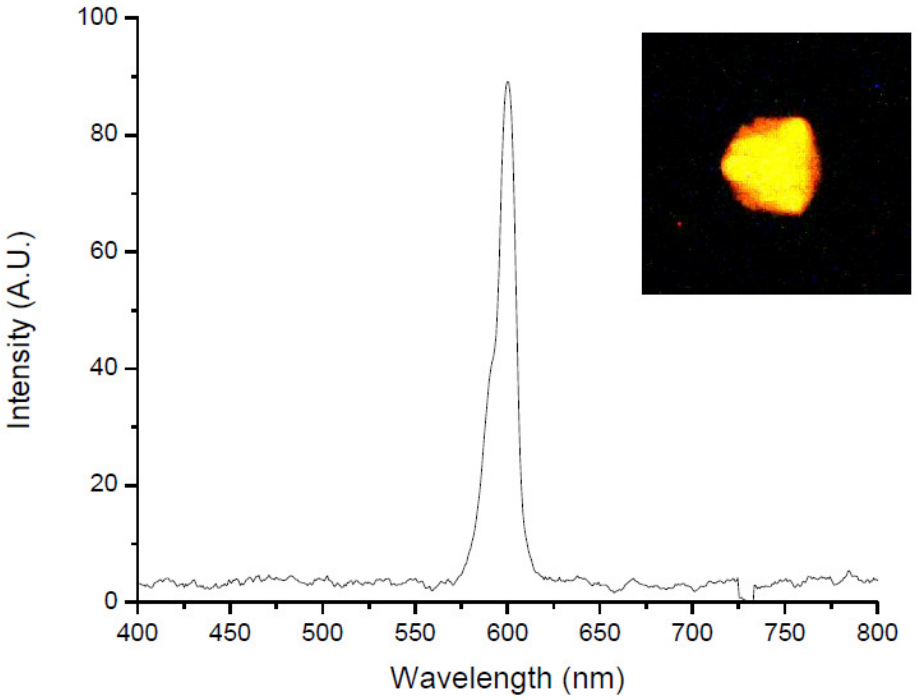

Figure 6.8 Fluorescence spectrum of $Cm_4[B_{16}O_{26}(OH)_4(H_2O)_3Cl_4]$ showing the emission near 595 nm, giving off yellow-orange light (insert) upon excitation of 420 nm light. The fluorescence of Cm(III) is a result of the relaxation from the $^6D_{7/2}$ excited state to the $^8S_{7/2}$ ground state.

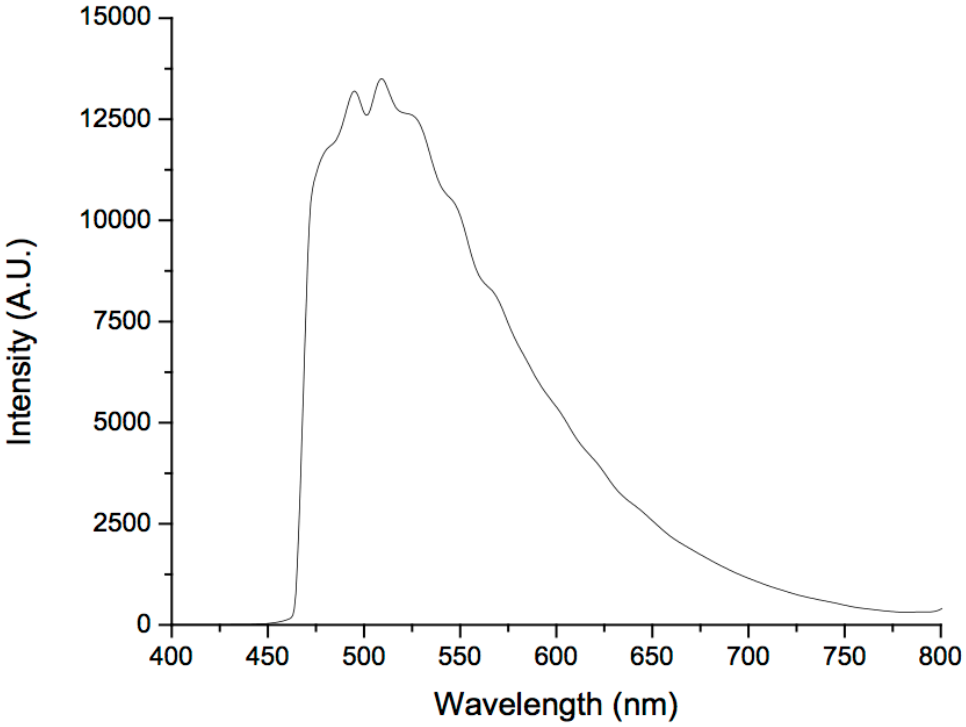

Figure 6.9 Fluorescence spectrum of $Cf_4[B_{16}O_{26}(OH)_4(H_2O)_3Cl_4]$ showing the emission near 525 nm and giving off green light upon excitation of 420 nm light. The two resolved peaks near 500 and 525 nm are most likely due to the two different Cf(III) sites present in this compound.

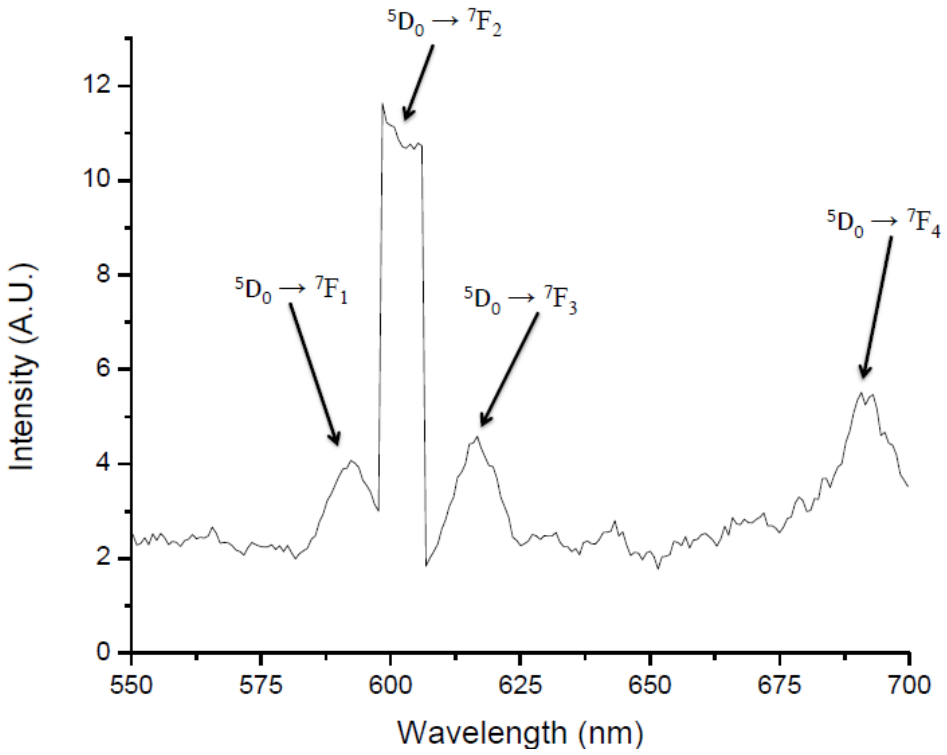

Figure 6.10 Fluorescence spectrum of $Eu_4[B_{16}O_{26}(OH)_4(H_2O)_3Cl_4]$ showing the emission between 600-615 nm and giving off red light upon excitation of 420 nm light. The fluorescence of Eu(III) is a result of the relaxation from the $^5D_0$ excited state to the $^7F_2$ manifold of the $^7F_0$ ground state.

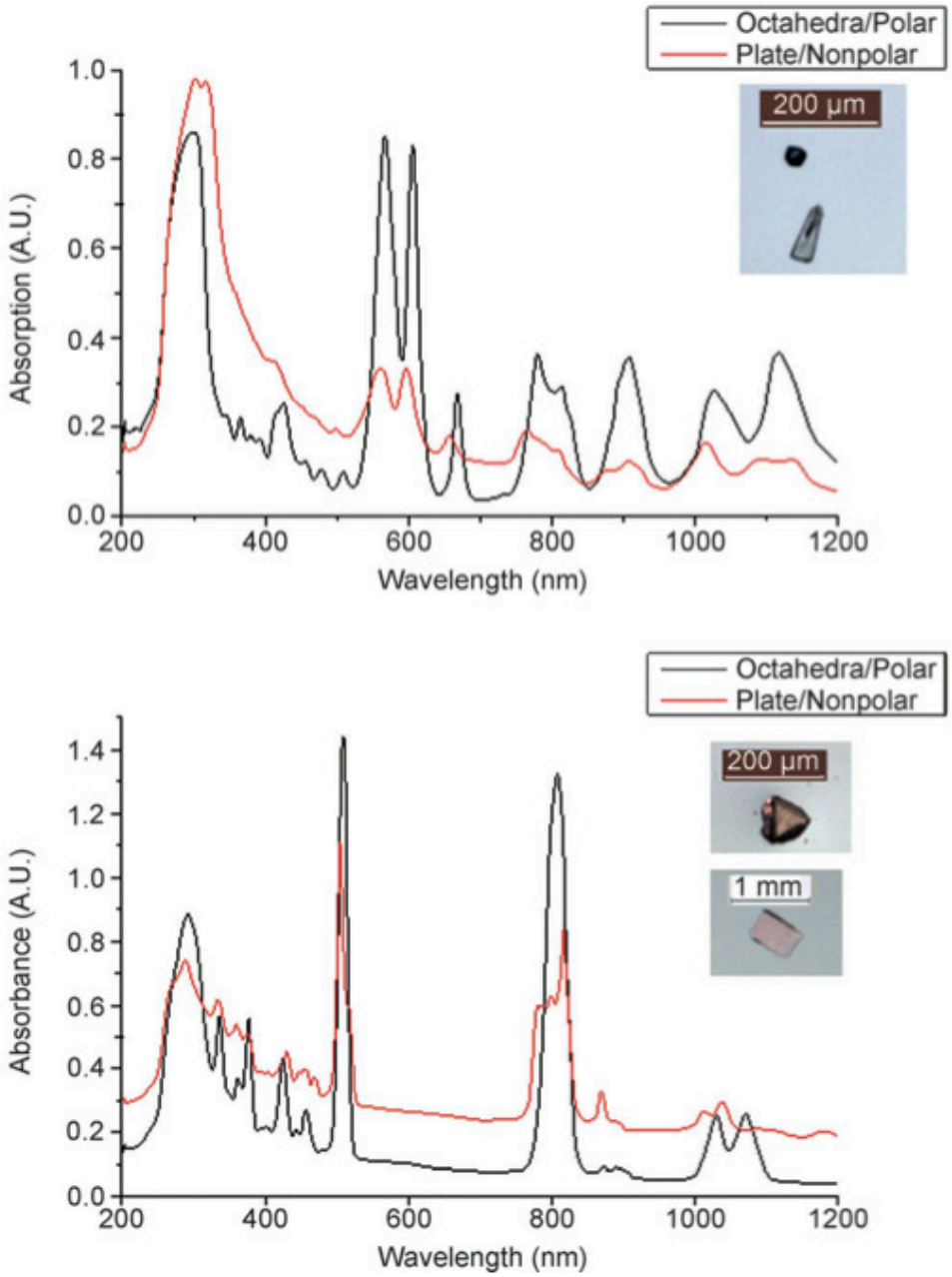

Figure 6.11 Absorption spectra taken at room temperature showing the characteristic Laporte forbidden *f–f* transitions observed for $Pu_4[B_{16}O_{26}(OH)_4(H_2O)_3Cl_4]$ (top black), $Pu_2[B_{13}O_{19}(OH)_5Cl_2(H_2O)_3]$ (top red), $Am_4[B_{16}O_{26}(OH)_4(H_2O)_3Cl_4]$ (bottom black), and $Am[B_9O_{13}(OH)_4]\cdot H_2O$ (bottom red). The photo inserts of each Figure have the polar crystals on top, and the nonpolar crystals on bottom.

CHAPTER SEVEN

CONCLUSION

This work has demonstrated and further developed of the idea that the polarizable oxoanions can be used to probe the changes in bonding when comparing lanthanide and actinide compounds. By utilizing both borate and plumbite oxoanions, which possess well-documented hyperpolarizability and polarizability, a variety of structures were synthesized. This was achieved by development of the supercritical water technique to explore phase spaces beyond that of the boric acid flux, and expansion of the mild hydrothermal technique.

Through the use of supercritical water as a synthetic media two new uranium borates were synthesized, connecting low temperature flux grown uranium borates with the high temperature uranium borates synthesized by Gasperin. These two new borates sharply diverge from those grown by flux, exhibiting a complex uranyl network instead of a borate network. Additionally the borate anions incorporated in the structures are exclusively trigonal and occur only as the BO_3 or B_2O_5 units. $K_{13}[(UO_2)_{19}(UO_4)(B_2O_5)_2(BO_3)_6(OH)_2O_5]\cdot H_2O$ is a mixed valent structure providing a link to the mixed valent structures observed for neptunium.

The family of hexanuclear and pentanuclear lanthanide lead clusters develop the chemistry and foundation of the plumbite and *f*-element chemistry. These clusters, add to both the sparce literature documenting lanthanide lead structures and expand the understanding of the hexanuclear lanthanide clusters. These clusters demostrate the common electronic, photoluminescent, and magnetic properties associated with the lanthanides. Owing to the extremely high hyperpolarizability and proposed polarizability of the plumbite anion, changes in the electronics and structure of actinide complex synthesized under similar conditions are expected.

Two structural studies were conducted with californium through reactions in a boric acid flux, which complete two structural families that extend to californium. In the synthesis of $Cf[B_6O_8(OH)_5]$, californium differed from all previous observations of coordination environment, borate network, and bonding. However, when comparing this behavoir to the $M_4[B_{16}O_{26}(OH)_4\cdot(H_2O)_3Cl_4]$ family, for which californium is a member, it appears to act in a similar manner to both its lanthanide and actinide congeners. This furthers serves to demonstrate

that while the behavior of californium and other trivalent actinides is hard to predict, careful choice of hyperpolarizable ligands can give rise to covalent interactions.

APPENDIX A

SUPERCRITICAL WATER SETUP

Figure A.1 The autoclave in its three parts: vessel, plunger, and cap.

Figure A.2 Assembled the cap drives the plunger into the vessel creating a metal-metal seal. This specific type of sealing mechanism in known as a Tuttle Cold seal.

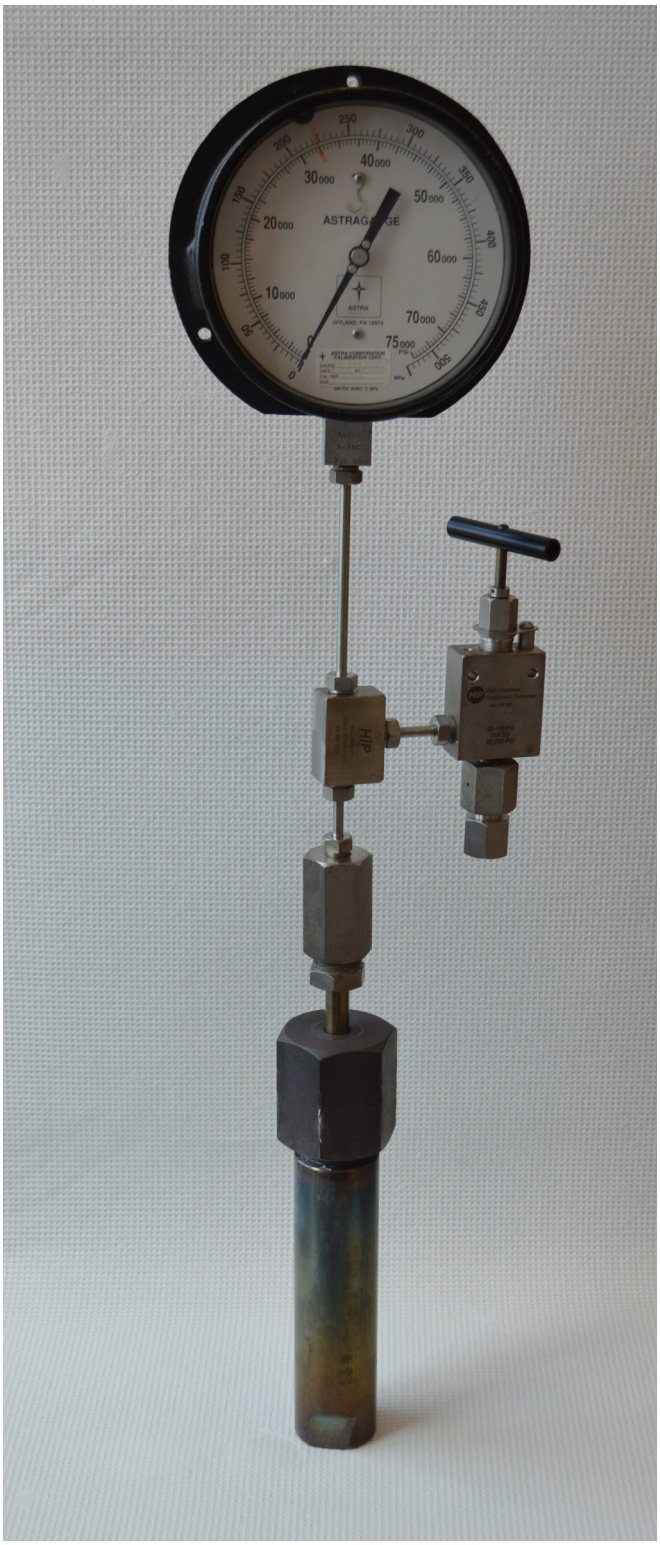

Figure A.3 A pressure apparatus is attached to monitor pressure. (In this picture the metal is more a brown color due to repeated heat-treating.)

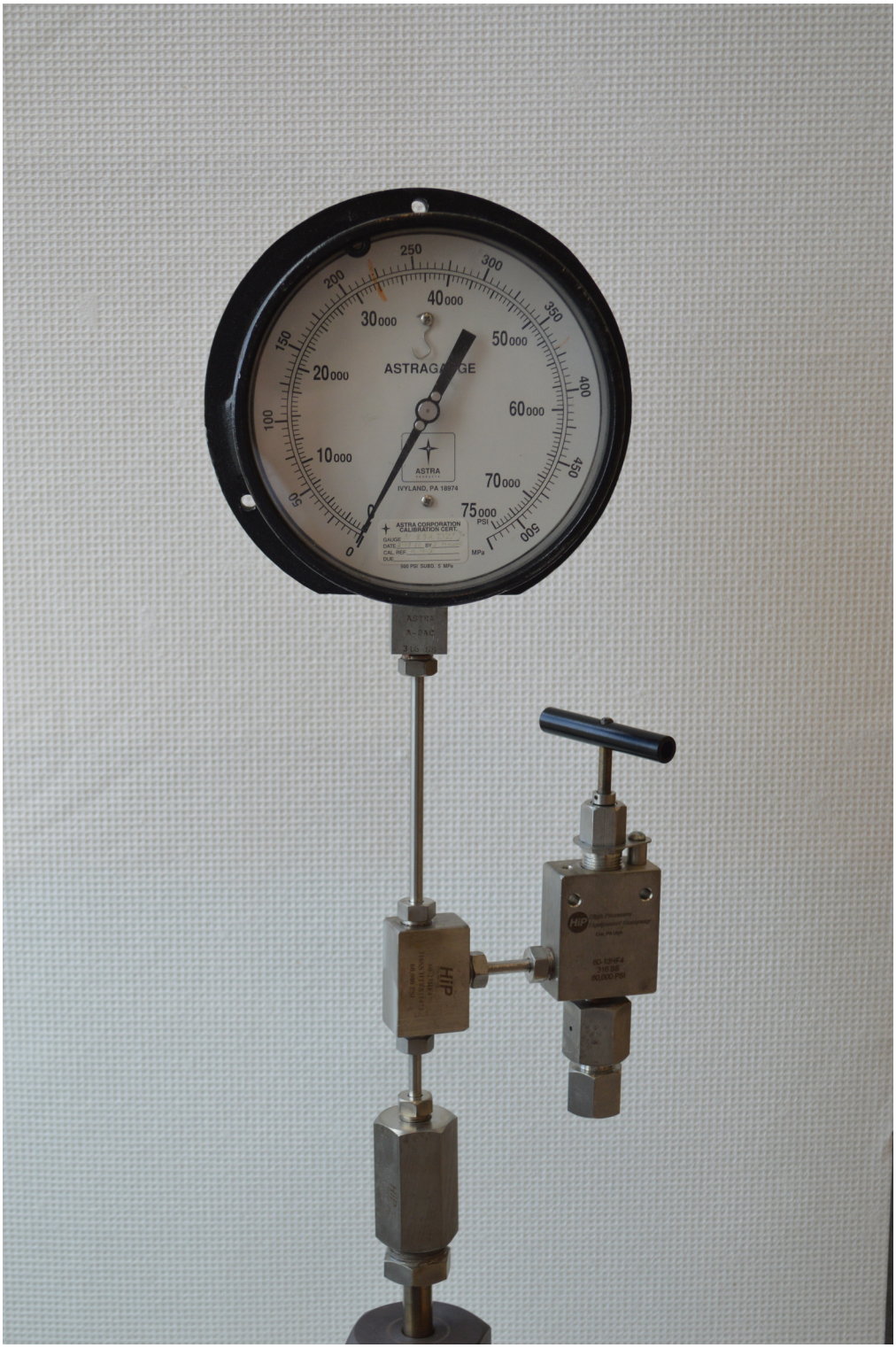

Figure A.4 The pressure apparatus consists of a manual release valve, a blast seal for over pressure, and a gauge for reading the pressure.

Figure A.5 The system is heated by attaching a band heater and thermocouple.

Figure A.6 Stable heating is achieved by placing the system in a pit insulated by vermiculite.

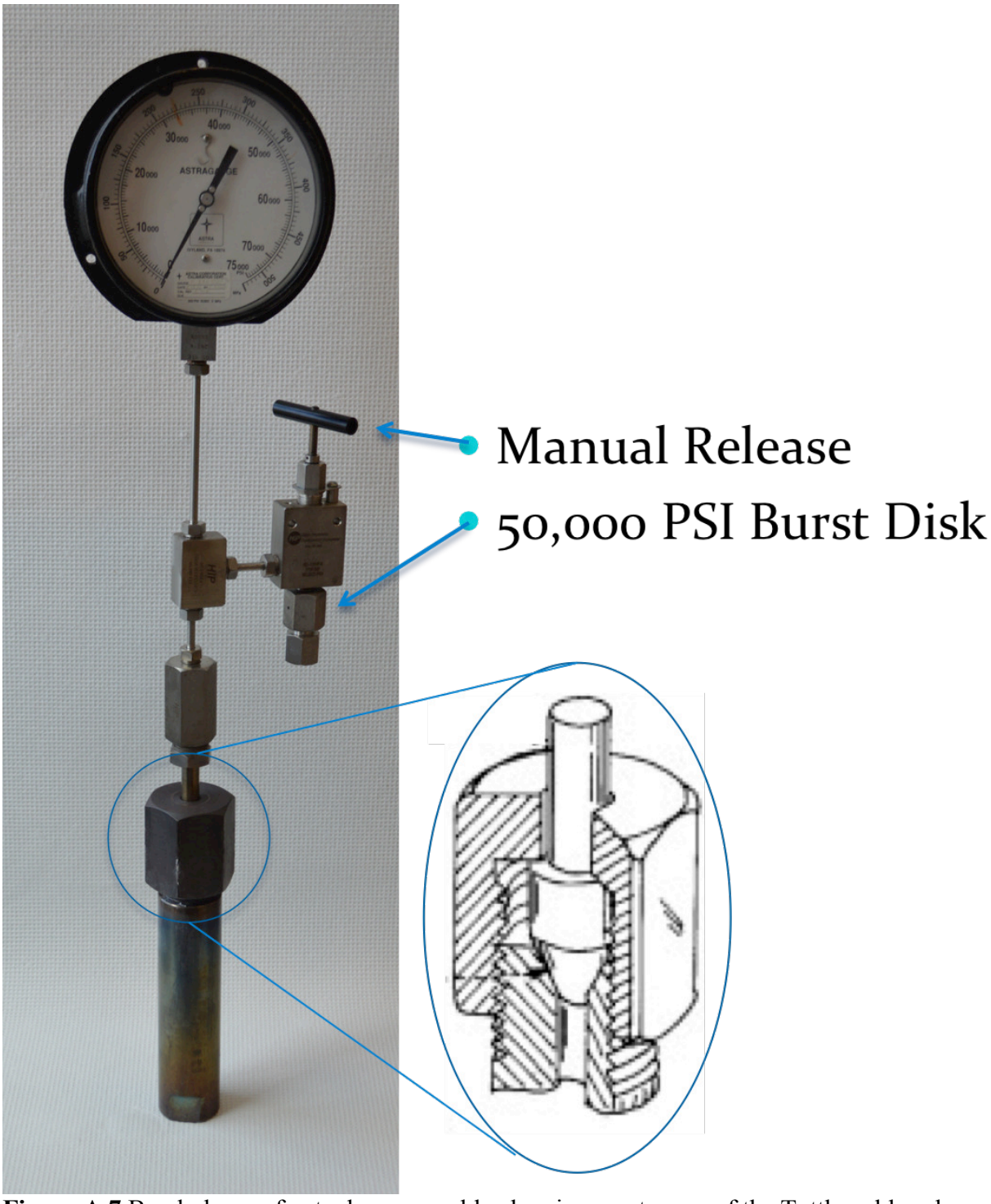

Figure A.7 Break down of autoclave assembly showing a cut away of the Tuttle cold seal mechanism.

Figure A.8 Silver floating liners used for basic conditions. From top to bottom: fine silver tubing, crimpled and welded, loaded and sealed, and crushed after reaction.

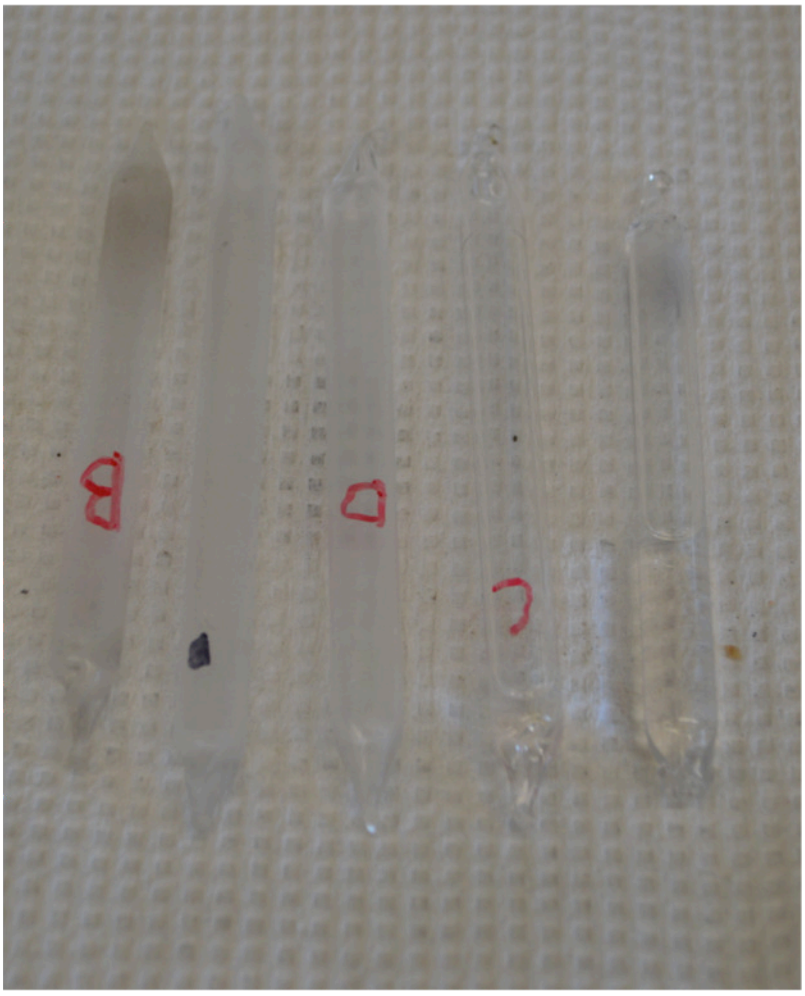

Figure A.9 Quartz floating liners used for acidic or oxidizing conditions. On the right, sealed quartz tubing transparent with mineralizer before reaction. On the left, tube after reaction hazy from crystal formation.

Autoclave Cooling

Turn off and let stand in furnace (approximately 8 hours till cool), or turn off, remove autoclave, and place under a flow of house air on high (approximately 2 hours till cool

Autoclave Opening

Place in the vice, with the base being held in the vice pads. Relieve any residual pressure by opening the manual release. Use pipe wrench with “cheater stick” (use place hands at the end of the pipe for maximum torque) to apply controlled pressure till the cap rotates. You may need to hold the step down connector to keep the autoclave upright. DO NOT power down on the lever, something will snap, fly off, impale someone, and be bad news.

After seal has been broken the pipe wrench can be discarded and the cap unscrewed using ones hands. Be careful of potential metal splinters on the corners of the cap. Once the cap has been removed. Pour the contents into a beaker. Ensure all the silver tubes look mostly flattened. If any completely retain their cylindrical shape the weld failed, and the water and autoclave are probably contaminated.

Autoclave Cleaning

The threads of the autoclave should be cleaned in between each cycle. Turn the bench grinder on and allow it to reach maximum speed. A mask should be worn for the grinding. Press the threads up to the wire brush side. If to much pressure is applied, the brush will slow down. This can be felt and indicates that slightly less pressure should be used. The cleaned surface should be shinny like the rest of autoclave.

In the advent of a weld failure the inside of the autoclave can be cleaned. Wash 3x with DI water. Scrub with Alconox and a test tube brush. 3x DI water rinse and it's good to go.

Autoclave Loading

Secure autoclave base in an up right position in the vice. Place two silver tube so the welds are parallel to each other and drop into autoclave. The low numbers go in first. Measure out approximately 19.5 mL of DI water and pour into the chamber or fill the chamber to the top. Coat the threads with a layer of copper grease. Screw the cap on till it is fully tightened. Use the pipe wrench and cheater stick (FROM 2' out, NOT THE EDGE!) to fully tighten the cap.

Place in tube furnace, check to make turn the manual pressure release is closed. Flip the switch. Check in 1.5-3 hours to ensure pressure has been generated and held. If pressure is not established after 4 hours or pressure is lost during a reaction, turn it off, wait for it to cool, and figure out what went wrong.

APPENDIX B

SUPPLEMENTAL INFORMATION FOR CHAPTER 3

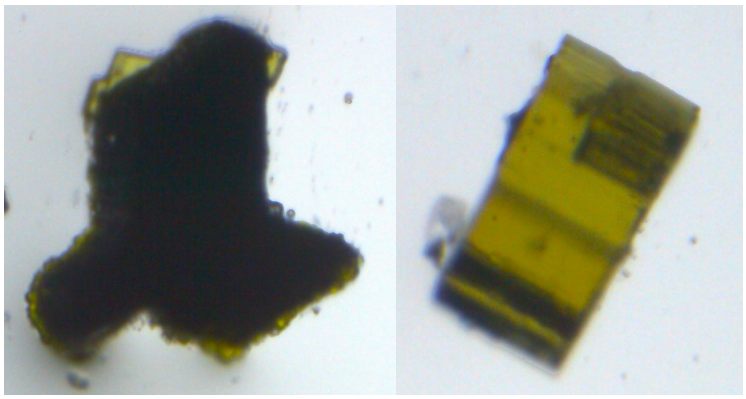

Figure B.1 left) View through the top of $K_{13}[(UO_2)_{19}(UO_4)(B_2O_5)_2(BO_3)_6(OH)_2O_5]\cdot H_2O$ (**2-SCWUB**). right) View through the side $K_{13}[(UO_2)_{19}(UO_4)(B_2O_5)_2(BO_3)_6(OH)_2O_5]\cdot H_2O$ (**2-SCWUB**).

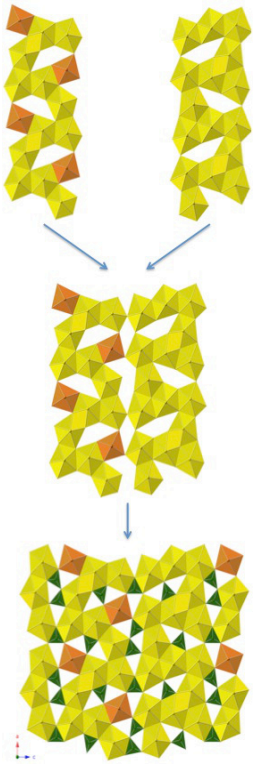

Figure B.2 Linking of edge sharing uranium chains via corner sharing and borate triangles to form a complex sheet topology.

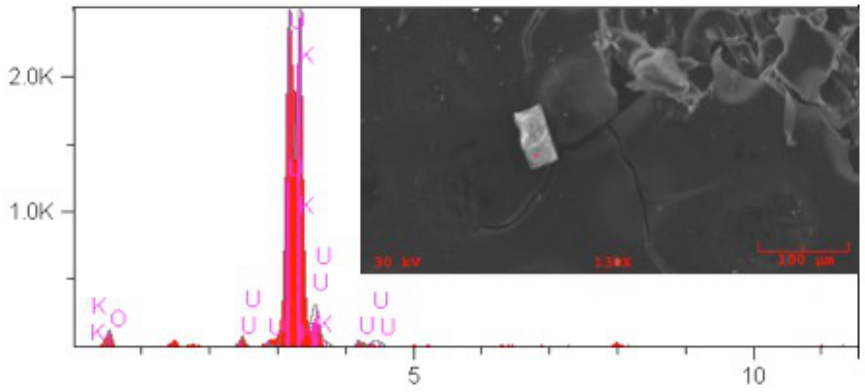

Elt.	Line	Intensity (c/s)	Error 2-sig	Conc	Units	
O	Ka	38.05	2.252	8.020	wt.%	
K	Ka	421.76	7.498	8.731	wt.%	
U	Ma	1,027.56	11.704	83.249	wt.%	
				100.000	wt.%	Total

Figure B.3 SEM images and EDS spectra of $K_{10}[(UO_2)_{16}(B_2O_5)_2(BO_3)_6O_8]\cdot 7H_2O$ (**1-SCWUB**). The presence of K and U were confirmed, however only semi-quantitative values could achieved as the Kα of potassium and the Mα of uranium overlap.

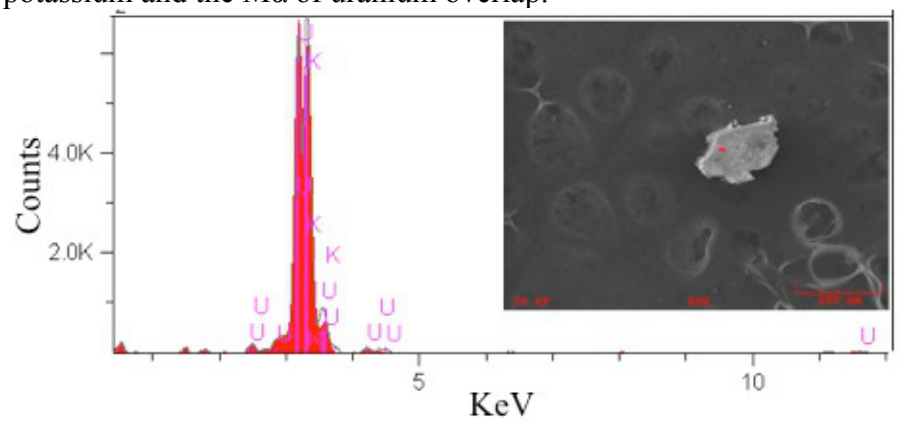

Elt.	Line	Intensity (c/s)	Error 2-sig	Atomic %	
K	Ka	1,249.25	12.905	43.139	
U	Ma	2,563.88	18.488	56.861	
				100.000	Total

Figure B.4 SEM images and EDS spectra of $K_{13}[(UO_2)_{19}(UO_4)(B_2O_5)_2(BO_3)_6(OH)_2O_5]\cdot H_2O$ (**2-SCWUB**). The presence of K and U were confirmed, however only semi-quantitative values could achieved as the Kα of potassium and the Mα of uranium overlap.

APPENDIX C

SUPPLEMENTAL INFORMATION FOR CHAPTER 4

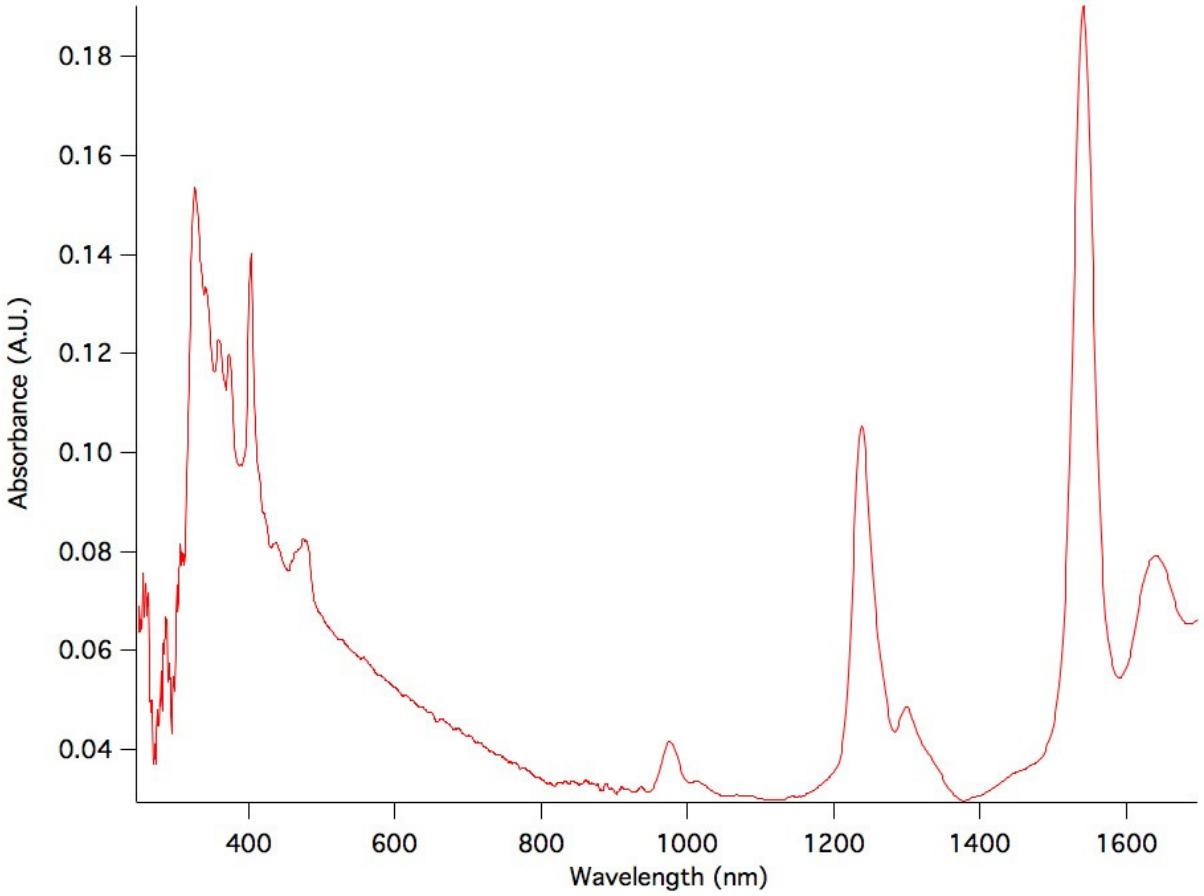

Figure C.1 UV-Vis-NIR absorbance spectrum of $[Sm_6Pb_{18}O_2(OH)_{38}][ClO_4]_{12}\cdot 8\ H_2O$ displaying characteristic sharp *f-f* transitions.

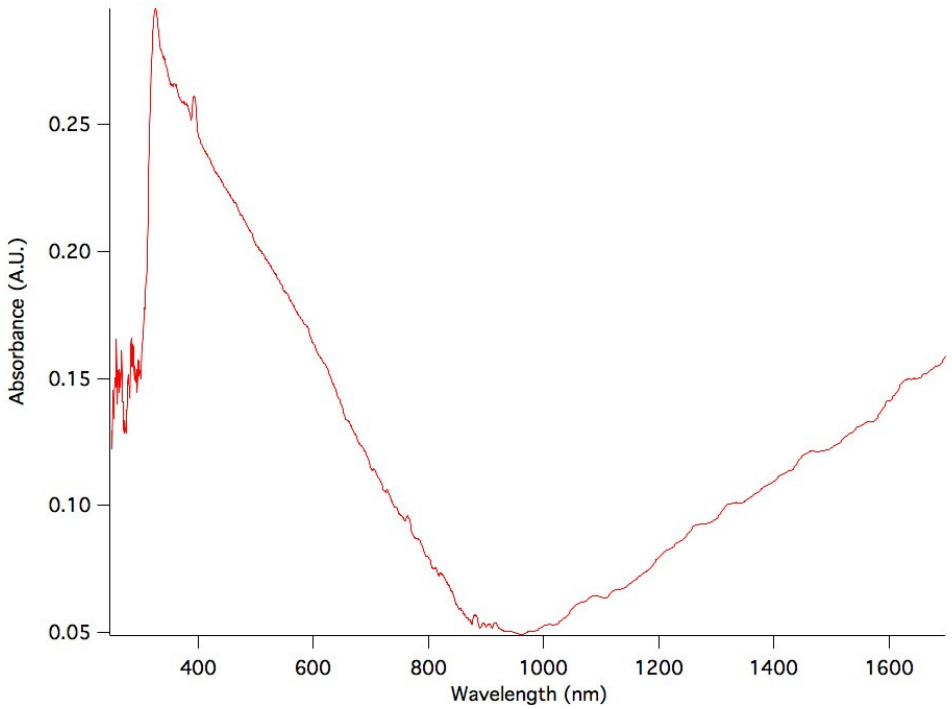

Figure C.2 UV-Vis-NIR absorbance spectrum of $[Eu_6Pb_{18}O_2(OH)_{38}][ClO_4]_{12}\cdot 8\ H_2O$ displaying characteristic sharp *f-f* transitions.

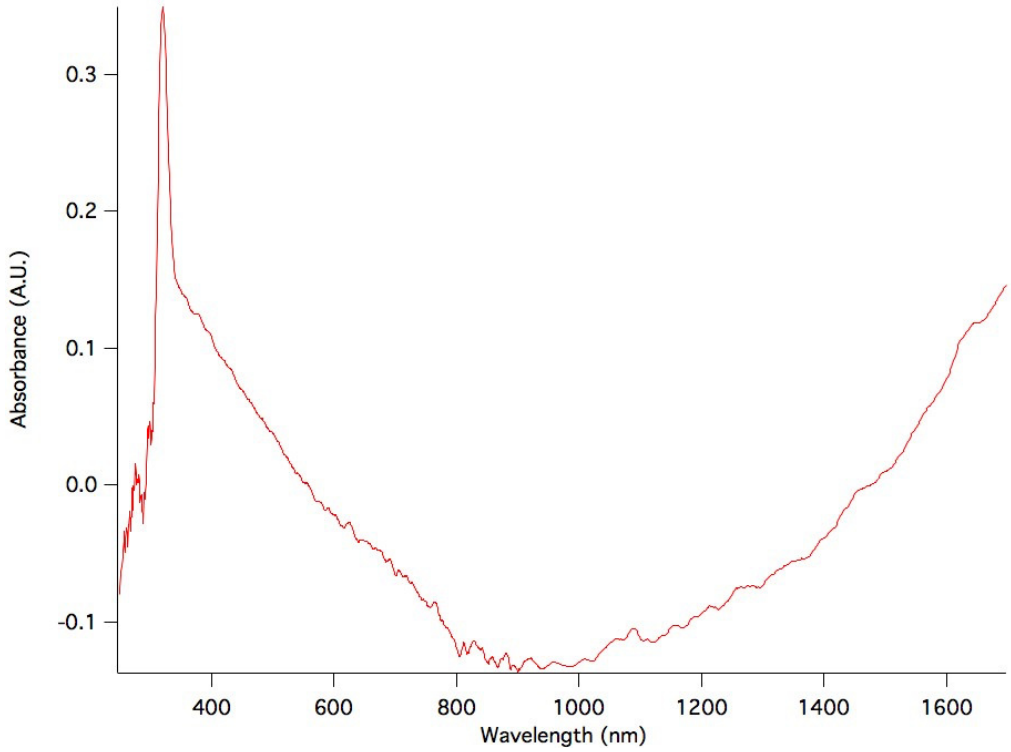

Figure C.3 UV-Vis-NIR absorbance spectrum of $[Gd_6Pb_{18}O_2(OH)_{38}][ClO_4]_{12}\cdot 8\ H_2O$ displaying characteristic sharp *f-f* transitions.

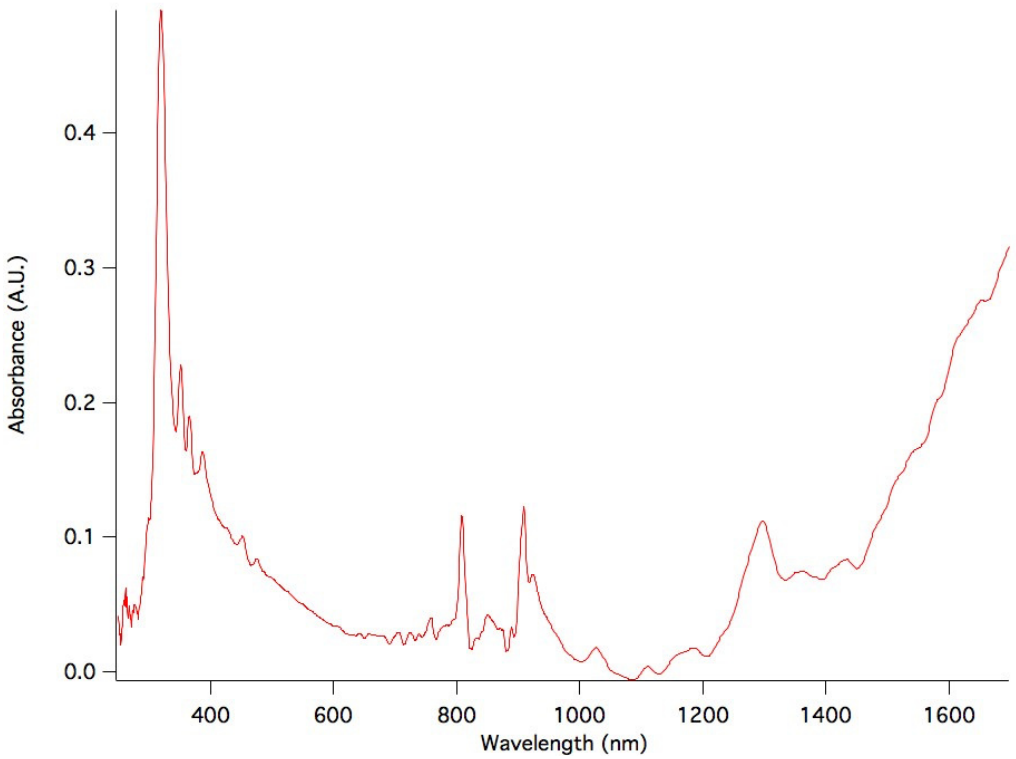

Figure C.4 UV-Vis-NIR absorbance spectrum of $[Dy_6Pb_{18}O_2(OH)_{38}][ClO_4]_{12}\cdot 8\ H_2O$ displaying characteristic sharp *f-f* transitions.

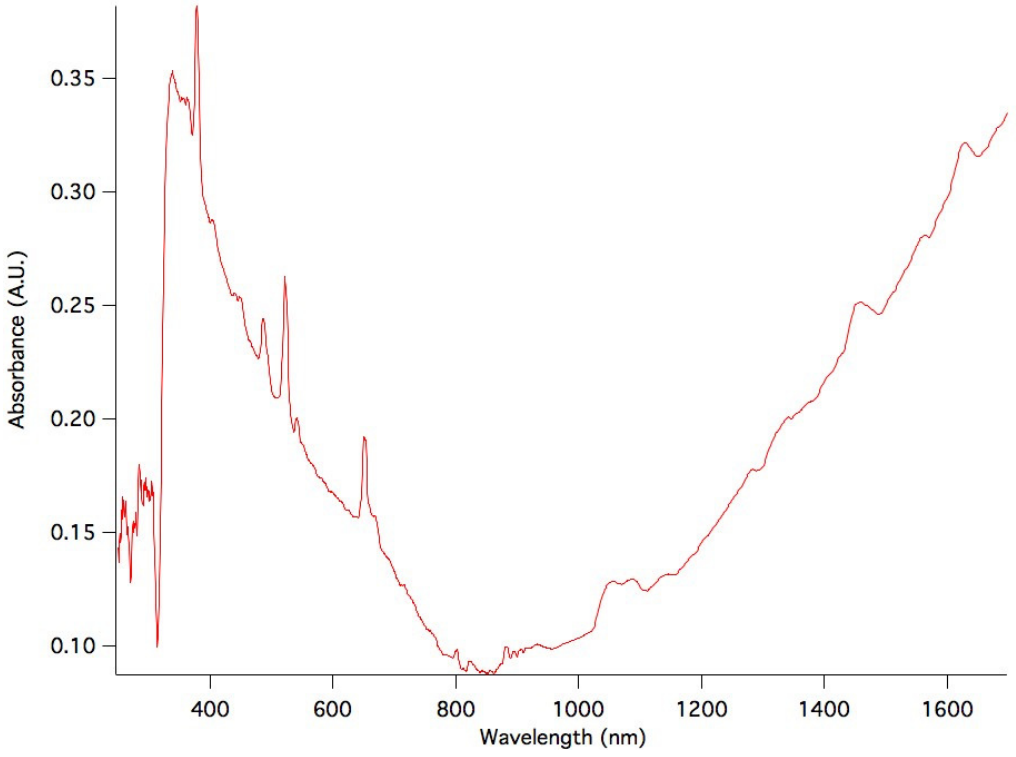

Figure C.5 UV-Vis-NIR absorbance spectrum of $[Er_6Pb_{18}O_2(OH)_{38}][ClO_4]_{12}\cdot 8\ H_2O$ displaying characteristic sharp *f-f* transitions.

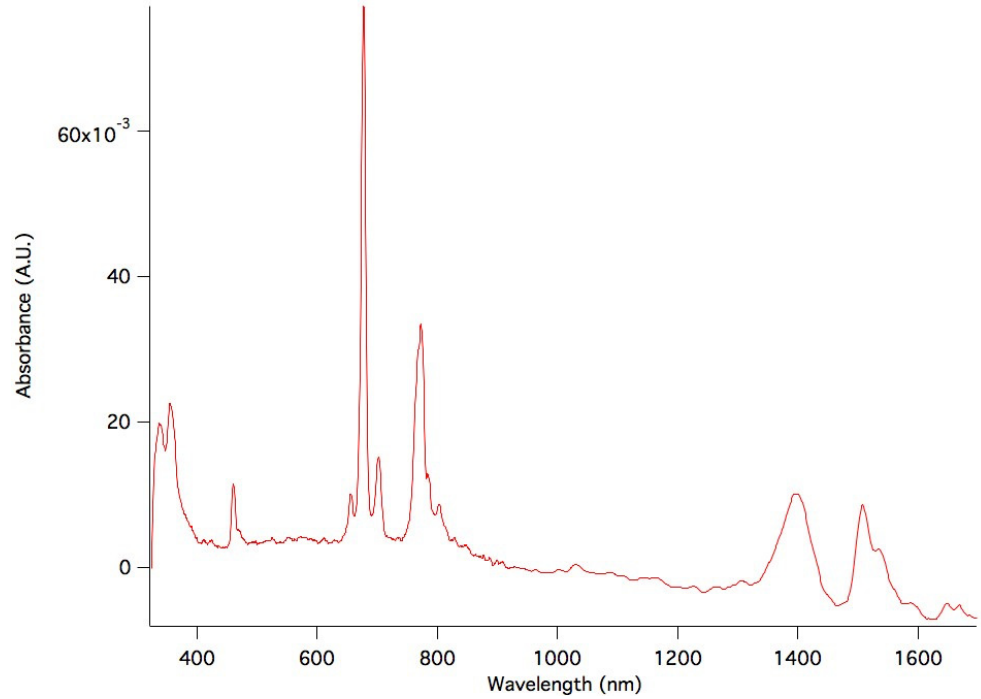

Figure C.6 UV-Vis-NIR absorbance spectrum of $[Tm_5Pb_{17}(OH)_{36}][ClO_4]_{13}\cdot nH_2O$ displaying characteristic sharp *f-f* transitions.

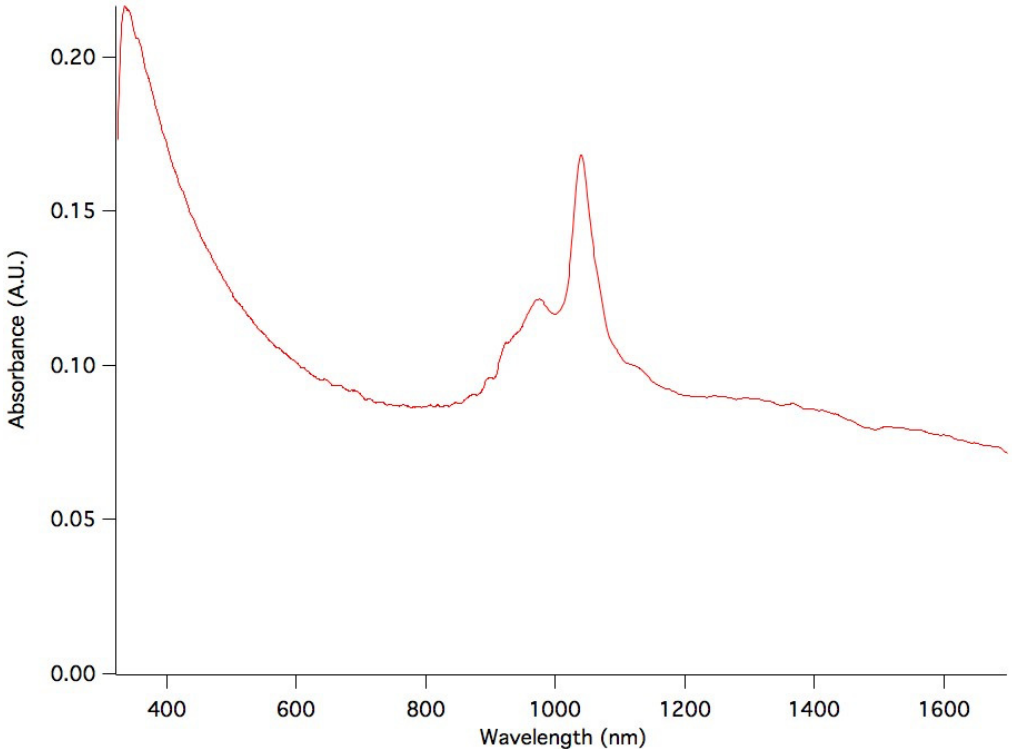

Figure C.7 UV-Vis-NIR absorbance spectrum of $[Yb_5Pb_{17}(OH)_{36}][ClO_4]_{13}\cdot nH_2O$ displaying characteristic sharp *f-f* transitions.

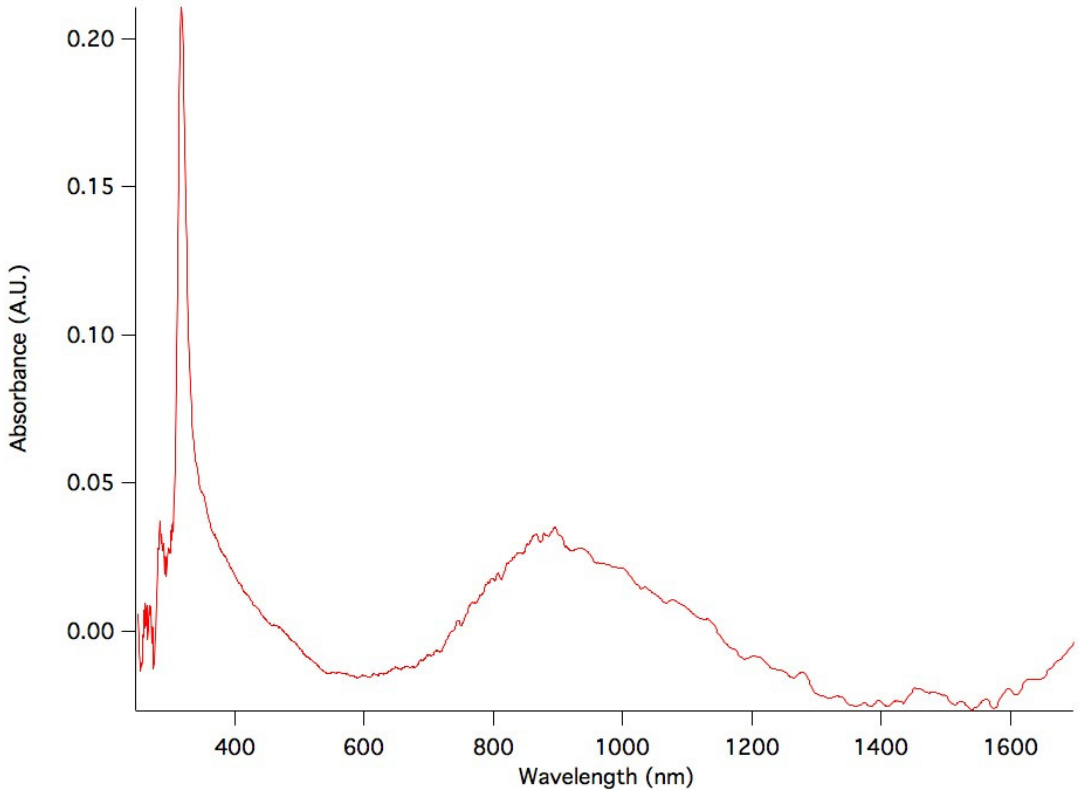

Figure C.8 UV-Vis-NIR absorbance spectrum of $[Lu_5Pb_{17}(OH)_{36}][ClO_4]_{13}\cdot nH_2O$ displaying characteristic sharp *f-f* transitions.

APPENDIX D

CALIFORNIUM BORATE THEORETICAL CALCUATIONS

Theoretical Calculations Methodology

Although the positions of the californium, oxygen, and boron atoms of the cluster were taken from the crystallographic structure, the position of the hydrogen atoms (initially present in the crystallographic structure or added to 'neutralize' the cluster) were optimized with the Perdew–Burke–Ernzerhof (PBE) functional using the TURBOMOLE program package.[154] During this optimization, a C_2 symmetry point group was imposed. The C_2 symmetry arises from the first, second, and third coordination spheres, and hence the imposed symmetry constraint only affects the added protons. All-electron def-TZVP basis sets[155] were used for all the atoms, except the californium atom, which was treated using a 60-electron core quasi-relativistic pseudopotential.[156] A sextet spin state was considered for the optimization of the H atoms. A single-point unrestricted DFT calculation was then performed at this geometry with the PBE0 functional.[157] Test calculations showed that the lowest-energy quartet and doublet spin configurations lie about 30 and 50 kcal mol[158] above the lowest sextet spin state, respectively, and thus only the electronic structure of the ground sextet state is considered in the subsequent population analysis. Restricted open-shell Kohn–Sham DFT single-point calculations were performed with all electron def-TZVP basis sets[155] on hydrogen, boron, and oxygen atoms and the Stuttgart ECP60MWB contracted pseudopotential basis set[156,159] on californium, with both the PBE and PBE0 functionals, using the Gaussian 09 program package.

Mulliken charge and spin populations were computed, and for the B3LYP and PW91 functionals NBO populations were also calculated.[160] An ELF analysis was performed.[154,155] The ELF and electron-density values were computed on a grid with the DGrid program, version 4.6. The topological analysis of the ELF allows the nature of chemical bonds to be discussed.[161] The number of bonding electrons for each Cf–O pair is presented in **Table D.2**. Calculations based on multiconfigurational wavefunction were performed using the CASSCF method with the Molcas program.[162,163] The minimal ANO-DK3 basis set was used for all atoms.[164] The Douglass–Kroll–Hess Hamiltonian was used to account explicitly for scalar relativistic effects.[165,166]

Theoretical Results and Discussion

Prior electronic structure calculations on Pu(III), Am(III) and Cm(III) borates revealed overlap between the 6p and 6d orbitals of Pu(III), Am(III) and Cm(III) with the 2p orbitals of the coordinated borate oxygen atoms.[42] The overlap only occurs at the base sites of the metal coordination environments and is exclusively to oxygen atoms of BO_4 units, not those of BO_3. All sites around the Cf(III) center in $Cf[B_6O_8(OH)_5]$ are occupied by either BO_4, or at two sites, by both BO_3 and BO_4 via μ_3-oxygen atoms. Given the very large charge density of the $[BO_4]$ anions, the coordination environment provides considerable electron density to the Cf(III) center and creates electronic behavior that has not been observed before for Cf(III) and is quite unusual for *f*-elements in general.

To better understand the bonding, quantum chemical calculations were performed using density functional theory (DFT) on a finite cluster, with the PBE,[167] PBE0,[158] B3LYP, and PW91 exchange-correlation functionals. The cluster was designed to describe accurately the first and second coordination spheres of the Cf(III) ions, and results in an accurate description of the Cf–O bonds. As indicated by the calculated charges, both Mulliken and natural bond orbitals (NBOs), provided in **Table D.1**, show the effective charge on the californium ions is far from the formal 3 at the DFT level. The Mulliken charges range from 1.5 to 1.85 e^-, and the NBO charges range from 1.70 to 1.85 e^-. Clearly, the charges are not 3 as expected for a fully ionic structure and do not strongly depend on whether a pure generalized gradient approximation or hybrid functional is used. Further analysis of the electron populations shows that much of the additional charge resides in the 6*d* orbitals with 0.7 e^-. There is about 0.3 e^- in the 7*p* and a 0.1 to 0.25 e^- additional population in the 5*f* orbitals.

Given the number of interacting oxygen (eight) in the first shell of the ligands, there is not much interaction for a given oxygen atom with the 5*f* orbitals, as shown in **Figure D.1**. The NBO population for 7*s* (0.08 e^-) is somewhat less than the Mulliken population on the 7*s*. As a check of the potential for issues with spin contamination with the $5f^9$ Cf(III) complex, we performed the same calculations with the high-spin $5f^7$ Cm(III), for which such an issue is not expected to be problematic. The results, as shown in the **Table D.2**, are essentially the same between californium and curium, which confirms that the observed donation of the borate to the Cf(III) was not an artifact. We also checked to see if the removal of protons to create a more negative ligand about the californium (and curium) changed the effective orbital interactions at

the actinide, and they did not. Overall, the predicted charges show that there is a substantial charge donation from the borate oxygen ligands to the californium, with about half of this extra charge into the 6*d*.

The topological analysis of the electron localization function (ELF) shows electron-donation from the eight coordinated O atoms to the californium.[154,162] About one to four bonding electrons can be found between the californium atom and each of the coordinated O atoms, **Table D.3**, consistent with the charge results. As several molecular orbitals can contribute to the same covalent basin, the analogy between the ELF approach and the notion of bonding in terms of molecular orbitals is not direct.

To further investigate the electronic structure of californium, the crystal-field splitting of the ground free-ion term (^{6}H) was predicted with complete active-space self-consistent field (CASSCF) calculations, which included either all high-spin $5f^9$ states (21 sextets) or states belonging to the ^{6}H of the free-ion (11 states). The lowest 11 states are not degenerate, as expected from symmetry arguments (the cluster belongs to the C_2 symmetry point group). The total splitting of this term (between the lowest and the highest root) is about 230 meV (1,850 cm^{-1}). We conclude that an unusually significant crystal-field splitting is present in this system. Thus, the crystal-field can also participate in the broadening observed in absorption and emission spectra, and the reduction in the magnetic moment. Owing to the high computational cost, the CASSCF calculations do not include basis functions to describe the critical 6*d* and 7*p* levels, so these CASSCF calculations cannot be used to examine the overall donation to Cf(III) levels. However, the CASSCF calculations do show that at least 0.16 e^- is transferred to the 5*f* orbitals from the ligands, consistent with the larger basis-set DFT results.

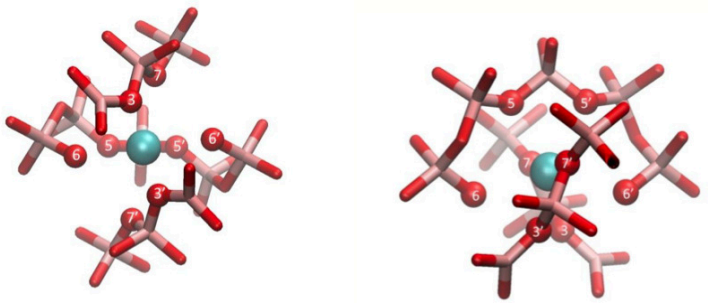

Figure D.1 Representation of the optimized cluster model and atom labeling scheme. Left: front view perpendicular to the C_2 axis. Right: top view parallel to the C_2 axis. Cf: pink, O: red, B: light cream, H atoms have been omitted for clarity. Ball and sick represent the central Cf and its first coordination sphere, capped sticks second and third sphere.

Table D.1. Molecular charges for the Cf atom obtained at various levels of theory

Method	f_{occ}	Mulliken Cf	NBO Cf	Mulliken Spin Cf
PBE	f_9	1.55/1.67[a]		4.9
PBE0	f_9	1.69/1.85[a]		4.98
B3LYP	f_9	1.51[b]	1.85	4.91
PW91	f_9	1.70[b]	1.7	4.8

[a] Unrestricted/spin restricted open-shell calculations.
[b] Unrestricted open-shell calculations.

Table D.2. Comparison of Cf and Cm model clusters with different charges.

Molecule	Functional	f_{occ}	Spin pop	NBO charge	Mulliken charge	Pop 7*s*	Pop 5*f*	Pop 6*d*	Pop 7*p*
$^6CfB_{11}O_{34}H_{32}$	B3LYP	f_9	4.91	1.85	1.51	0.08	9.11	0.65	0.29
	PW91	f_9	4.8	1.7	1.27	0.08	9.24	0.67	0.29
$^8CmB_{11}O_{34}H_{32}$	B3LYP	f_7	7.02	1.82	1.43	0.08	7.07	0.7	0.29
	PW91	f_7	7.06	1.72	1.17	0.08	7.09	0.76	0.3
$^6CfB_{11}O_{34}H_{30}^{-2}$	B3LYP	f_9	4.91	1.81	1.46	0.09	9.1	0.65	0.32
	PW91	f_9	4.8	1.65	1.2	0.09	9.24	0.67	0.32
$^8CmB_{11}O_{34}H_{30}^{-2}$	B3LYP	f_7	7.02	1.79	1.38	0.09	7.06	0.7	0.32
	PW91	f_7	7.07	1.68	1.12	0.08	7.08	0.76	0.33
$^6CfB_{11}O_{34}H_{26}^{-6}$	B3LYP	f_9	4.9	1.92	1.48	0.07	9.12	0.6	0.26
	PW91	f_9	4.76	1.74	1.22	0.07	9.28	0.61	0.27
$^8CmB_{11}O_{34}H_{26}^{-6}$	B3LYP	f_7	7.04	1.89	1.41	0.07	7.04	0.68	0.26
	PW91	f_7	7.09	1.78	1.15	0.07	7.06	0.74	0.28

Table D.3 Number of electrons involved in covalent V(Cf,O) ELF basins. The V(Cf,O) basins for which the maximum value of ELF was lower than 0.7 have been discarded from this analysis.

Atom	O_3	$O_{3'}$	O_5	$O_{5'}$	O_6	$O_{6'}$	O_7	$O_{7'}$
UPBE	3.12	3.08	3.32	3.43	4.08	4.05	1.47	1.58
UPBE0	1.66	1.62	4.4	4.08	1.74	1.76	1.82	1.82

APPENDIX E

COPYRIGHT PERMISSION LETTERS

Home | Create Account | Help

ACS Publications
Most Trusted. Most Cited. Most Read.

Title: Further Evidence for the Stabilization of U(V) within a Tetraoxo Core

Author: Jared T. Stritzinger, Evgeny V. Alekseev, Matthew J. Polinski, et al

Publication: Inorganic Chemistry

Publisher: American Chemical Society

Date: May 1, 2014

LOGIN

If you're a copyright.com user, you can login to RightsLink using your copyright.com credentials. Already **a RightsLink user** or want to learn more?

PERMISSION/LICENSE IS GRANTED FOR YOUR ORDER AT NO CHARGE

This type of permission/license, instead of the standard Terms & Conditions, is sent to you because no fee is being charged for your order. Please note the following:

- Permission is granted for your request in both print and electronic formats, and translations.
- If figures and/or tables were requested, they may be adapted or used in part.
- Please print this page for your records and send a copy of it to your publisher/graduate school.
- Appropriate credit for the requested material should be given as follows: "Reprinted (adapted) with permission from (COMPLETE REFERENCE CITATION). Copyright (YEAR) American Chemical Society." Insert appropriate information in place of the capitalized words.
- One-time permission is granted only for the use specified in your request. No additional uses are granted (such as derivative works or other editions). For any other uses, please submit a new request.

JOHN WILEY AND SONS LICENSE
TERMS AND CONDITIONS

Mar 16, 2015

This Agreement between Jared T Stritzinger ("You") and John Wiley and Sons ("John Wiley and Sons") consists of your license details and the terms and conditions provided by John Wiley and Sons and Copyright Clearance Center.

License Number	3590941134727
License date	Mar 16, 2015
Licensed Content Publisher	John Wiley and Sons
Licensed Content Publication	Chemistry - A European Journal
Licensed Content Title	Chirality and Polarity in the f-Block Borates M4[B16O26(OH)4(H2O)3Cl4] (M=Sm, Eu, Gd, Pu, Am, Cm, and Cf)
Licensed Content Author	Matthew J. Polinski,Kristen A. Pace,Jared. T. Stritzinger,Jian Lin,Justin N. Cross,Samantha K. Cary,Shelley M. Van Cleve,Evgeny V. Alekseev,Thomas E. Albrecht-Schmitt
Licensed Content Date	Jul 7, 2014
Pages	5
Type of use	Dissertation/Thesis
Requestor type	Author of this Wiley article
Format	Print and electronic
Portion	Full article
Will you be translating?	No
Title of your thesis / dissertation	A SYNTHETIC EXPLORATION OF ACTINDE BORATES AND PLUBITES
Expected completion date	May 2015
Expected size (number of pages)	150

REFERENCES

(1) Ewing, R. C. *Elements* **2006**, *2* (6), 331–334.

(2) Frazier, T. A. Blue Ribbon Commission on America's Nuclear Future Draft Report to the Secretary of Energy, 2011.

(3) Hudson, M. J.; Harwood, L. M.; Laventine, D. M.; Lewis, F. W. *Inorg. Chem.* **2013**, *52* (7), 3414–3428.

(4) Rechard, R. P.; Cotton, T. A.; Voegele, M. D. *Reliab. Eng. Syst. Saf.* **2014**, *122*, 7–31.

(5) Compliance Recertification Application for the Waste Isolation Pilot Plant Appendix SOTERM, 2009.

(6) Snider, A. C. Verification of the Definition of Generic Weep Brine and the Development of a Recipe for this Brine, 2003.

(7) Gorden, A. E. V.; DeVore, M. A.; Maynard, B. A. *Inorg. Chem.* **2013**, *52* (7), 3445–3458.

(8) Behrle, A. C.; Barnes, C. L.; Kaltsoyannis, N.; Walensky, J. R. *Inorg. Chem.* **2013**, *52* (18), 10623–10631.

(9) Birkett, J. E.; Carrott, M. J.; Fox, O. D.; Jones, C. J.; Maher, C. J.; Roube, C. V.; Taylor, R. J.; Woodhead, D. A. *Chim. Int. J. Chem.* **2005**, *59* (12), 898–904.

(10) Shannon, R. D. *Acta Crystallogr. Sect. A* **1976**, *32* (5), 751–767.

(11) Shannon, R. D.; Prewitt, C. T. *Acta Crystallogr. B* **1969**, *25* (5), 925–946.

(12) Girnt, D.; Roesky, P. W.; Geist, A.; Ruff, C. M.; Panak, P. J.; Denecke, M. A. *Inorg. Chem.* **2010**, *49* (20), 9627–9635.

(13) De Sahb, C.; Watson, L. A.; Nadas, J.; Hay, B. P. *Inorg. Chem.* **2013**, *52* (18), 10632–10642.

(14) Morss, L. R.; Edelstein, N. M.; Fuger, J.; Katz, J. J. *The Chemistry of the Actinide and Transactinide Elements*, 3rd ed.; Springer Science & Business Media, 2007.

(15) Kaltsoyannis, N.; Scott, P. *The f Elements*, 1 edition.; Oxford University Press: Oxford ; New York, 1999.

(16) Cotton, S. In *Lanthanide and Actinide Chemistry*; John Wiley & Sons, Ltd, 2006; pp 1–7.

(17) MacDonald, M. R.; Bates, J. E.; Ziller, J. W.; Furche, F.; Evans, W. J. *J. Am. Chem. Soc.* **2013**, *135* (26), 9857–9868.

(18) Cotton, S. In *Lanthanide and Actinide Chemistry*; John Wiley & Sons, Ltd, 2006; pp 145–153.

(19) Clark, D. L. *Los Alamos Sci.* **2000**, *26*, 364–381.

(20) Neidig, M. L.; Clark, D. L.; Martin, R. L. *Coord. Chem. Rev.* **2013**, *257* (2), 394–406.

(21) Denning, R. G. *J. Phys. Chem. A* **2007**, *111* (20), 4125–4143.

(22) Tatsumi, K.; Hoffmann, R. *Inorg. Chem.* **1980**, *19* (9), 2656–2658.

(23) Denning, R. G. In *Complexes, Clusters and Crystal Chemistry*; Structure and Bonding; Springer Berlin Heidelberg, 1992; pp 215–276.

(24) Wen, X.-D.; Martin, R. L.; Henderson, T. M.; Scuseria, G. E. *Chem. Rev.* **2013**, *113* (2), 1063–1096.

(25) Jensen, M. P.; Bond, A. H. *J. Am. Chem. Soc.* **2002**, *124* (33), 9870–9877.

(26) Prodan, I. D.; Scuseria, G. E.; Martin, R. L. *Phys. Rev. B* **2007**, *76* (3), 033101.

(27) Mehdoui, T.; Berthet, J.-C.; Thu□ry, P.; Ephritikhine, M. *Dalton Trans.* **2004**, No. 4, 579.

(28) Mazzanti, M.; Wietzke, R.; Pécaut, J.; Latour, J.-M.; Maldivi, P.; Remy, M. *Inorg. Chem.* **2002**, *41* (9), 2389–2399.

(29) Gaunt, A. J.; Scott, B. L.; Neu, M. P. *Angew. Chem.* **2006**, *118* (10), 1668–1671.

(30) Apostolidis, C.; Schimmelpfennig, B.; Magnani, N.; Lindqvist-Reis, P.; Walter, O.; Sykora, R.; Morgenstern, A.; Colineau, E.; Caciuffo, R.; Klenze, R.; Haire, R. G.; Rebizant, J.; Bruchertseifer, F.; Fanghänel, T. *Angew. Chem.* **2010**, *122* (36), 6487–6491.

(31) Kirker, I.; Kaltsoyannis, N. *Dalton Trans* **2011**, *40* (1), 124–131.

(32) Pappalardo, R.; Carnall, W.; Fields, P. *J. Chem. Phys.* **1969**, *51* (2), 842–843.

(33) Baumgärtner, F.; Fischer, E. O.; Kanellakopulos, B.; Laubereau, P. *Angew. Chem.* **1966**, *78* (1), 112–113.

(34) Laubereau, P. G.; Burns, J. H. *Inorg. Chem.* **1970**, *9* (5), 1091–1095.

(35) Bursten, B. E.; Strittmatter, R. J. *Angew. Chem. Int. Ed. Engl.* **1991**, *30* (9), 1069–1085.

(36) Bursten, B. E.; Rhodes, L. F.; Strittmatter, R. J. *J. Am. Chem. Soc.* **1989**, *111* (8), 2756–2758.

(37) Bursten, B. E.; Rhodes, L. F.; Strittmatter, R. J. *J. Am. Chem. Soc.* **1989**, *111* (8), 2758–2766.

(38) Choppin, G. R. *J. Alloys Compd.* **2002**, *344* (1–2), 55–59.

(39) Banik, N. L.; Schimmelpfennig, B.; Marquardt, C. M.; Brendebach, B.; Geist, A.; Denecke, M. A. *Dalton Trans.* **2010**, *39* (21), 5117.

(40) Miguirditchian, M.; Guillaneux, D.; Guillaumont, D.; Moisy, P.; Madic, C.; Jensen, M. P.; Nash, K. L. *Inorg. Chem.* **2005**, *44* (5), 1404–1412.

(41) Polinski, M. J.; Iii, E. B. G.; Maurice, R.; Planas, N.; Stritzinger, J. T.; Parker, T. G.; Cross, J. N.; Green, T. D.; Alekseev, E. V.; Cleve, S. M. V.; Depmeier, W.; Gagliardi, L.; Shatruk, M.; Knappenberger, K. L.; Liu, G.; Skanthakumar, S.; Soderholm, L.; Dixon, D. A.; Albrecht-Schmitt, T. E. *Nat. Chem.* **2014**, *6* (5), 387–392.

(42) Polinski, M. J.; Grant, D. J.; Wang, S.; Alekseev, E. V.; Cross, J. N.; Villa, E. M.; Depmeier, W.; Gagliardi, L.; Albrecht-Schmitt, T. E. *J. Am. Chem. Soc.* **2012**, *134* (25), 10682–10692.

(43) Polinski, M. J.; Wang, S.; Alekseev, E. V.; Depmeier, W.; Albrecht-Schmitt, T. E. *Angew. Chem. Int. Ed.* **2011**, *50* (38), 8891–8894.

(44) Polinski, M. J.; Wang, S.; Alekseev, E. V.; Depmeier, W.; Liu, G.; Haire, R. G.; Albrecht-Schmitt, T. E. *Angew. Chem. Int. Ed.* **2012**, *51* (8), 1869–1872.

(45) Polinski, M. J.; Wang, S.; Cross, J. N.; Alekseev, E. V.; Depmeier, W.; Albrecht-Schmitt, T. E. *Inorg. Chem.* **2012**, *51* (14), 7859–7866.

(46) Zou, G.; Huang, L.; Ye, N.; Lin, C.; Cheng, W.; Huang, H. *J. Am. Chem. Soc.* **2013**, *135* (49), 18560–18566.

(47) Becker, P. *Adv. Mater.* **1998**, *10* (13), 979–992.

(48) Goodey, J.; Broussard, J.; Halasyamani, P. S. *Chem. Mater.* **2002**, *14* (7), 3174–3180.

(49) Bergman, J. G.; Crane, G. R. *J. Solid State Chem.* **1975**, *12* (3–4), 172–175.

(50) Cross, J. N.; Villa, E. M.; Wang, S.; Diwu, J.; Polinski, M. J.; Albrecht-Schmitt, T. E. *Inorg. Chem.* **2012**, *51* (15), 8419–8424.

(51) Cross, J. N.; Cary, S. K.; Stritzinger, J. T.; Polinski, M. J.; Albrecht Schmitt, T. E. *Inorg. Chem.* **2014**, *53* (6), 3148–3152.

(52) Cross, J. N.; Duncan, P. M.; Villa, E. M.; Polinski, M. J.; Babo, J.-M.; Alekseev, E. V.; Booth, C. H.; Albrecht-Schmitt, T. E. *J. Am. Chem. Soc.* **2013**, *135* (7), 2769–2775.

(53) Cross, J. N. Tuning Actinide Complexes Through Structure and Oxidation State http://etd.nd.edu/ETD-db/theses/available/etd-06232014-160131/ (accessed Mar 18, 2015).

(54) Lo, B. W. N. *J. Phys. Chem. Solids* **1973**, *34* (3), 513–520.

(55) Leonyuk, N. I. *J. Cryst. Growth* **1997**, *174* (1–4), 301–307.

(56) *CRC Handbook of Chemistry and Physics*, 95th ed.; Haynes, W. M., Ed.; CRC Press: Boca Raton, Florida, 2015.

(57) Williams, I. D.; Wu, M.; Sung, H. H.-Y.; Zhang, X. X.; Yu, J. *Chem. Commun.* **1998**, No. 22, 2463–2464.

(58) Ju, J.; Lin, J.; Li, G.; Yang, T.; Li, H.; Liao, F.; Loong, C.-K.; You, L. *Angew. Chem. Int. Ed.* **2003**, *42* (45), 5607–5610.

(59) Ju, J.; Yang, T.; Li, G.; Liao, F.; Wang, Y.; You, L.; Lin, J. *Chem. – Eur. J.* **2004**, *10* (16), 3901–3906.

(60) Yang, T.; Ju, J.; Li, G.; Liao, F.; Zou, X.; Deng, F.; Chen, L.; Wang, Y.; Lin, J. *Inorg. Chem.* **2007**, *46* (12), 4772–4774.

(61) Yang, W.; Li, J.; Pan, Q.; Jin, Z.; Yu, J.; Xu, R. *Chem. Mater.* **2008**, *20* (15), 4900–4905.

(62) Yang, M.; Yu, J.; Di, J.; Li, J.; Chen, P.; Fang, Q.; Chen, Y.; Xu, R. *Inorg. Chem.* **2006**, *45* (9), 3588–3593.

(63) Yang, T.; Sun, J.; Li, G.; Wang, Y.; Christensen, J.; He, Z.; Christensen, K. E.; Zou, X.; Liao, F.; Lin, J. *Inorg. Chem.* **2009**, *48* (23), 11209–11214.

(64) Ju, J.; Sasaki, J.; Yang, T.; Kasamatsu, S.; Negishi, E.; Li, G.; Lin, J.; Nojiri, H.; Rachi, T.; Tanigaki, K.; Toyota, N. *Dalton Trans.* **2006**, No. 13, 1597.

(65) Yang, T.; Li, G.; You, L.; Ju, J.; Liao, F.; Lin, J. *Chem. Commun.* **2005**, No. 33, 4225.

(66) Lu, P.; Wang, Y.; Lin, J.; You, L. *Chem. Commun.* **2001**, No. 13, 1178–1179.

(67) Li, L.; Lu, P.; Wang, Y.; Jin, X.; Li, G.; Wang, Y.; You, L.; Lin, J. *Chem. Mater.* **2002**, *14* (12), 4963–4968.

(68) Li, L.; Jin, X.; Li, G.; Wang, Y.; Liao, F.; Yao, G.; Lin, J. *Chem. Mater.* **2003**, *15* (11), 2253–2260.

(69) Wang, S.; Alekseev, E. V.; Stritzinger, J. T.; Depmeier, W.; Albrecht-Schmitt, T. E. *Inorg. Chem.* **2010**, *49* (6), 2948–2953.

(70) Wang, S.; Villa, E. M.; Diwu, J.; Alekseev, E. V.; Depmeier, W.; Albrecht-Schmitt, T. E. *Inorg. Chem.* **2011**, *50* (6), 2527–2533.

(71) Wang, S.; Alekseev, E. V.; Miller, H. M.; Depmeier, W.; Albrecht-Schmitt, T. E. *Inorg. Chem.* **2010**, *49* (21), 9755–9757.

(72) Wang, S.; Alekseev, E. V.; Diwu, J.; Casey, W. H.; Phillips, B. L.; Depmeier, W.; Albrecht-Schmitt, T. E. *Angew. Chem.* **2010**, *122* (6), 1075–1078.

(73) Wang, S.; Alekseev, E. V.; Ling, J.; Skanthakumar, S.; Soderholm, L.; Depmeier, W.; Albrecht-Schmitt, T. E. *Angew. Chem. Int. Ed.* **2010**, *49* (7), 1263–1266.

(74) Rabenau, A. *Angew. Chem. Int. Ed. Engl.* **1985**, *24* (12), 1026–1040.

(75) Feng, S.; Xu, R. *Acc. Chem. Res.* **2001**, *34* (3), 239–247.

(76) Kolis, J. W.; Korzenski, M. B. In *Chemical Synthesis Using Supercritical Fluids*; Jessop, P. G., Leitner, W., Eds.; Wiley-VCH Verlag GmbH, 1999; pp 213–242.

(77) Bünzli, J.-C. G.; Piguet, C. *Chem. Soc. Rev.* **2005**, *34* (12), 1048–1077.

(78) Shang, M.; Geng, D.; Kang, X.; Yang, D.; Zhang, Y.; Lin, J. *Inorg. Chem.* **2012**, *51* (20), 11106–11116.

(79) Cotton, F. A.; Wilkinson, G.; Murillo, C. A.; Bochmann, M. *Advanced Inorganic Chemistry*, 6 edition.; Wiley-Interscience: New York, 1999.

(80) Ilton, E. S.; Haiduc, A.; Cahill, C. L.; Felmy, A. R. *Inorg. Chem.* **2005**, *44* (9), 2986–2988.

(81) Chen, C.-S.; Lee, S.-F.; Lii, K.-H. *J. Am. Chem. Soc.* **2005**, *127* (35), 12208–12209.

(82) Belai, N.; Frisch, M.; Ilton, E. S.; Ravel, B.; Cahill, C. L. *Inorg. Chem.* **2008**, *47* (21), 10135–10140.

(83) Lee, C.-S.; Lin, C.-H.; Wang, S.-L.; Lii, K.-H. *Angew. Chem. Int. Ed.* **2010**, *49* (25), 4254–4256.

(84) Burns, P. C. *Can. Mineral.* **2005**, *43* (6), 1839–1894.

(85) Burns, P. C.; Ewing, R. C.; Hawthorne, F. C. *Can. Mineral.* **1997**, *35*, 1551–1570.

(86) Wang, S.; Alekseev, E. V.; Depmeier, W.; Albrecht-Schmitt, T. E. *Chem. Commun.* **2011**, *47* (39), 10874.

(87) Wang, S.; Alekseev, E. V.; Ling, J.; Skanthakumar, S.; Soderholm, L.; Depmeier, W.; Albrecht-Schmitt, T. E. *Angew. Chem. Int. Ed.* **2010**, *49* (7), 1263–1266.

(88) Franck, E. U. *Fluid Phase Equilibria* **1983**, *10* (2–3), 211–222.

(89) Lobachev, A. *Hydrothermal synthesis of crystals*; Consultants Bureau, 1971.

(90) Rabenau, A. *J. of Materials Ed* **1988**, *10*, 543–591.

(91) Wu, S.; Wang, S.; Polinski, M.; Beermann, O.; Kegler, P.; Malcherek, T.; Holzheid, A.; Depmeier, W.; Bosbach, D.; Albrecht-Schmitt, T. E.; Alekseev, E. V. *Inorg. Chem.* **2013**, *52* (9), 5110–5118.

(92) Lin, C.-H.; Lii, K.-H. *Angew. Chem.* **2008**, *120* (45), 8839–8841.

(93) Lee, C.-S.; Wang, S.-L.; Lii, K.-H. *J. Am. Chem. Soc.* **2009**, *131* (42), 15116–15117.

(94) Chen, C.-L.; Nguyen, Q. B.; Chen, C.-S.; Lii, K.-H. *Inorg. Chem.* **2012**, *51* (14), 7463–7465.

(95) Gasperin, M. *Acta Crystallogr. C* **1989**, *45* (7), 981–983.

(96) Hinteregger, E.; Hofer, T. S.; Heymann, G.; Perfler, L.; Kraus, F.; Huppertz, H. *Chem. - Eur. J.* **2013**, *19* (47), 15985–15992.

(97) Carnall, W. T.; Liu, G. K.; Williams, C. W.; Reid, M. F. *J. Chem. Phys.* **1991**, *95* (10), 7194–7203.

(98) Leung, A. F.; Poon, Y.-M. *Can. J. Phys.* **1977**, *55* (10), 937–942.

(99) De Wet, J. F.; du Preez, J. G. H. *J. Chem. Soc. Dalton Trans.* **1978**, No. 6, 592.

(100) Arney, D. S. J.; Burns, C. J. *J. Am. Chem. Soc.* **1995**, *117* (37), 9448–9460.

(101) Fortier, S.; Kaltsoyannis, N.; Wu, G.; Hayton, T. W. *J. Am. Chem. Soc.* **2011**, *133* (36), 14224–14227.

(102) Williams, C. W.; Blaudeau, J.-P.; Sullivan, J. C.; Antonio, M. R.; Bursten, B.; Soderholm, L. *J. Am. Chem. Soc.* **2001**, *123* (18), 4346–4347.

(103) Fieser, M. E.; MacDonald, M. R.; Krull, B. T.; Bates, J. E.; Ziller, J. W.; Furche, F.; Evans, W. J. *J. Am. Chem. Soc.* **2015**, *137* (1), 369–382.

(104) Siidra, O. I.; Krivovichev, S. V.; Armbruster, T.; Depmeier, W. *Inorg. Chem.* **2007**, *46* (5), 1523–1525.

(105) Wang, G.; Luo, M.; Lin, C.; Ye, N.; Zhou, Y.; Cheng, W. *Inorg. Chem.* **2014**, *53* (23), 12584–12589.

(106) Binnemans, K.; Görller-Walrand, C. *Chem. Phys. Lett.* **1995**, *235* (3–4), 163–174.

(107) Tanner, P. A. *Chem. Soc. Rev.* **2013**, *42* (12), 5090–5101.

(108) Knope, K. E.; Vasiliu, M.; Dixon, D. A.; Soderholm, L. *Inorg. Chem.* **2012**, *51* (7), 4239–4249.

(109) Knope, K. E.; Wilson, R. E.; Vasiliu, M.; Dixon, D. A.; Soderholm, L. *Inorg. Chem.* **2011**, *50* (19), 9696–9704.

(110) Hu, Y.-J.; Knope, K. E.; Skanthakumar, S.; Soderholm, L. *Eur. J. Inorg. Chem.* **2013**, *2013* (24), 4159–4163.

(111) Sykora, R. E.; Assefa, Z.; Haire, R. G.; Albrecht-Schmitt, T. E. *Inorg. Chem.* **2006**, *45* (2), 475–477.

(112) Burns, J. H.; Peterson, J. R.; Baybarz, R. D. *J. Inorg. Nucl. Chem.* **1973**, *35* (4), 1171–1177.

(113) Galbis, E.; Hernández-Cobos, J.; den Auwer, C.; Le Naour, C.; Guillaumont, D.; Simoni, E.; Pappalardo, R. R.; Sánchez Marcos, E. *Angew. Chem.* **2010**, *122* (22), 3899–3903.

(114) Lindqvist-Reis, P.; Apostolidis, C.; Rebizant, J.; Morgenstern, A.; Klenze, R.; Walter, O.; Fanghänel, T.; Haire, R. G. *Angew. Chem.* **2007**, *119* (6), 937–940.

(115) Skanthakumar, S.; Antonio, M. R.; Wilson, R. E.; Soderholm, L. *Inorg. Chem.* **2007**, *46* (9), 3485–3491.

(116) Ruiz-Martínez, A.; Casanova, D.; Alvarez, S. *Chem. – Eur. J.* **2008**, *14* (4), 1291–1303.

(117) Ruiz-Martínez, A.; Alvarez, S. *Chem. – Eur. J.* **2009**, *15* (30), 7470–7480.

(118) Castro-Rodriguez, I.; Olsen, K.; Gantzel, P.; Meyer, K. *J. Am. Chem. Soc.* **2003**, *125* (15), 4565–4571.

(119) Skanthakumar, S.; Soderholm, L.; Movshovich, R. *J. Alloys Compd.* **2000**, *303–304*, 298–302.

(120) Staub, U.; Soderholm, L.; Wasserman, S. R.; Conner, A. G. O.; Kramer, M. J.; Patterson, B. D.; Shi, M.; Knapp, M. *Phys. Rev. B* **2000**, *61* (2), 1548–1554.

(121) Fields, P.; Wybourne, B.; Carnall, W. *The electronic energy levels of the heavy actinides Bk+ 3 (5f8), Cf+ 3 (5f9), Es+ 3 (5f10), and Fm+ 3 (5f11)*; Argonne National Laboratory, 1964; Vol. 6911.

(122) Campos, A. F.; Meijerink, A.; Donegá, C. de M.; Malta, O. L. *J. Phys. Chem. Solids* **2000**, *61* (9), 1489–1498.

(123) Legendziewicz, J. *J. Alloys Compd.* **2000**, *300–301*, 71–87.

(124) Roos, B. O.; Malmqvist, P.-Å.; Gagliardi, L. *J. Am. Chem. Soc.* **2006**, *128* (51), 17000–17006.

(125) Kovács, A.; Pogány, P.; Konings, R. J. M. *Inorg. Chem.* **2012**, *51* (8), 4841–4849.

(126) Kovács, A.; Konings, R. J. M.; Varga, Z.; Szieberth, D. *J. Phys. Chem. A* **2013**, *117* (44), 11357–11363.

(127) Burns, J. H.; Peterson, J. R. *Acta Crystallogr. B* **1970**, *26* (11), 1885–1887.

(128) Carnall, W. T. *J. Chem. Phys.* **1992**, *96* (12), 8713–8726.

(129) Milman, V.; Winkler, B.; Pickard, C. J. *J. Nucl. Mater.* **2003**, *322* (2–3), 165–179.

(130) Peterson, J. R.; Burns, J. H. *J. Inorg. Nucl. Chem.* **1973**, *35* (5), 1525–1530.

(131) Runde, W.; Bean, A. C.; Brodnax, L. F.; Scott, B. L. *Inorg. Chem.* **2006**, *45* (6), 2479–2482.

(132) Sykora, R. E.; Assefa, Z.; Haire, R. G.; Albrecht-Schmitt, T. E. *J. Solid State Chem.* **2004**, *177* (12), 4413–4419.

(133) Polinski, M. J.; Villa, E. M.; Albrecht-Schmitt, T. E. *Coord. Chem. Rev.* **2014**, *266–267*, 16–27.

(134) Matonic, J. H.; Scott, B. L.; Neu, M. P. *Inorg. Chem.* **2001**, *40* (12), 2638–2639.

(135) Polinski, M. J.; Wang, S.; Alekseev, E. V.; Cross, J. N.; Depmeier, W.; Albrecht-Schmitt, T. E. *Inorg. Chem.* **2012**, *51* (21), 11541–11548.

(136) Polinski, M. J.; Alekseev, E. V.; Darling, V. R.; Cross, J. N.; Depmeier, W.; Albrecht-Schmitt, T. E. *Inorg. Chem.* **2013**, *52* (4), 1965–1975.

(137) Polinski, M. J.; Cross, J. N.; Villa, E. M.; Lin, J.; Alekseev, E. V.; Depmeier, W.; Albrecht-Schmitt, T. E. *Inorg. Chem.* **2013**, *52* (14), 8099–8105.

(138) Carnall, W. T.; Rajnak, K. *J. Chem. Phys.* **1975**, *63* (8), 3510–3514.

(139) Sluis, K. L. V.; Nugent, L. J. *J. Opt. Soc. Am.* **1974**, *64* (5), 687–695.

(140) Conway, J. G.; Fried, S.; Latimer, R. M.; McLaughlin, R.; Gutmacher, R. G.; Carnall, W. T.; Fields, P. *J. Inorg. Nucl. Chem.* **1966**, *28* (12), 3064–3066.

(141) Conway, J. G.; Gruber, J. B.; Hulet, E. K.; Morrow, R. J.; Gutmacher, R. G. *J. Chem. Phys.* **1962**, *36* (1), 189–190.

(142) Kim, J. I.; Klenze, R.; Wimmer, H. **1991**.

(143) Law, G.-L.; Andolina, C. M.; Xu, J.; Luu, V.; Rutkowski, P. X.; Muller, G.; Shuh, D. K.; Gibson, J. K.; Raymond, K. N. *J. Am. Chem. Soc.* **2012**, *134* (37), 15545–15549.

(144) Ramya, A. R.; Sharma, D.; Natarajan, S.; Reddy, M. L. P. *Inorg. Chem.* **2012**, *51* (16), 8818–8826.

(145) Carnall, W. T.; Fields, P. R.; Rajnak, K. *J. Chem. Phys.* **1968**, *49* (10), 4424–4442.

(146) Yuasa, J.; Mukai, R.; Hasegawa, Y.; Kawai, T. *Chem. Commun.* **2014**, *50* (59), 7937–7940.

(147) Crosswhite, H. M.; Crosswhite, H.; Carnall, W. T.; Paszek, A. P. *J. Chem. Phys.* **1980**, *72* (9), 5103–5117.

(148) Carnall, W. T.; Fields, P. R.; Rajnak, K. *J. Chem. Phys.* **1968**, *49* (10), 4443–4446.

(149) Carnall, W. T.; Fields, P. R.; Rajnak, K. *J. Chem. Phys.* **1968**, *49* (10), 4450–4455.

(150) Carnall, W. T.; Fields, P. R.; Wybourne, B. G. *J. Chem. Phys.* **1965**, *42* (11), 3797–3806.

(151) Carnall, W. T.; Fields, P. R.; Rajnak, K. *J. Chem. Phys.* **1968**, *49* (10), 4412–4423.

(152) Yatsimirskii, K. B.; Davidenko, N. K. *Coord. Chem. Rev.* **1979**, *27* (3), 223–273.

(153) Peijzel, P. S.; Meijerink, A.; Wegh, R. T.; Reid, M. F.; Burdick, G. W. *J. Solid State Chem.* **2005**, *178* (2), 448–453.

(154) Kohout, M.; Savin, A. *Int. J. Quantum Chem.* **1996**, *60* (4), 875–882.

(155) Becke, A. D.; Edgecombe, K. E. *J. Chem. Phys.* **1990**, *92* (9), 5397–5403.

(156) Schäfer, A.; Huber, C.; Ahlrichs, R. *J. Chem. Phys.* **1994**, *100* (8), 5829–5835.

(157) Cao, X.; Dolg, M. *J. Mol. Struct. THEOCHEM* **2004**, *673* (1–3), 203–209.

(158) Perdew, J. P.; Burke, K.; Ernzerhof, M. *Phys. Rev. Lett.* **1996**, *77* (18), 3865–3868.

(159) Cao, X.; Dolg, M.; Stoll, H. *J. Chem. Phys.* **2003**, *118* (2), 487–496.

(160) Reed, A. E.; Curtiss, L. A.; Weinhold, F. *Chem. Rev.* **1988**, *88* (6), 899–926.

(161) Silvi, B.; Savin, A. *Nature* **1994**, *371* (6499), 683–686.

(162) Roos, B. O.; Taylor, P. R.; Si�doteqgbahn, P. E. M. *Chem. Phys.* **1980**, *48* (2), 157–173.

(163) Aquilante, F.; De Vico, L.; Ferré, N.; Ghigo, G.; Malmqvist, P.-åke; Neogrády, P.; Pedersen, T. B.; Pitoňák, M.; Reiher, M.; Roos, B. O.; Serrano-Andrés, L.; Urban, M.; Veryazov, V.; Lindh, R. *J. Comput. Chem.* **2010**, *31* (1), 224–247.

(164) Tsuchiya, T.; Abe, M.; Nakajima, T.; Hirao, K. *J. Chem. Phys.* **2001**, *115* (10), 4463–4472.

(165) Douglas, M.; Kroll, N. M. *Ann. Phys.* **1974**, *82* (1), 89–155.

(166) Hess, B. A. *Phys. Rev. A* **1986**, *33* (6), 3742–3748.

(167) Perdew, J. P.; Ernzerhof, M.; Burke, K. *J. Chem. Phys.* **1996**, *105* (22), 9982–9985.

BIOGRAPHICAL SKETCH

Jared Tyler Stritzinger
Department of Chemistry and Biochemistry
95 Chieftain Way Florida State University
Tallahassee, FL 32306

Education

Florida State University, Department of Chemistry and Biochemistry, Tallahassee, FL
- Ph.D. in Inorganic Chemistry, May 2015 GPA 4.0/4.0

Clemson University, Department of Chemistry, Clemson, SC
- B.S. in Chemistry, *Magna Cum Laude*, May 2011 GPA 3.7/4.0

Research Experience

Graduate Student: Research Advisor: Thomas E. Albrecht-Schmitt

- Investigated solid-state chemistry of the lanthanides and actinides including transuranic elements Np - Cf to probe periodic trends.
- Designed and operated an experimental set-up for synthesis in supercritical water.
- Synthesized solid materials using hydrothermal/solvothermal techniques.
- Characterized materials using single crystal and powder X-ray diffraction, solid-state UV-Vis-NIR absorption and luminescence spectroscopy, and SEM-EDX

Skills and Techniques

- Experienced with techniques and procedures for handling highly radioactive materials and maintaining safe working environment.
- Synthetic experience in the hydrothermal, solvothermal, and supercritical water regimes.
- Command of positive- and negative-pressure gloveboxes
- Able to work glass and quartz tubes
- Basic TIG welding skills
- Adept at acquisition and structural solution for single crystal X-ray data; able to handle general structural problems such as twinning or disorder
- Acquisition and interpretation of UV-Vis-NIR absorbance and photoluminescence spectroscopy.
- Acquisition of SEM-EDS spectra on single crystals.
- Experience with powder X-ray diffraction.

Publications

1. Stritzinger, J. T.; Pace, K. P.; Barth, A. T.; Beatrice, M. T.; Silver, M. A.; Cary, S. K.; Eaton, T. M.; Albrecht-Schmitt, T. E., "Structural and Electronic Variations in *f* -Element Containing Lead Oxide Nano-Clusters," **In Preparation**
2. Cross, J.N.; Cary, S.K.; Marr, C.J.; Stritzinger, J.T.; Polinski, M.J.; Albrecht-Schmitt, T.E. "Massive Charge Transfer in Trivalent Plutonium and Cerium Tungstates and the Structural Deviation of Americium," **In Preparation**
3. Cary, S. K.; Vasiliu, M.; Baumbach, R. E.; Stritzinger, J. T.; Green, T. D.; Diefenbach, K.; Cross, J. N.; Knappenberger, K. L.; Liu, G.; Silver, M. A.; DePrince, A. E.; Cleve, S. M. V.; House, J. H.; Kikugawa, N.; Gallagher, A.; Arico, A. A.; Dixon, D. A.; Albrecht-Schmitt, T. E., "Emergence of Californium as the Second Transitional Element in the Actinide Series" *Nat Com*. **In Review**
4. Polinski, M. J.; Pace, K. A.; Stritzinger, J.T.; Lin, J.; Cross, J.N.; Cary, S. K.; Van Cleve, S.M.; Alekseev, E. V.; Albrecht-Schmitt, T. E., "Chirality and Polarity in the f-Block Borates $M_4[B_{16}O_{26}(OH)_4(H_2O)_3Cl_4]$ (M=Sm, Eu, Gd, Pu, Am, Cm, and Cf),"*Chem. Eur. J.*, **2014**, *20*, 9892–9896. Published: July 7, 2014
5. Stritzinger, J. T.; Alekseev, E. V.; Polinski, M. J.; Cross, J. N.; Eaton, T. M.; Albrecht-Schmitt, T. E. "Further Evidence for the Stabilization of U(V) within a Tetraoxo Core," *Inorg. Chem.* **2014**, *53*, 5294–5299. Published: May 1, 2014
6. Polinski, M. J.; Iii, E. B. G.; Maurice, R.; Planas, N.; Stritzinger, J. T.; Parker, T. G.; Cross, J. N.; Green, T. D.; Alekseev, E. V.; Cleve, S. M. V.; Depmeier, W.; Gagliardi, L.; Shatruk, M.; Knappenberger, K. L.; Liu, G.; Skanthakumar, S.; Soderholm, L.; Dixon, D. A.; Albrecht-Schmitt, T. E., "Unusual structure, bonding and properties in a californium borate," *Nat. Chem.* **2014**, *6*, 387–392. Published: March 23, 2014
7. Cross, J. N.; Cary, S. K.; Stritzinger, J. T.; Polinski, M. J.; Albrecht Schmitt, T. E. , "Synthesis and Spectroscopy of New Plutonium(III) and -(IV) Molybdates: Comparisons of Electronic Characteristics," *Inorg. Chem.* **2014**, *53*, 3148–3152. Published: March 6, 2014
8. Lin, J.; Eaton, T.; Cross, J.N.; Stritzinger, J. T.; Albrecht-Schmitt, T. E., "$Th(VO_3)_2(SeO_3)$ and $Ln(VO_3)_2(IO_3)$ (Ln = Ce, Pr, Nd, Sm, and Eu): unusual cases of aliovalent substitution," *Chem. Commun*., **2014**, *50*, 3668-3670. Published: February 17, 2014
9. McMillen, C. D.; Stritzinger, J.; Kolis, J. "Two Novel Acentric Borate Fluorides: $M_3B_6O_{11}F_2$ (M = Sr, Ba)," *Inorg. Chem.*, **2012**, *51* (7), 3953–3955. Published: March 12, 2012
10. McMillen, C. D.; Emirdag-Eanes, M.; Stritzinger, J.; Kolis, J., "Hydrothermal synthesis of new rare earth silicate fluorides: A novel class of polar materials," *J. Solid State Chem.* **2012,** *195*, 155-160. Published: March 3, 2012
11. Stritzinger, J.; McMillen, C. D.; Kolis, J. "Hydrothermal Synthesis and Single Crystal Structures of New Thorium Fluorides: $A_3Ba_2Th_3F_{19}$ (A = Na, K, Rb)," *J. Chem. Crystallographer*. **2012**, *42* (4), 366-371. Published: February 22, 2012
12. Wang, S.; Alekseev, E.; Stritzinger, J.; Liu, G; Depmeier, W.; Albrecht-Schmitt, T. "Structure-Property Relationships in Lithium, Silver, and Cesium Uranyl Borates," *Chem. Mater.* **2010**, *22*, 5983–5991. Published: October 13, 2010

13. Wang, S.; Alekseev, E.; Stritzinger, J.; Depmeier, W.; Albrecht-Schmitt, T. "Crystal Chemistry of the Potassium and Rubidium Uranyl Borate Families Derived from Boric Acid Fluxes," *Inorg. Chem.* **2010**, *49*, 6690–6696. Published: June 18, 2010
14. Wang, S.; Alekseev, E.; Stritzinger, J.; Depmeier, W.; Albrecht-Schmitt, T. "How are centrosymmetric and noncentrosymmetric structures achieved in uranyl borates?" *Inorg. Chem.* **2010**, *49*, 2948-2953. Published February 16, 2010

Conference Participation

- ACS Nation Meeting (249st Annual Spring Meeting) – Denver, CO March 2015
  - Oral presentation: Structural Variations in *f*-Element Plumbite Nanoclusters
- Plutonium Futures – Las Vegas, NV, September 2014
  - Poster presentation: Exploration of Uranyl Borate System in Supercritical Water.
- ACS Nation Meeting (241st Annual Spring Meeting) – New Orleans, LA, March 2013
  - Poster presentation: Exploration of Uranyl Borate System in Supercritical Water.
- Florida Solid State Conference (1st Annual Meeting) - Tallahassee, FL, September 2012
  - Poster presentation: Exploration of Uranyl Borate System in Supercritical Water.
- ACS Nation Meeting (241st Annual Spring Meeting) – Anaheim, CA, March 2011
  - Poster presentation: Hydrothermal synthesis and crystal chemistry of novel fluorides and fluoroborates.
- ACS Nation Meeting (239th Annual Spring Meeting) – San Francisco, CA, March 2010
  - Poster presentation: Synthesis and characterization of new uranyl borates.

Professional Organization

- American Chemical Society